2015

Los Alamos Space Weather Summer School
Research Reports

Misa M. Cowee *(Editor)*

2015

Los Alamos Space Weather Summer School
Research Reports

Misa M. Cowee *(Editor)*

2015

Los Alamos Space Weather Summer School
Research Reports

Preface

The fifth Los Alamos Space Weather Summer School was held June 1st – July 24th, 2015, at Los Alamos National Laboratory (LANL). With renewed support from the Institute of Geophysics, Planetary Physics, and Signatures (IGPPS) and additional support from the National Aeronautics and Space Administration (NASA) and the Department of Energy (DOE) Office of Science, we hosted a new class of five students from various U.S. and foreign research institutions. The summer school curriculum includes a series of structured lectures as well as mentored research and practicum opportunities. Lecture topics including general and specialized topics in the field of space weather were given by a number of researchers affiliated with LANL.

Students were given the opportunity to engage in research projects through a mentored practicum experience. Each student works with one or more LANL-affiliated mentors to execute a collaborative research project, typically linked with a larger on-going research effort at LANL and/or the student's PhD thesis research. This model provides a valuable learning experience for the student while developing the opportunity for future collaboration.

This report includes a summary of the research efforts fostered and facilitated by the Space Weather Summer School. These reports should be viewed as work-in-progress as the short session typically only offers sufficient time for preliminary results. At the close of the summer school session, students present a summary of their research efforts.

It has been a pleasure for me to be the director of the Los Alamos Space Weather Summer School this year. I am very proud of the work done by the students, mentors and lecturers—your dedicated effort and professionalism are key to a successful program. I am grateful for all the administrative and logistical help I have received in organizing the program.

Los Alamos, NM   Dr. Misa Cowee
November 2015   *Summer School Director*

2015

New students

Yuxi Chen	*University of Michigan*
Ravindra Desai	*University College London, UK*
Ehab Hassan	*University of Texas at Austin*
Nadine Kalmoni	*University College London, UK*
Dong Lin	*Virginia Polytechnic Institute and State University*

Returning students

Sebastian De Pascuale	*University of Iowa*
R. Scott Hughes	*University of Southern California*
Hong Zhao	*University of Colorado Boulder*

2015

**Los Alamos Space Weather Summer School
Research Reports**

Project Reports

New Students

Returning Students

2015

Los Alamos Space Weather Summer School
Research Reports

2015

Pictures

Class of 2015 Students and Mentors
(Students indicated in bold. Left to right, back row: John Steinberg, Reiner Friedel, Steve Morley, Mike Henderson, Xiangrong Fu; middle row: **Sebastian DePascaule, Ehab Hassan, Hong Zhao, Dong Lin, Yuxi Chen, R. Scott Hughes***; front row: Ravi Desai, Josefina Salazar, Misa Cowee,* **Nadine Kalmoni,** *Vania Jordanova. Not pictured: Gian Luca Delzanno, Yiqun Yu, and Peter Gary.*

2015

**Los Alamos Space Weather Summer School
Research Reports**

Lectures

2015

**Los Alamos Space Weather Summer School
Research Reports**

Sponsors

- Institute of Geophysics, Planetary Physics, and Signatures (IGPPS)
- National Aeronautics and Space Administration (NASA)
- Department of Energy - Office of Science (DOE-OSC)

Contact Information

Publication Release

Full Particle-in-Cell(PIC) Simulation of Whistler Wave Generation

Yuxi Chen

Center for Space Environment Modeling, University of Michigan, Ann Arbor, Michigan, USA

Yiqun Yu

Beihang University, Beijing, China

Gian Luca Delzanno

Los Alamos National Laboratory, New Mexico, USA

Abstract

Whistler waves are considered as an important mechanism for both electrons acceleration and precipitation in the radiation belts. The generation and propagation of whistler waves have drawn great attention in the space physics field. As a preliminary study to understand the development of electron temperature anisotropy, the generation and propagation of whistler waves, and the influence of inhomogeneous magnetic field, we performed a series of one-dimensional and two-dimensional simulations using the implicit particle-in-cell (iPIC3D) code. Both initial conditions and boundary conditions are explored. A one-dimensional system with a uniform background magnetic field and either a uniform or localized plasma distribution is studied. For the localized plasma distribution the wave packets propagation is affected by the presence of the edge density gradient. A two-dimensional self-consistent simulation with curved magnetic field and localized plasma distribution is performed and analyzed. After the development of the whistler instability and the propagation of transmitted and reflected wave packets, at a later time the frequency spectrum shifts to higher frequencies due to wave-wave interaction of wave-packets that are artificially reflected from the boundary of the system.

Keywords: particle-in-cell, whistler wave

1. Introduction

Whistler mode waves are electromagnetic emissions frequently observed in the inner magnetosphere. The frequency of whistler waves is between ion gyro-frequency and electron gyro-frequency. The whistler waves with narrow band of frequency-time spectrum are called chorus waves, which are often observed outside the plasmapause in the dawn sector ((Meredith et al., 2001)).

Chorus waves are important for both electrons acceleration and precipitation in radiation belt. It has been observed that chorus waves can accelerate electrons to relativistic speed in the outer radiation belt (Horne and Thorne, 1998; Horne et al., 2005; Thorne et al., 2013). Chorus wave can also scatter energetic particles into loss cone, and cause the electrons' precipitation to the ionosphere, which is an important source of aurora (Thorne et al., 2010). It has been generally accepted that the chorus waves are generated by the temperature anisotropy of electrons (Omura et al., 2008), which may be introduced by the injections of plasma sheet electrons from the tail of magnetosphere (Horne and Thorne, 2003; Jordanova et al., 2010).

Several numerical models have been developed to study the generation and evolution of chorus waves. The Vlasov-hybrid simulation has been used to generate both rising-tone and falling-tone successfully (Nunn, 1990; Nunn

and Omura, 2012). Katoh and Omura (2007) used a 1D electron hybrid code, in which the background cold electrons are described as a fluid while the energetic electrons are treated as particles, to generate rising-tone chorus. This one-dimensional code assumes an azimuthal symmetric parabolic field to represent the spatial inhomogeneity of Earth's dipole field. Using the same field configuration, Hikishima et al. (2009) performed a full particle-in-cell (PIC) simulation, and Tao (2014) used a hybrid code, DAWN, studied the wave intensity variation of chorus waves. However, all these models are one-dimensional, and they are not fully self-consistent when dealing with a spatially varying magnetic field. To get more self-consistent results, Wu et al. (2015) used a two-dimensional hybrid code to study the generation and propagation of chorus waves on a generalized coordinate system.

During the geomagnetic active times, the energetic particles injected from the tail to the ring current may become anisotropic because of the inhomogeneity of the background magnetic field. These electrons with temperature anisotropy can generate chorus waves due to the whistler anisotropy instability (Gary and Wang, 1996). The waves are generated and propagates on the dipole field, and the non-uniform background field leads to the rising-tone chorus waves (Katoh and Omura, 2007). Our final goal is to understand the development of the electron anisotropy, the role of inhomogeneous magnetic field, the generation and propagation of whistler wave. As a preliminary study, we use the implicit particle-in-cell (iPIC3D) code (Markidis et al., 2010) to learn about the generation and propagation of the chorus wave on both uniform and spatially varying background magnetic field.

In the next section, the iPIC3D code is briefly introduced. Section 3 describes the simulation setup, and discusses the simulation results. Finally the conclusion is presented in section 4.

2. The implicit particle-in-cell (iPIC3D) code

$$\nabla \cdot \vec{E} = 4\pi\rho \tag{1}$$

$$\nabla \cdot \vec{B} = 0 \tag{2}$$

$$\frac{\partial \vec{B}}{\partial t} = -c\nabla \times \vec{E} \tag{3}$$

$$\frac{\partial \vec{E}}{\partial t} = c\nabla \times \vec{B} - 4\pi\vec{J} \tag{4}$$

$$\frac{d\vec{p}}{dt} = q(\vec{E} + \frac{\vec{V} \times \vec{B}}{c}) \tag{5}$$

The particle-in-cell (PIC) method has been extensively used in the plasma physics field. It directly solves the Maxwell's equations (eq. (1) to eq. (4)) to update electromagnetic field, and moves particles via Newton's equation (eq. (5)). The basic idea of PIC is not difficult. Super-particles[1] are moving around on the grid following the Newton's equation, and the fields are updated based on the charge density and current, which are determined by super-particles. The disadvantage of PIC is that it is very time consuming because most computational time is used to move super-particles and many super-particles are needed to suppress the statistical noise. Explicit methods are widely used to solve these time-evolution equations. However, the explicit particle-in-cell method is suffering from the stability constraints (Lapenta, 2012):

- The Courant - Friedrichs - Lewy (CFL) condition: $\Delta t < \frac{\Delta x}{c}$.

- Time step should be small enough to resolve the highest frequency motion, which is plasma frequency here: $\Delta t < \frac{2}{\omega_{pe}}$.

- Finite grid instability: $\Delta x < c_0\lambda_{De}, c_0 \sim \pi$.

These constrains limit both spatial resolution (Δx) and time step (Δt), so it is very difficult for explicit particle-in-cell code to simulate large scale system. To break down these constrains, we need to solve the time-evolution equations

---

[1]A super particle is a computational particle that represents many real particles

in a implicit manner. Markidis et al. (2010) developed the iPIC3D code, it transforms the Maxwell's equations into a second order derivative form:

$$\frac{\partial^2 \vec{E}}{\partial t^2} = c^2 \nabla^2 \vec{E} - 4\pi \frac{\partial \vec{J}}{\partial t} - 4\pi c^2 \nabla \rho \tag{6}$$

and update the electric field with an implicit solver. Particles are also moved implicitly. So, the iPIC3D code is unconditionally stable and not limited by the constrains we discussed above, and large grid size and time step can be used, which is important for large scale simulations. In practice, the iPIC3D code still needs to satisfy the accuracy constraint: $\Delta t < \Delta x / v_{th}$, where v_{th} is the thermal velocity of particles, in order to get accurate results. Since the time step is not limited by the stability constrains, it can be larger than particle gyro-period. To ensure the gyro-motion is resolved, the sub-cycling technique is used (Peng et al., 2015) in iPIC3D.

3. Simulation setup and Results

We want to simulate how the chorus waves develop when anisotropic energetic electrons are injected into the ring current. But it is not trivial to get the background equilibrium distribution as initial condition nor to set proper boundary conditions. Non-equilibrium initial condition may drive instabilities, and the boundary conditions are also crucial for PIC simulations (Naitou et al., 1979). As a preliminary study, we focus on the injected anisotropic electrons and ignore the background cold electrons. Since the injected electrons are concentrated on the Earth's equator, we only initialize the anisotropic particles in a small region near the center of the simulation domain. These simplifications avoid the difficulty of setting initial equilibrium initial condition for background plasma. We also use some simple boundary conditions, like periodic boundary or Neumann boundary. We will explore the role of boundary conditions in the future.

3.1. 1D simulation with uniform background

We started from a 1D simulation with uniform background density and magnetic field. Because it is easy to setup and can give us some basic knowledge about both numerical parameters and physics of whistler waves. The simulation is initialized with uniform background magnetic field $\vec{B} = (0, 0, 150)$nT on a domain with $L_Z = 500c/\omega_{pe}$. The electrons are initialized with uniform density $n_e = 6cm^{-3}$, and anisotropy temperature $T_\parallel = 1kev$ and $T_\perp = 4kev$. Cold ions with the same number density are used to keep charge neutrality. Based on our numerical experiments, we choose $\Delta z = 0.05c/\omega_{pe}$, $\Delta t = 0.13\omega_{pe}^{-1}$ and 1000 super-particles in each cell. Periodic boundary conditions are used for both fields and particles.

The simulation results at $t = 248/\Omega_{ce}$[2] is shown in Figure 1. The whistler waves generate the fields perpendicular to the propagation direction, and the non-zero parallel electric filed E_z is caused by statistic noise. We can see that the disturbed perpendicular fields form several wave packets. The wave observed at the middle point of the simulation domain is shown in Figure 2. We can see the chorus wave develops from uniform background and forms several wave packets. The frequency of the waves are about $0.4\Omega_{ce}$ or $0.45\Omega_{ce}$ (bottom of Figure 2), which is the frequency of a typically chorus wave. Further analysis shows that different frequencies corresponding to different wave-packets. We also analyze the dominant wave mode in the simulation domain, and found it shifts from large wavenumber ($k_{dominant} \sim 1.2\omega_{pe}/c$ at $t = 50\Omega_{ce}^{-1}$) to small wavenumber ($k_{dominant} \sim 0.8\omega_{pe}/c$ at $t = 125\Omega_{ce}^{-1}$), which is consistent with previous studies (Lu et al., 2010).

3.2. 1D simulation with localized plasma distribution

Using the same background magnetic field and numerical parameters, we only distribute particles uniformly in the middle ($200 < z < 300$) of the domain. Since electrons have larger thermal velocity than ions, we may expect charge separation at the edges of the plasma distribution.

The results at $t = 248/\Omega_{ce}$ are shown in Figure 3. As we expected, the charge separation appears and builds localized electric field in z direction, which is the same order as the noise. Figure 4 shows the B_y wave in a time-space plane. The waves grow and propagate toward both sides. When the wave reach the shape density gradient locations, part of the wave is transmitted and part of the wave is reflected. The reflected wave may interact with other waves.

---

[2]Time is normalized by ω_{pe} in the code, but we show the results in terms of Ω_{ce} in this report.
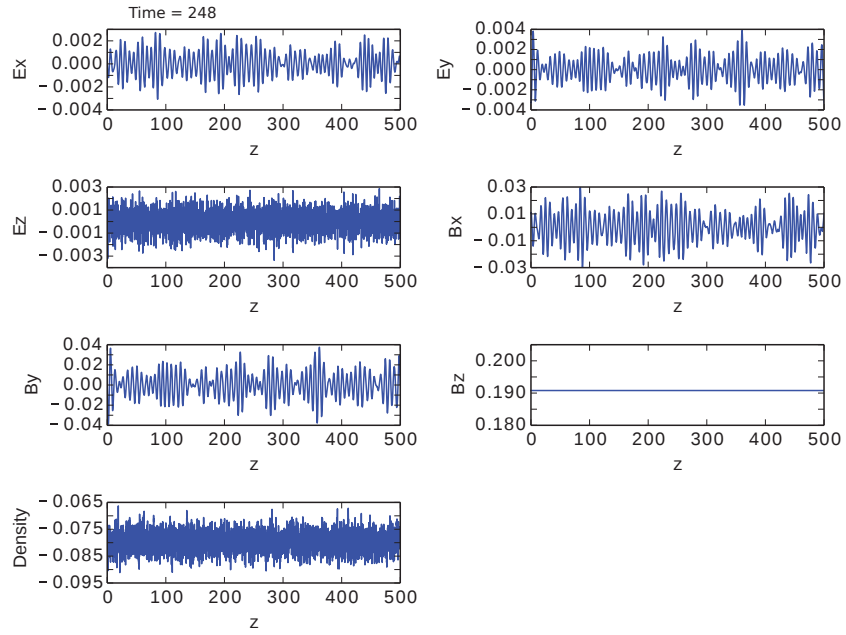
Figure 1: The generation of whister wave on 1D grid with uniform background magnetic field. Results at $t = 248\Omega_{ce}^{-1}$ are shown. The unit of length is c/ω_{pe}. Note that all the values are in normilized units.
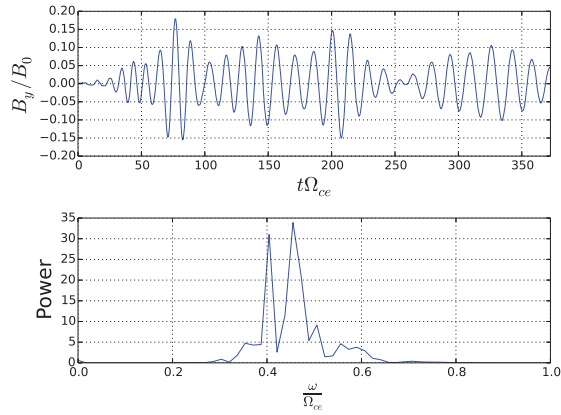
Figure 2: Top: the wave observed at the middle of the simulation domain. Bottom: The frequency spectrum.
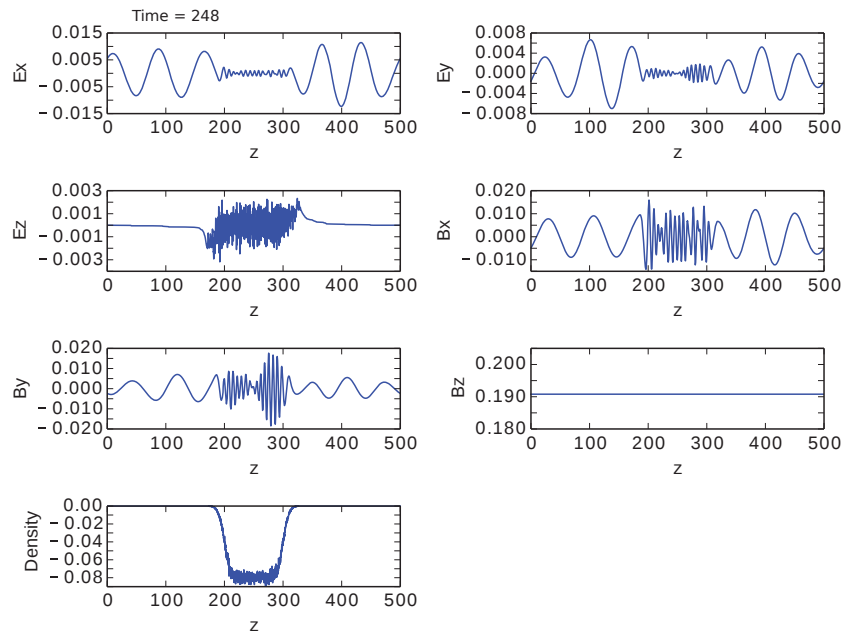
Figure 3: Simulation results at $t = 248\Omega_{ce}^{-1}$ for locally distributed plasma.
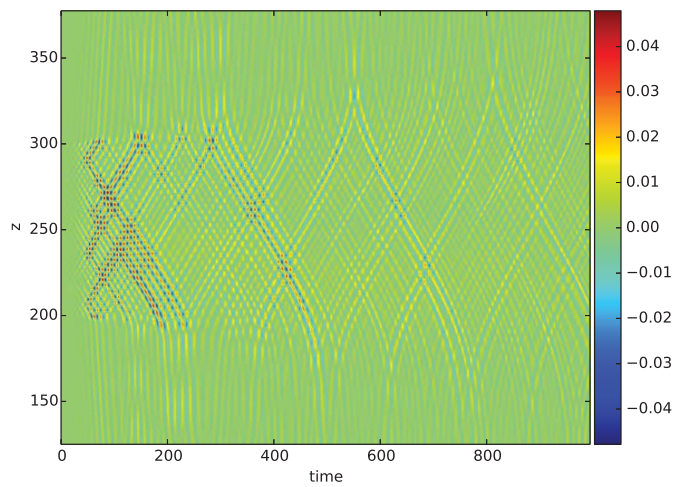
Figure 4: B_y for the whole domain as a function of time.
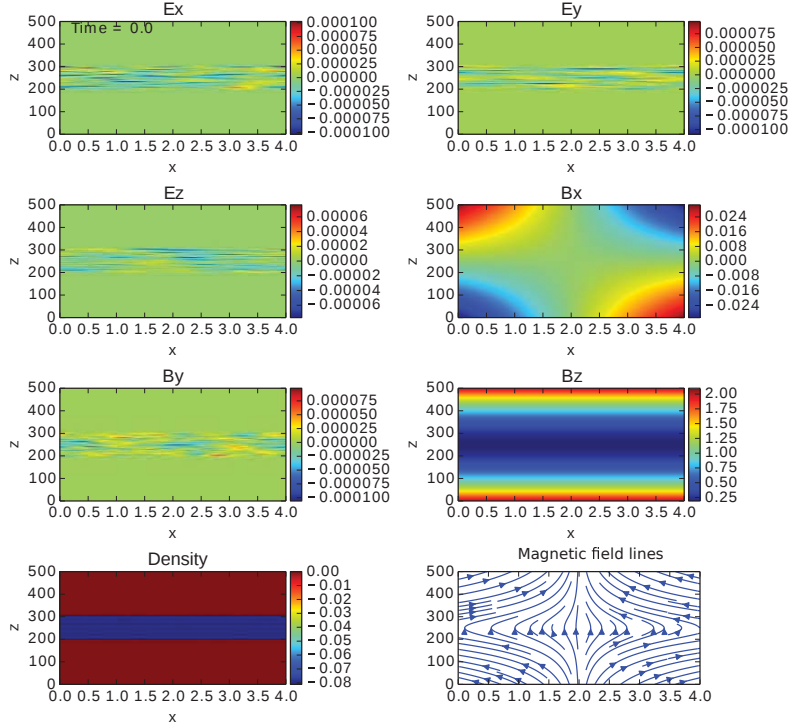
Figure 5: The initial condition for the 2D simulation with curved magnetic field.

3.3. 2D curved magnetic field

A 2D simulation with curved background magnetic field, which mimics the dipole field of Earth, is conducted. The simulation domain is $(x, z) \in [0, 4] \times [0, 500]$. The initial condition is shown in Figure 5, and the background field is

$$B_x = 2c_0 x(250 - z)B_0$$
$$B_y = 0$$
$$B_z = (1 + c_0(z - 250)^2)B_0$$

where $B_0 = 250nT$ and $c_0 = 1.6 \times 10^{-5} c^{-2} \Omega_{ce}^2$. The background field is similar to the one used by Katoh and Omura (2007), except that B_y is always zero here. The plasma is only uniformly distributed between $z = 200$ and $z = 300$. Since the background magnetic field does not change too much for $(x, z) \in [0, 4] \times [200, 300]$, this initial distribution will not cause significant instability during the simulation. In z direction, Neumann boundary is applied for disturbed fields and open boundary is used for particles. Other simulation parameters are the same as these 1D simulations.

The wave observed at $x = 2c/\omega_{pe}$ and $z = 260c/\omega_{pe}$ is shown in Figure 6, where we can also see the formation of chorus wave packets. Interestingly, the frequency shifts from about $0.6\Omega_{ce}$ at $t \sim 80\Omega_{ce}^{-1}$ to $1.3\Omega_{ce}$ at $t \sim 220\Omega_{ce}^{-1}$. This turns out to be related to the boundaries and caused by the wave-wave interaction, which can be seen from Figure 7. Figure 7 shows B_y along z direction as a function of time. Similar to the 1D case, waves can be reflected when density gradient becomes large. At $t \sim 220\Omega_{ce}^{-1}$ and $z \sim 260c/\omega_{pe}$. The reflected waves create the wave observed at $z \sim 260$ with very high frequency.
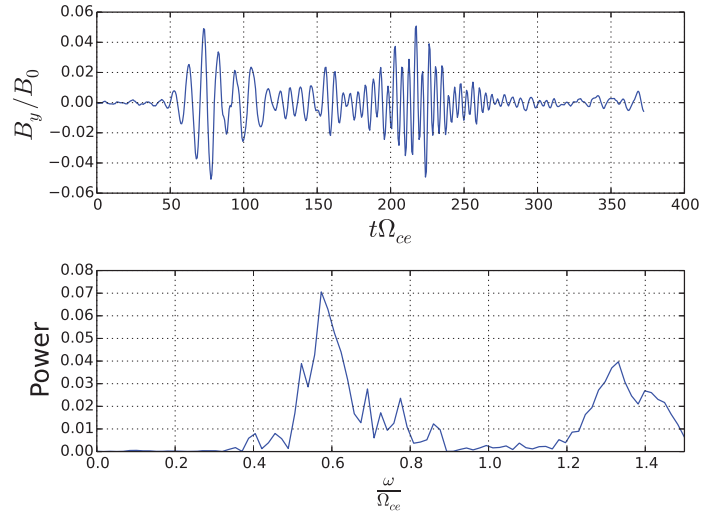
Figure 6: Top: B_y ovserved at $x = 0$ and $z = 260$. Bottom: the spectral power of B_y.
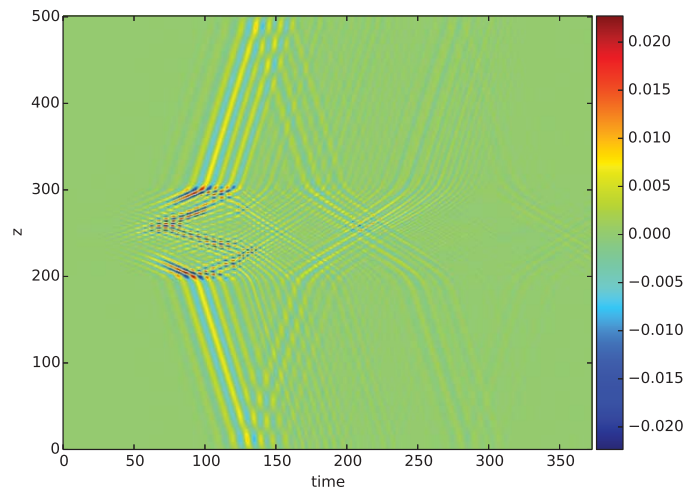
Figure 7: The wave B_y in the 2D simulation along z direciton as a function of time.

4. Conclusion

As the first step to study the development of anisotropy, the role of inhomogeneous magnetic field, and the generation and propagation of whistler waves, we conducted a series of one-dimensional and two-dimensional particle-in-cell simulations that start from a bi-Maxwellian plasma with a predefined level of temperature anisotropy. The whistler instability then develops and chorus wave packets are observed.

We explored the influence of the initial and boundary conditions of the system. In particular, we have studied a one-dimensional system with a uniform background magnetic field and either a uniform or localized plasma distribution. The early behavior of the system is similar in both cases, but for the localized plasma distribution the wave packets propagation is affected by the presence of the edge density gradient and transmitted and reflected wave packets develop. A two-dimensional self-consistent simulation with inhomogeneous background magnetic field and localized plasma distribution is performed, showing the importance of the boundary conditions in the system. After the development of the whistler instability and the propagation of transmitted and reflected wave packets, at a later time the frequency spectrum shifts to higher frequencies due to wave-wave interaction of wave-packets that are artificially reflected from the boundary of the system.

Future work will focus on characterizing the transmitted/reflected wave packets and the role of the inhomogeneous magnetic field.

References

Gary, S.P., Wang, J., 1996. Whistler instability: Electron anisotropy upper bound. Journal of Geophysical Research: Space Physics (1978–2012) 101, 10749–10754.

Hikishima, M., Yagitani, S., Omura, Y., Nagano, I., 2009. Full particle simulation of whistler-mode rising chorus emissions in the magnetosphere. Journal of Geophysical Research: Space Physics (1978–2012) 114.

Horne, R., Thorne, R., 2003. Relativistic electron acceleration and precipitation during resonant interactions with whistler-mode chorus. Geophysical research letters 30.

Horne, R.B., Thorne, R.M., 1998. Potential waves for relativistic electron scattering and stochastic acceleration during magnetic storms. Geophysical Research Letters 25, 3011–3014.

Horne, R.B., Thorne, R.M., Shprits, Y.Y., Meredith, N.P., Glauert, S.A., Smith, A.J., Kanekal, S.G., Baker, D.N., Engebretson, M.J., Posch, J.L., et al., 2005. Wave acceleration of electrons in the van allen radiation belts. Nature 437, 227–230.

Jordanova, V., Thorne, R., Li, W., Miyoshi, Y., 2010. Excitation of whistler mode chorus from global ring current simulations. Journal of Geophysical Research: Space Physics (1978–2012) 115.

Katoh, Y., Omura, Y., 2007. Computer simulation of chorus wave generation in the earth's inner magnetosphere. Geophysical research letters 34.

Lapenta, G., 2012. Particle simulations of space weather. Journal of Computational Physics 231, 795–821.

Lu, Q., Zhou, L., Wang, S., 2010. Particle-in-cell simulations of whistler waves excited by an electron κ distribution in space plasma. Journal of Geophysical Research: Space Physics (1978–2012) 115.

Markidis, S., Lapenta, G., Rizwan-Uddin, 2010. Multi-scale simulations of plasma with ipic3d. Mathematics and Computers in Simulation 80, 1509–1519.

Meredith, N.P., Horne, R.B., Anderson, R.R., 2001. Substorm dependence of chorus amplitudes- implications for the acceleration of electrons to relativistic energies. Journal of geophysical research 106.

Naitou, H., Tokuda, S., Kamimura, T., 1979. On boundary conditions for a simulation plasma in a magnetic field. Journal of Computational Physics 33, 86–101.

Nunn, D., 1990. The numerical simulation of vlf nonlinear wave-particle interactions in collision-free plasmas using the vlasov hybrid simulation technique. Computer Physics Communications 60, 1–25.

Nunn, D., Omura, Y., 2012. A computational and theoretical analysis of falling frequency vlf emissions. Journal of Geophysical Research: Space Physics (1978–2012) 117.

Omura, Y., Katoh, Y., Summers, D., 2008. Theory and simulation of the generation of whistler-mode chorus. Journal of Geophysical Research: Space Physics (1978–2012) 113.

Peng, I.B., Markidis, S., Vaivads, A., Vencels, J., Amaya, J., Divin, A., Laure, E., Lapenta, G., 2015. The formation of a magnetosphere with implicit particle-in-cell simulations. Procedia Computer Science 51, 1178–1187.

Tao, X., 2014. A numerical study of chorus generation and the related variation of wave intensity using the dawn code. Journal of Geophysical Research: Space Physics 119, 3362–3372.

Thorne, R., Li, W., Ni, B., Ma, Q., Bortnik, J., Chen, L., Baker, D., Spence, H.E., Reeves, G., Henderson, M., et al., 2013. Rapid local acceleration of relativistic radiation-belt electrons by magnetospheric chorus. Nature 504, 411–414.

Thorne, R.M., Ni, B., Tao, X., Horne, R.B., Meredith, N.P., 2010. Scattering by chorus waves as the dominant cause of diffuse auroral precipitation. Nature 467, 943–946.

Wu, S., Denton, R., Liu, K., Hudson, M., 2015. One-and two-dimensional hybrid simulations of whistler mode waves in a dipole field. Journal of Geophysical Research: Space Physics 120, 1908–1923.

Hybrid simulations of the right-hand ion cyclotron anisotropy instability in a sub-Alfvénic plasma flow

Ravindra T. Desai

Mullard Space Science Laboratory, University College London, Holmbury St Mary, RH5 6NT, UK

Misa M. Cowee

Los Alamos National Laboratory, Los Alamos, New Mexico, 87545, USA

Abstract

This report outlines a study of the right-hand ion cyclotron anisotropy instability driven by negatively charged ions in a sub-Alfvénic plasma flow. A set of hybrid Particle-In-Cell simulations are performed on a multi-ion plasma consisting of anisotropic ring and maxwellian distributions of positive and negative ions. It was found that the right-hand instability acts in an analogous manner to the left-hand instability with comparable growth and saturation rates as predicted by linear dispersion theory. Comparable fluctuations in the electromagnetic fields were also observed indicating equivalent wave-particle interactions. A number of complexities arose when both instabilities were generated within the same system. The resultant waves displayed a combination of left and right-hand polarisations and gyrophase bunching was identified as introducing electrostatic effects which resulted in significant and periodic magnetic field oscillations and wave amplitudes > 50% greater than expected. Simulated scaling of the wave energy with ring densities and anisotropies was consequently shown to provide a potential method for diagnosing plasma conditions in environments containing both positive and negative ions.

Keywords: Sub-Alfvénic flow, Ion Cyclotron Wave, Wave Polarisation

1. Introduction

The electromagnetic ion cyclotron anisotropy instability is driven by a $T_\perp > T_\parallel$ anisotropy in the distribution function of an ion species. Anisotropic ion populations can be created by the ionisation of neutral atoms where the newly formed ions are accelerated orthogonally to ambient electric and magnetic fields. The ions are thus energised and, for a sufficiently high plasma beta, generate a number of electromagnetic instabilities (Gary et al, 1987). The left-hand ion cyclotron instability has been studied extensively for the cases of single and multi, light and heavy-ion plasmas (Gary et al, 1989; Cowee et al, 2012; Omidi et al, 2010), and has been observed in-situ in a number of space environments (Huddleston et al. 1997; Leisner et al. 2006). This paper reports a study on the properties of the left and right-hand ion cyclotron instabilities in a multi-ion sub-Alfvénic plasma flow consisting of anisotropic distributions of both positive and negative ions.

In the Solar Wind the ion cyclotron instability is a ubiquitous feature (Jian et al. 2010; Volwerk et al. 2013). Solar wind ions can possess large supra-Alfvénic velocity components parallel to the interplanetary magnetic field which results in a Doppler shift between the plasma frame and the observing spacecraft. This frequency shift can cause the waves to be observed as right-handed polarised although they are left-hand polarised in the plasma frame.

In the Earth's magnetosphere, anisotropic ring current ions are unstable to the generation of ion cyclotron waves (Horne and Thorne, 1993). The anisotropies involved in this process however are significantly lower than when the

instability is generated by the ionisation of neutrals. These waves are at the outset left-hand polarised but can undergo polarisation reversals if they pass through the crossover frequency of the multi-ion plasma in which they are generated (Hu and Denton 2009). As they propagate outwards from the equatorial regions right-hand polarised waves can thus be observed.

In Jupiter's and Saturn's magnetospheres, ion cyclotron waves are generated by the ionisation of neutral material (Huddleston et al. 1997; Leisner et al. 2006). The predominantly dipolar magnetic field configurations and corotational electric fields result in a 'perpendicular' sub-Alfvénic pickup geometry. The anisotropic ions form rings in velocity space unstable to the generation of left-handed ion cyclotron waves which act to scatter and diffuse the ion pitch angle distributions, restoring thermal equilibrium.

In the vicinity of the Jovian moon Europa, Galileo wave observations displayed bursty characteristics at the gyrofrequency of a number of species including O_2, SO_2, K, Na and Cl, (Volwerk et al, 2001). At the gyrofrequency of chlorine the wave ellipticity alternated between negative and positive values, the waves displaying both left and right-hand polarisations. The absence of polarisation reversals at the gyrofrequency of other elements led to this phenomena being attributed to the presence of both positive and negative chlorine ion populations. This inference is supported by the high electron affinity and stable configuration of the chlorine anion, Cl^-, the additional electron filling the atoms outer d-shell. Negatively charged halogens, including chlorine, are also known to be abundant in the Earth's D region (Kopp and Fritzenwallner, 1997).

This paper outlines a study investigating the behaviour of the ion cyclotron anisotropy instability driven by heavy positive and negative ion rings in the Europan plasma environment. Using a hybrid simulation code and drawing comparisons to linear dispersion theory we answer the following questions: Do anisotropic negative ion distributions generate the right-hand ion cyclotron instability? Does this instability have fundamentally differently properties to the left-hand cyclotron instability other than the wave polarisation? Is there any interaction between the left and right-hand instabilities when they are generated in the same system? Following this we examine whether it is possible to estimate ion densities at Europa from the wave amplitudes observed by the Galileo spacecraft, using simulated scaling of the wave energy with ring densities and anisotropies.

2. Methodology

Linear dispersion theory is able to predict the frequencies and growth rates of the ion cyclotron anisotropy instability but is unable to predict wave-particle interactions (Huddlestone et al, 1998). To capture these effects Particle-In-Cell (PIC) simulations are employed, a simulation technique which has extensively been applied to the study of positive ion rings generating left-handed ion cyclotron waves (Cowee et al, 2006, 2009, 2010, 2012). The hypothesis in this investigation is that negative ion rings will conversely generate right-handed waves, as was the inference in Volwerk et al, 2001.

The hybrid code developed by Winske & Omidi, 1993, is used in this analysis and has been successfully shown to reproduce the ion cyclotron anisotropy instability in a number of plasma environments (Gary et al, 1989; Omidi et al, 2010; Cowee et al, 2012). Ions are specified kinetically with electrons approximated as a massless neutralising fluid, an approach suited to capturing phenomena at the ion spatial and temporal scales. In this study the particle positions are resolved along one spatial dimension aligned with the magnetic field, B_0, and the electromagnetic fields are resolved in three dimensions. This approach is justified as linear dispersion theory predicts main wave power at parallel propagation (Gary and Madland, 1988). Simulating three dimensions would capture more modes but it has been shown that in one dimension the physical relation between relative changes in wave amplitudes and growth rates will remain unchanged with respect to varying background plasma conditions (Cowee et al, 2006).

In the PIC simulations, particles properties are collectively approximated by between $10^7 - 10^8$ superparticles upon 512 grid cells specified across ~40 proton inertial length scales, c/ω, and timesteps specified as a function of the ion cyclotron frequency, Ω_j, where j denotes the ion species. These interpolated ion properties are subsequently used as inputs to Darwin's approximation of the field equations.

In this analysis the plasma considered consists of multiple ion species, either in a zero drift maxwellian distribution or a ring distribution with $T_\perp > T_\parallel$. Each species has mass, m_j, and charge state, Z_j, normalised to the proton scale with perpendicular and parallel velocities defined as $V_{\parallel j} = (2k_B T_{\parallel j}/m_j)^{1/2}$, and $V_{\perp j} = (2k_B T_{\perp j}/m_j)^{1/2}$. The temperature anisotropy, $A_j = T_{\perp j}/T_{\parallel j}$, is specified according to the corotational plasma velocity of the Jovian magnetodisk at $\sim 10 R_J$. Further plasma parameters specified are the plasma beta, $\beta_j = 2\mu_0 n_0 T_{\parallel j}/B_0^2$,, and the Alfven velocity, $V_a = B_0/\sqrt{\mu_0 n_o m_j}$.

Table 1 and 2 shows the simulation and plasma parameters defined to be characteristic of the sub-Alfvénic Europan plasma interaction as observed by Galileo. The background plasma species, densities and bulk velocities are based upon values taken from Paterson, 1999, Kivelson et al, 2009, and Bagenal et al, 2015, and are not expected to play a significant role in the generation of the ion cyclotron instabilities. Three different simulations are carried out in this study to examine the growth of this instability under varying conditions. In run I a positive maxwellian chlorine core and anisotropic chlorine ring are initialised to examine the growth of the left-handed instability in an isotropic background plasma. In run II a negative chlorine core and ring are initialised to examine the growth of the right-handed instability. In run III a combination of these two are then simulated to explore the effects associated with these two instabilities growing side by side within the same system.

3. Results

Figures 1-5 show the simulation results corresponding to the three different simulation cases outlined in table 1.

Figure 1 shows the full ω-k spectrum normalised to the gyrofrequency of the heavy ion species. In each case the wave power is concentrated at the heavy ion's gyrofrequency demonstrating growth of the ion cyclotron instability as predicted by linear dispersion theory. At this frequency range the right-hand magnetosonic mode is also apparent although the main wave power is concentrated at the cyclotron wave branch. Run I and run II show similar behaviour, thus demonstrating that an anisotropic negative ion distribution will generate the ion cyclotron instability in a comparable manner to an anisotropic positive ion distribution. Run III displays stronger wave power which is expected as there is twice as much free energy within the system.

Figure 2 tracks the temperature evolution of the various species. In each run the chlorine ring ions scatter, their energy reducing in the perpendicular direction and increasing in the parallel direction. The chlorine core species acts to damp the growth of the instability and are consequently heated in the perpendicular direction by a factor of ~ 4. The background core population is not expected to undergo any heating unless it has a gyroperiod which allows it to resonantly interact with the ring species (Huddlestone et al, 1998). In run I this effect is evident in that the similarly charged background species has a mass/charge ratio of a third of the ring species and is consequently heated by a few percent. In run II the oppositely charged ring species does not interact with this background population, the only temperature change of the background species being due to interaction with noise level waves. It is noticeable in run III that the temperature of the background and chlorine core species oscillate strongly. This effect is not predicted by linear dispersion analysis or reported in previous hybrid simulations of the ion cyclotron instability in planetary environments (Cowee et al. 2006, 2009, 2010).

Figure 3 displays the energy-history of the instability as it grows from the noise level and reaches saturation at time equal to $\sim 50 \Omega t$. Run I and run II have similar growth rates, the slight interaction of the positive chlorine ring with the background species not appearing to significantly dampen the growth of the instability. Run III shows a growth rate greater than in run I and run II which is in-line with expectations that an increased ring density should produce stronger wave growth (Huddlestone et al. 1998). The expectation of run III is then that the growth of the wave amplitudes will cease at the combined values of runs I and II. Strong oscillations however are observed throughout run III which significantly increase once the instability has saturated. These oscillations result in energies being reached which are significantly larger than expected, in this instance an increase of $> 50\%$. These oscillations appear at twice the chlorine cyclotron frequency and are consequently identified as the half-length electrostatic mode identified in Omidi et al, 2010, and Bortnik et al, 2010.

Figure 4 shows the helical components of the waveform along the simulation axis stacked in time as the simulations progresses. The magnetic field oscillations are decomposed into their positive and negative helical components to display the rotation of the wave with respect to the wave vector, k. The striations in these plots represent transverse waves which can be seen to increase in magnitude as they move both parallel and anti-parallel to the magnetic field. In run I the waves move towards $-x$ for the positive helical components and towards $+x$ for the negative components, thus displaying left-handed wave polarisations. In run II this motion is reversed, indicating right-handed wave polarisations. Run III shows striations leaning towards both $+x$ and $-x$ which can be seen to intersect one another. This can be taken as evidence that both left-handed and right-handed waves are growing within the system, generated by the positive and negative ion rings respectively. The precise resultant ellipticity however cannot be determined from this analysis and the resultant wave's characteristics therefore require further analysis to determine whether the left and right-handed components combine to form a linearly polarised wave form or whether both left and right-hand polarised waves are periodically present.

Figure 5 displays the phase-space of run III at four times within the simulation run. Gyrophase bunching is evident in this figure with particles being trapped in the parallel direction. This introduces electrostatic effects at twice the anisotropic ion's gyrofrequency as ions possessing opposing helical components intersect one another's path twice within each gyro-orbit. In Omidi et al, 2010, a half-length electrostatic mode was attributed to oppositely directed helical components being produced by waves propagating both parallel and anti-parallel to the magnetic field. This effect appears to be particularly enhanced in a system containing both positive and negative ions with the two instabilities, the left and right-hand ion cyclotron anisotropy instability, growing simultaneously and producing both right and left handed wave propagating in both directions along the field lines.

Figure 6 represents a further study where the ion densities and anisotropies were varied in order to constrain the parameter space within which the ion cyclotron waves were generated at Europa. The growth and saturation of the right-hand ion cyclotron anisotropy instability was found to scale similarly to the left-hand instability with respect to varying ion densities, pickup velocities and anisotropies. This study can be seen to provide a method for diagnosing local plasma conditions from observed wave amplitudes, although further analysis is required to understand the complexities involved in a system containing both positive and negative ions.

4. Conclusions

1D hybrid simulations of positive and negative anisotropic ion distributions were shown to reproduce the left and right-hand cyclotron instability and to reproduce wave-particle interactions which linear dispersion theory does not account for. Spectral analysis of the resultant waves showed left and right-handed ion cyclotron waves were indeed generated by positive and negatively charged anisotropic ion populations. The growing waves were shown to be analogous to one another the difference being the wave polarisation. Significant complexities resulted in simulations which contained both positive and negative ions with the multitude of waves generated not displaying a clear resultant polarisation.

Significant effects were also observed in the interaction between the left and right-handed ion cyclotron anisotropy instabilities. An electrostatic half-length mode was identified as acting at twice the cyclotron frequency which resulted in significantly larger magnetic field amplitudes than anticipated. A scaling study on the effects of varying ion densities and anisotropies was also performed to understand how these changes affected the resultant wave amplitudes once the instability had saturated. This parametric study demonstrated how it was possible to use this simulation technique to constrain the local plasma conditions at Europa, although further analysis is required to understand the electrostatic effects and spectral properties associated with the generation of both the left and right-handed waves within the same system.

References

Bagenal, F, E S, R J. Wilson, T A. Cassidy, V Dols, F. J. Crary, A J. Steffl, P A. Delamere, W S. Kurth, and W R. Paterson. 2015. "Plasma Conditions at Europa's Orbit." *Icarus* 261: 1–13. doi:10.1016/j.icarus.2015.07.036.

Bortnik, J., R. M. Thorne, and N. Omidi. 2010. "Nonlinear Evolution of EMIC Waves in a Uniform Magnetic Field: 2. Test-Particle Scattering." *Journal of Geophysical Research* 115 (A12): A12242. doi:10.1029/2010JA015603.

Cowee, M M, S P Gary, and H Y Wei. 2012. "Pickup Ions and Ion Cyclotron Wave Amplitudes Upstream of Mars: First Results from the 1D Hybrid Simulation." *Geophysical Research Letters* 39 (8): L08104–L08104. doi:10.1029/2012GL051313.

Cowee, M M, R J Strangeway, C T Russell, and D Winske. 2006. "One-Dimensional Hybrid Simulations of Planetary Ion Pickup : Techniques and Verification." *Journal of Geophysical Research* 111: 1–9. doi:10.1029/2006JA011996.

Cowee, M. M., and S. P. Gary. 2012. "Electromagnetic Ion Cyclotron Wave Generation by Planetary Pickup Ions: One-Dimensional Hybrid Simulations at Sub-Alfvénic Pickup Velocities." *Journal of Geophysical Research* 117 (A6): A06215. doi:10.1029/2012JA017568.

Cowee, M. M., S. P. Gary, H. Y. Wei, R. L. Tokar, and C. T. Russell. 2010. "An Explanation for the Lack of Ion Cyclotron Wave Generation by Pickup Ions at Titan: 1-D Hybrid Simulation Results." *Journal of Geophysical Research: Space Physics* 115 (July): 1–12. doi:10.1029/2010JA015769.

Cowee, M. M., N. Omidi, C. T. Russell, X. Blanco-Cano, and R. L. Tokar. 2009. "Determining Ion Production Rates near Saturn's Extended Neutral Cloud from Ion Cyclotron Wave Amplitudes." *Journal of Geophysical Research: Space Physics* 114: 1–10. doi:10.1029/2008JA013664.

Gary, S. P., and C. D. Madland. 1988. "Electromagnetic Ion Instabilities in a Cometary Environment." *Journal of Geophysical Research* 93: 235–41.

Gary, S. Peter, Kazuhiro Akimoto, and Dan Winske. 1989. "Computer Simulations of Cometary-Ion/ion Instabilities and Wave Growth." *Journal of Geophysical Research* 94 (A4): 3513. doi:10.1029/JA094iA04p03513.

Gary, S. P. Shriver, D. 1987. "The Electromagnetic Ion Cyclotron Beam Anisotropy Instability." *Planetary and Space Science* 35 (1): 51–59.

Horne, Richard B., and Richard M. Thorne. 1993. "On the Preferred Source Location for the Convective Amplification of Ion Cyclotron Waves." *Journal of Geophysical Research* 98: 9233–47. doi:10.1029/92JA02972.

Hu, Y., and R. E. Denton. 2009. "Two-Dimensional Hybrid Code Simulation of Electromagnetic Ion Cyclotron Waves in a Dipole Magnetic Field." *Journal of Geophysical Research* 114 (A12): A12217. doi:10.1029/2009JA014570.

Huddleston, D. E., R. J. Strangeway, J. Warnecke, C. T. Russell, M. G. Kivelson, and F. Bagenal. 1997. "Ion Cyclotron Waves in the Io Torus during the Galileo Encounter: Warm Plasma Dispersion Analysis." *Geophysical Research Letters* 24 (17): 2143–46. doi:10.1029/97GL01203.

Huddlestone, D E, R. J. Strangeway, J Warnecke, C T Russell, and M G Kivelson. 1998. "Ion Cyclotron Wave in the Io Torus: Wave Dispersion Analysis and SO2+ Source Rate Estimates." *Journal of Geophysical Research* 103: 887–99.

Jian, L. K., C. T. Russell, J. G. Luhmann, B. J. Anderson, S. a. Boardsen, R. J. Strangeway, M. M. Cowee, and a. Wennmacher. 2010. "Observations of Ion Cyclotron Waves in the Solar Wind near 0.3 AU." *Journal of Geophysical Research: Space Physics* 115 (May): 1–11. doi:10.1029/2010JA015737.

Kivelson, M. G., K. K. Khurana, and M. Volwerk. 2009. "Europa's Interaction with the Jovian Magnetosphere." *Europa*, 545–70.

Kopp, Ernest, and J Fritzenwallner. 1997. "Chlorine and Bromine Ions in the D-Region." *Advances in Space Research* 20 (ll): 2111–15.

Leisner, J. S., C. T. Russell, M. K. Dougherty, X. Blanco-Cano, R. J. Strangeway, and C. Bertucci. 2006. "Ion Cyclotron Waves in Saturn's E Ring: Initial Cassini Observations." *Geophysical Research Letters* 33 (11): L11101. doi:10.1029/2005GL024875.

Omidi, N., R. M. Thorne, and J. Bortnik. 2010. "Nonlinear Evolution of EMIC Waves in a Uniform Magnetic Field: 1. Hybrid Simulations." *Journal of Geophysical Research* 115 (A12): A12241. doi:10.1029/2010JA015607.

Paterson, W. R., L. a. Frank, and K. L. Ackerson. 1999. "Galileo Plasma Observations at Europa: Ion Energy Spectra and Moments." *Journal of Geophysical Research* 104 (A10): 22779. doi:10.1029/1999JA900191.

Volwerk, M, M G Kivelson, and K K Khurana. 2001. "Wave Activity in Europa's Wake: Implications for Ion Pickup" 106 (A11). doi:10.1029/2000JA000347.

Volwerk, M., C. Koenders, M. Delva, I. Richter, K. Schwingenschuh, M. S. Bentley, and K.-H. Glassmeier. 2013. "Ion Cyclotron Waves during the Rosetta Approach Phase: A Magnetic Estimate of Cometary Outgassing." *Annales Geophysicae* 31 (12): 2201–6. doi:10.5194/angeo-31-2201-2013.

Winske, D., and N Omidi. 1993. "Hybrid Codes: Methods and Application." *Computer Space Plasma Physics: Simulation Techniques and Software*.

Table 1: Simulation parameters

c/vA	xmax (km)	nx (km)	Superparticles per cell	B0 (nT)	n0 (1/cc)
344.0	911.115	512	50	400	100

Table 2. Plasma input parameters

j	m_j/m_p	Zj/Zp	β_j	A_j	Run I n_j/n_0	Run II n_j/n_0	Run III n_j/n_0
Background	18.5	1.5	0.021427	1	0.80	0.80	0.60
Cl^+ **core**	36	1	0.021427	1	0.15	-	0.15
Cl^+ **ring**	36	1	0.000126	3656	0.05	-	0.15
Cl^- **core**	36	-1	0.021427	1	-	0.15	0.05
Cl^- **ring**	36	-1	0.000126	3656	-	0.05	0.05
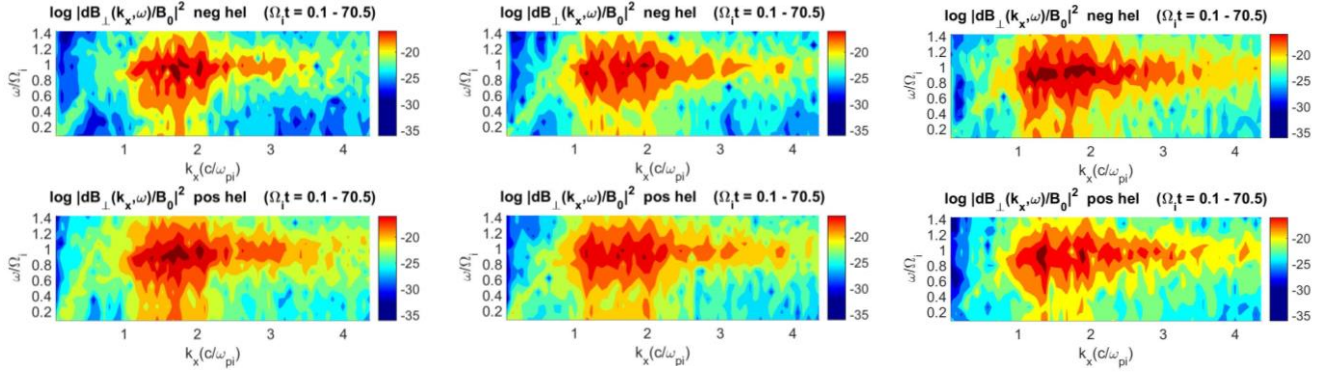
Figure 1: $\omega - k$ spectrum for (left) Run I, (centre) Run II and (right) Run III
normalised to the chlorine cyclotron frequency
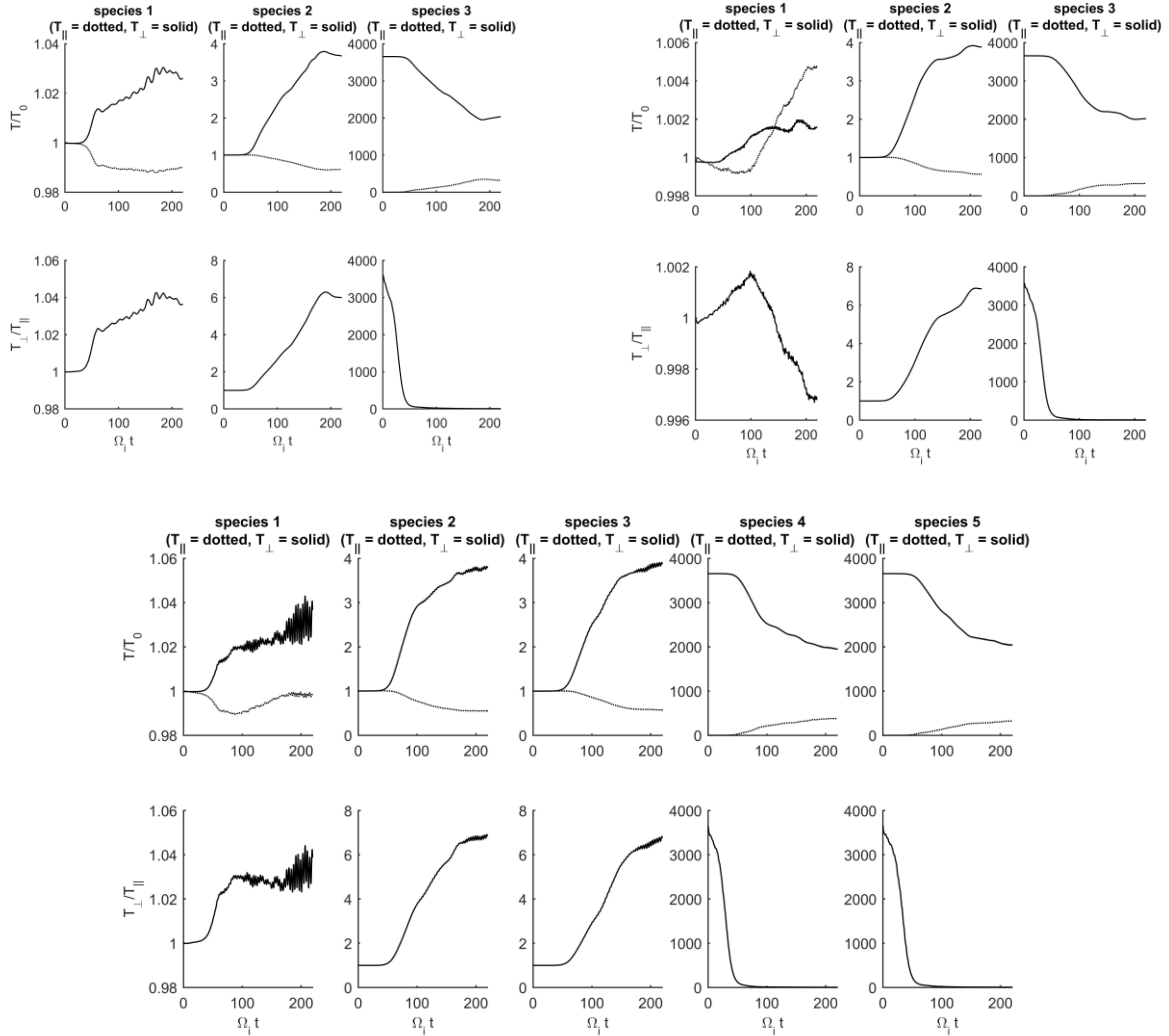
Figure 2: Temperature evolution of (top-left) Run I, (top-right) Run II and (bottom) Run III
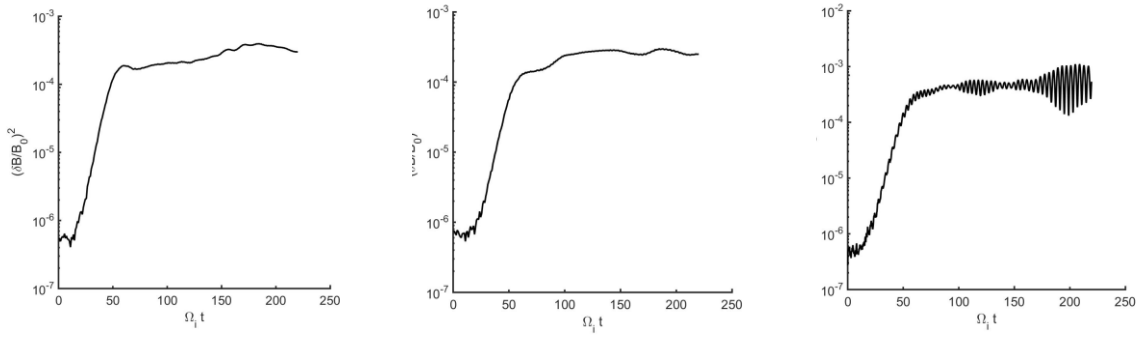
Figure 3: Energy-history of (left) Run I, (centre) Run II, (right) Run III
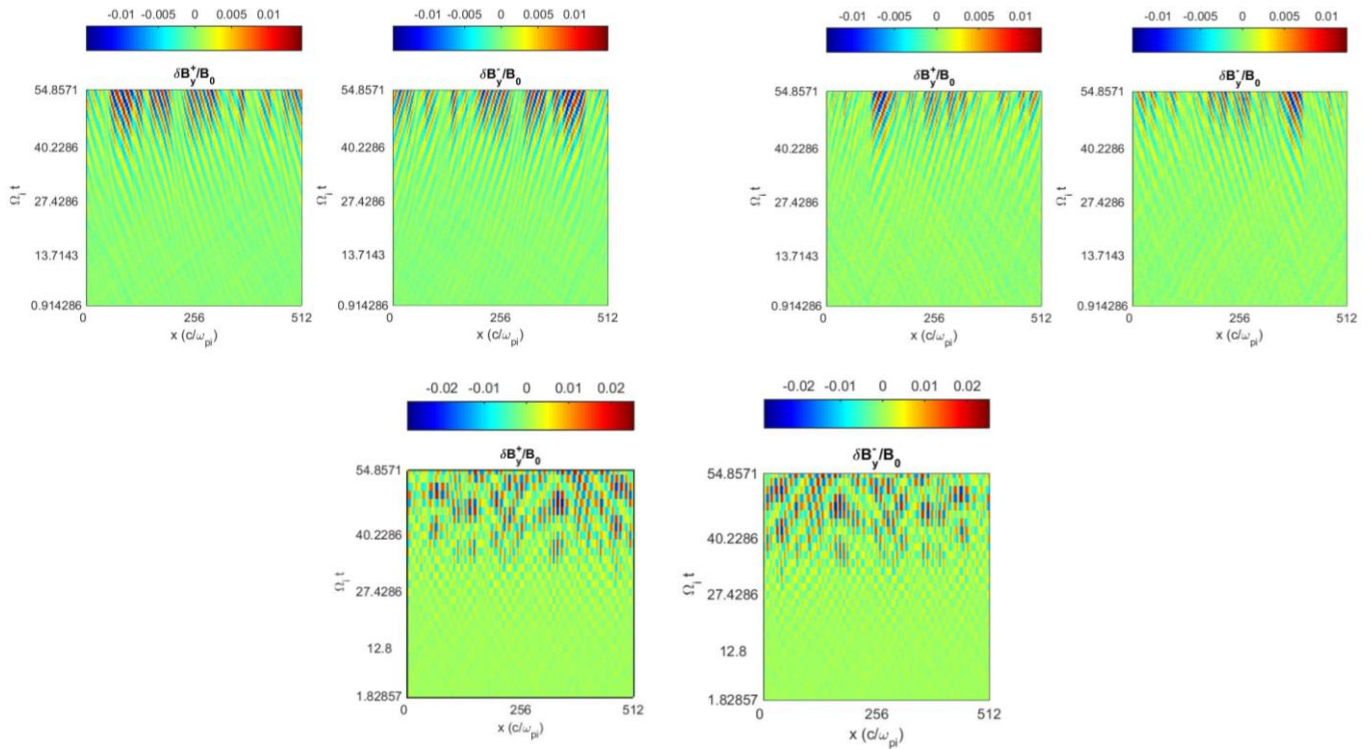
Figure 4: Positive and negative helical components for (top-left) Run I, (top-right) Run II, and (bottom) Run III
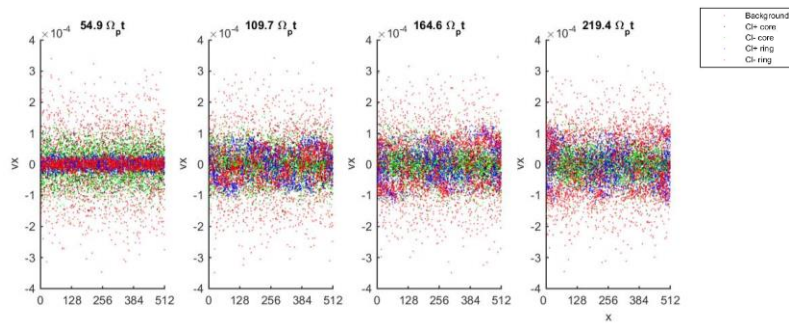
Figure 5: Phasespace of Run III
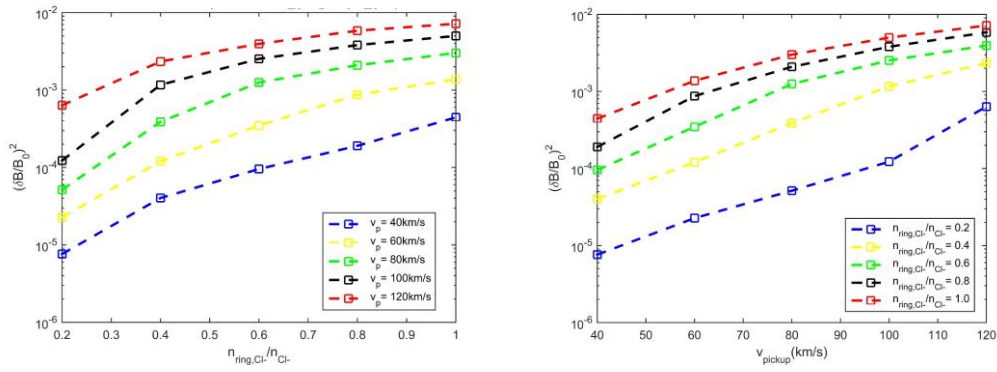
Figure 6: Parametric study of the saturation energy dependence of the instability with respect to variations in the pickup velocity and ring density

A Statistical Ensemble for Solar Wind Measurements
A Step toward Forecasting

Ehab Hassan

Dept. of Physics, University of Texas at Austin, TX, USA

Steven K. Morley and John T. Steinberg

Space Science and Applications (ISR-1), Los Alamos National Laboratory, USA

Abstract

Knowing the upstream solar wind condition is essential in forecasting the variations in the geomagnetic field and the status of the Earth's ionosphere. The solar wind measurements at the bow shock nose can be used in many data-driven simulations for the purpose of space weather forecasting. However, there is no monitoring station consistently at that location, and also it might not be practical to have a monitoring station that close to the Earth. The presence of a solar wind monitoring station near the first Lagrangian point (L1), such as Advanced Composition Explorer (ACE), does the same job if we can adequately propagate the solar wind to the bow shock nose. However, measurements at L1 will not necessarily impact the magnetosphere so an estimate of the solar wind parameters at the bow shock nose, given the measurements at L1, is desirable. We used three years of solar wind data measured by the Advanced Composition Explorer (ACE) and advected them to the location of the Interplanetary Monitoring Platform (IMP8) spacecraft, just upstream of Earth. The concurrent advected ACE data and IMP8 measurements are used to to establish Kernel Density Estimation (KDE) functions of solar wind parameters just upstream of the magnetopause, given the value measured at ACE. The location of the IMP8 spacecraft allows us to use these KDE functions to generate ensembles of solar wind data at the Earth's magnetopause that can be used to forecast the status of the geomagnetic field and the ionosphere. In addition, we employed a solar wind categorization scheme for the incoming solar wind data to established KDE functions for each of 4 categories and compared them with the uncategorized KDE functions.

1. Introduction

Space weather forecasting found its way to be a top priority research due to its great impact on the modernized technology we have nowadays [Baker 2000, Coster *et al.* 2003, Welling 2010]. Besides the heat flux and visible light the Sun emits, there are other active solar phenomena such as the solar flares and coronal-mass-ejections that might cause a great impact on Earth's system. The connection between the solar activities and their impacts on the Earth's system was first considered by Carrington [1859] who reported observing a flare in visible light that was followed hours later by a very large geomagnetic disturbance.

One aspect of solar behavior that occurs continuously is the solar wind, which is the outflow of plasma from the area of open magnetic field lines in the solar corona [Kivelson and Russel 1995]. Historically, the solar wind is classified according to its region of origin within the corona. The fast solar winds are emerging from coronal holes, which are always present at the solar poles, and which cover most of the Sun during the solar minimum. The fast solar winds are characterized by their low-density plasma and speed ranges in 450-850 km/s. In contrast, the plasma density in the slow solar wind is comparatively larger, its speed typically lies in the range 250-450 km/s and its origin is still controversial [e.g. Schwenn 2007]. According to the recent categorization scheme proposed by Xu and Borovosky [2015], the slow

solar wind can be subdivided into two subcategories: streamer-belt-origin and sector-reversal-region. We will discuss this categorization scheme later. In addition, there is another kind of solar wind called ejecta which are associated with corona-mass-ejections. At times coronal mass ejections take the form of magnetic clouds carrying flux rope magnetic fields that result from the generation mechanism in the solar corona. In addition, the speed and density of these ejecta vary according to the generation mechanism.

Because the solar wind variations happen continously and the interplanetary magnetic field for a plasma parcel is connected to the Sun, the solar wind carries lots of information about its origin on the Sun [Owens and Forsyth 2013]. Also, the impact of the solar wind on the Earth's system varies according to bulk parameters, such as the speed, density, and the interplanetary magnetic field (IMF) vector. Therefore, measuring the upstream solar wind conditions can help in forecasting their impact on the Earth's system. As a result, numerous satellite missions have been sent upstream of Earth to continuously monitor the solar wind conditions.

The interaction between the incoming solar wind and the Earth's system first takes place at the magnetosphere nose, or what is called the bow-shock. The ram pressure and the IMF vector determine the physical nature and the severity of this interaction with the magnetosphere [Dungey 1961 and Farrugia *et al.* 2008]. The magnetic reconnection process that takes place at the bow-shock between the IMF and the geomagnetic field has its largest effect when the IMF is oriented southward (i.e. anti-parallel to Earth's magnetic field) [McPherron *et al.* 2008 and Fuselier *et al.* 2011]. This magnetic reconnection process, which reconfigures the geomagnetic field line on the day-side of the Earth's magnetosphere, is mostly followed by another magnetic reconnection at the geomagnetic tail on the night-side. These continuous magnetic reconnection processes inject a huge shower of energetic particles on the polar caps that give rise to what is called northern lights or aurora borealis [Milan *et al.* 2007 and Pulkkinen *et al.* 2007].

Regarding the impact of the solar wind on the ionosphere, the effect is most pronounced in the po-lar caps [Frey *et al.* 2003]. However, it is found that the impact of the severe interaction between the solar wind and the ionosphere at high-latitudes can extend to the lower magnetic latitudes. Ohtani *et al* [2013] reported an enhancement in the equatorial electrojet current due to a variation on the horizontal component of the geomagnetic field during the transition of IMF orientation from southward to northward. Also, Kelley *et al.* [2003] reported a nighttime variation in the eastward component of the electric field at the magnetic equator that perfectly matches the variation in the calculated Interplanetary Electric Field (IEF).

Thus, the consequences of the interaction of solar wind with the magnetosphere, and in turn on the Earth's ionosphere, is not limited to the high latitudes but it can extend to the low-latitude and equatorial regions. These penetrating IMF and IEF to the low-latitudes might play an important role in driving different types of instabilities or have influence on the established instability mechanisms on these regions. The expected enhancement of the low-latitude and equatorial instabilities provides motivation to study the dynamic variations of different types of solar winds as they propagate from the Sun to the Earth. We consider this work as a step toward forecasting the status of the ionosphere at different latitudes during storm and substorm events based on an ensemble of solar wind data generated from one upstream point measurement.

This paper is organized as follow: In section(II) we give an overview of the categorization scheme proposed by Xu and Borovosky [2015]. Then a comparison between the different techniques that has been used for solar wind advection is presented in section(III). Section(IV) is dedicated for presenting a description for the solar wind dataset we use in our model and the technique we follow to generate the ensemble of the solar wind parameters. We end this paper by a summary and conclusion in section(V) and a proposal of the recommended future work in section(VI).
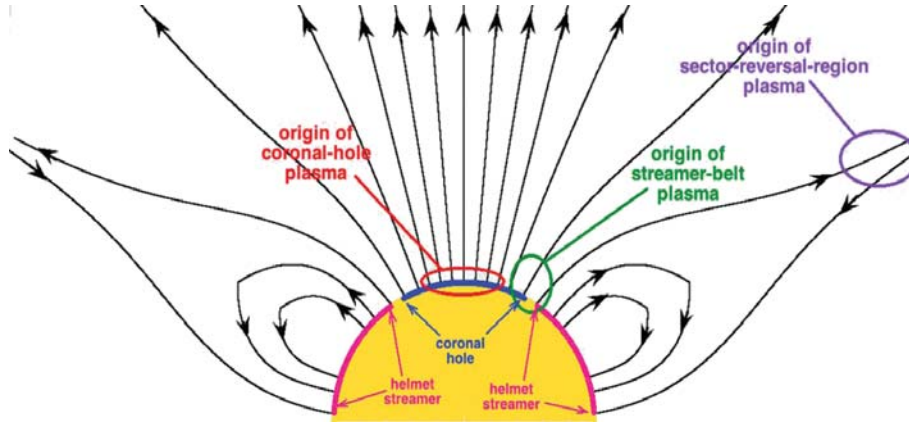
Figure 1: *Four Categories of Solar Wind origins in the Solar Corona. Adapted after Xu and Borovsky [2015]*

2. Solar Wind Categorization Scheme

The solar winds are commonly categorized according to their origin within different regions in the solar corona. Most frequently three categories have been used: ejecta, slow solar wind, and fast solar wind [e.g. Richardson *et al.* 2000, 2001]. The slow winds release from the cusp between the close and open magnetic field lines and are characterized by their low-speed and high-proton-density, and they are also called *streamer-belt-origin* winds. In contrast, the fast solar wind release from the open magnetic field lines which are characterized by their lower proton density and high-speed, and they are called *coronal-hole-origin* winds. On the other hand, the ejecta are associated with *coronal-mass-ejections* from the Sun, which includes magnetic clouds that exhibits different shapes of magnetic ropes [Russell 2001].

Based on twenty-years (1998-2008) of ACE solar wind data, Zhao *et al.* [2009] used the (O^{7+}/O^{6+}) density ratio and the solar wind speed to propose a scheme that categorizes the solar winds into coronal-hole, non-coronal-hole origin plasmas, and ejecta. In 2015, Xu and Borovsky proposed a 4-class categorization scheme for the solar wind plasma. They added a new category based on another solar wind origin called *sector-reversal-region*, as shown in figure(1). The sector-reversal-region is formed within the helmet streamer which separates two coronal holes of opposite polarities and is characterized by its very low proton specific entropy [Xu and Borovsky 2015].

In their categorization algorithm, Xu and Borovsky [2015] used the proton temperature (T_p), proton density (n_p), proton speed (v_p), and the interplanetary magnetic field (B) to calculate the proton specific-entropy (S_p), proton Alfven speed (v_A), and the expected temperature of the proton at a given solar wind speed (T_{exp}). If relationship 1a is satisfied, solar wind is regarding to be ejecta. If the solar wind is not ejecta and equation(1b) is satisfied, the solar wind is categorized as coronal-hole-origin. However the verification of equation(1c) for non-ejecta solar wind identifies sector-reversal-solar winds, and otherwise we have a streamer-belt-origin solar wind.

$$log_{10}(v_A) > 0.277 log_{10}(S_p) + 0.055 log_{10}(T_{exp}/T_p) + 1.83 \tag{1a}$$

$$log_{10}(S_p) > -0.525 log_{10}(T_{exp}/T_p) - 0.676 log_{10}(v_p) + 1.74 \tag{1b}$$

$$log_{10}(S_p) < -0.658 log_{10}(v_A) - 0.125 log_{10}(T_{exp}/T_p) + 1.04 \tag{1c}$$

(a) Solar Maximum (2003)

(b) Solar Minimum (2008)
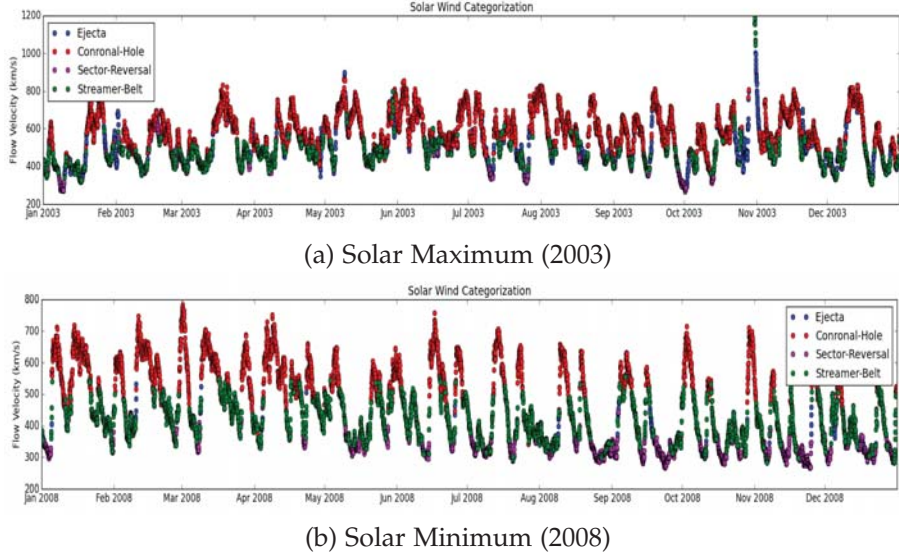
Figure 2: *Testing solar wind data in OMNI dataset against 4-categorization scheme during (a) solar maximum and (b) solar minimum conditions. The wind categorizations are indicated in the figure legend.*

where,

$$S_p = \frac{T_p}{n_p^{2/3}}, \qquad v_A = \frac{B}{(4\pi m_p n_p)^{1/2}}, \qquad T_{exp} = \left(\frac{v_p}{258}\right)^{3.113}$$

We tested the solar wind data from OMNI dataset against the 4-categorization algorithm during a year around solar maximum (2003) and a year around solar minimum (2008). The four groups of solar winds with the proton speed as an example are shown in figure(2). In the solar maximum year, we see the release of the ejecta from the Sun multiple times over the year, especially at the end of October and beginning of November where some unusual extreme storms were recorded [Balch *et al.* 2004, Love 2008]. In March 2008, which is considered as one of the deepest minimum recorded [Russell *et al.* 2010, Woods 2010, and Benevolenskaya and Kostuchenko 2013], the coronal-hole-origin solar wind type dominates the categorization. On the other hand, the observed speed of the coronal-hole-origin and streamer-belt-origin solar winds are in good agreement with the expected values. Moreover, the solar winds originating from sector-reversal-region are characterized by low speed (around 300 km/s) in years of both solar maximum and minimum.

3. Solar Wind Advection

In 1958, Parker proposed the spiral model for the solar wind interplanetary magnetic field (IMF) propagation into the heliosphere based on the radial outflow of parcels of plasma from the surface of the solar corona, as shown in figure(3-a). The arrival angle of the IMF at 1 AU, which is the angle between the orientation of the IMF and the radial direction, according to Parker spiral model should be approximately 45°. However, the probability distribution function (PDF) of the arrival angle at 1 AU, figure(3-b), elucidates the dependence of the arrival angle on the solar wind speed. The occurrence of the 45° arrival angle is found to be the most probable for solar wind speeds in the [350-450] km/s interval. However, there are always probabilities for other angles of arrival depending on the structural variation of the interplanetary magnetic field.
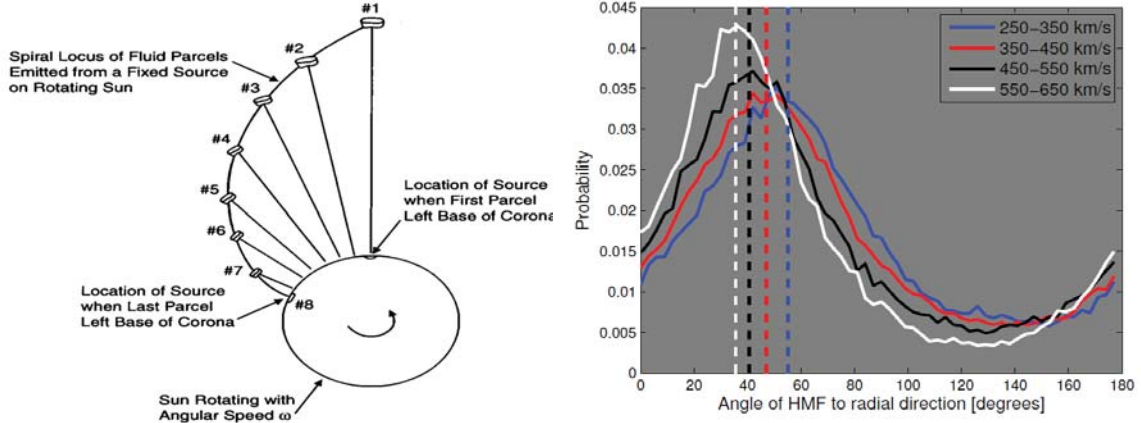
(a) Parker Spiral Model of the interplanetary magnetic field with the emission of magnetized plasma from the rotating sun. Adapted from Hundhausen [1995].

(b) Probability distribution function of the solar wind arrival angle at 1 AU as a function of its speed. Adapted from Owens and Forsyth [2013].

Figure 3: *(a) Parker spiral model for the advection of magnetized plasma parcels in the solar wind, and (b) the probability distribution function of the solar wind speed dependence on arrival angle at 1 AU.*

To test the advection or propagation model, it is preferable to have a distinct event that can be seen by the two monitoring stations so that we may consider the wind advection between them. A discontinuity in the IMF has been used by Horbury *et al.* [2001] to uniquely identify the same structure at two monitoring stations, where a discontinuity is defined as a sudden change in the orientation or magnitude of the interplanetary magnetic field.

Based on the Parker spiral model, and assuming that the parcel of magnetized plasma is advected with constant velocity along the Sun-Earth line, we can use the simple kinematics ($v_x = x/t$) to find the travel time of the solar wind plasma with the embedded magnetic field between two spacecraft. However, the advection of the solar wind as a flat surface ignores the variation in the phase front of the IMF which may be tilted at arbitrary angles with-respect-to the Sun-Earth line [Weimer *et al,* 2002, 2003, and 2008, Ridley 2000]. Also, it ignores the relative location between the spacecraft, and their locations with respect to the Sun-Earth line.

To include the orientation of the magnetic field phase front, we need to calculate the normal to the surface of minimum variations in the interplanetary magnetic field. Then we can estimate the propagation time between two points upstream using equation(2):

$$t_{adv} = \frac{(r_{s_2} - r_{s_2}) \cdot \hat{n}}{v_{sw} \cdot \hat{n}} \tag{2}$$

where, r_{s_1} and r_{s_2} are the locations of the two upstream monitoring stations, $\hat{n}$ is the normal to the IMF surface of minimum variations, and v_{sw} is the solar wind velocity.

Weimer *et al.* [2002, 2003] used minimum variance analysis of the magnetic field (MVAB) by constructing a covariance matrix from the IMF measurements, and then finding the eigenvector that corresponds to the smallest non-negative eigenvalue in order to estimate the orthogonal to the surface of minimum variations in the magnetic field. Another improvement to the MVAB method was made by Weimer *et al.* [2008] when they added a constraint in the magnitude of the magnetic field along the normal, and they called this
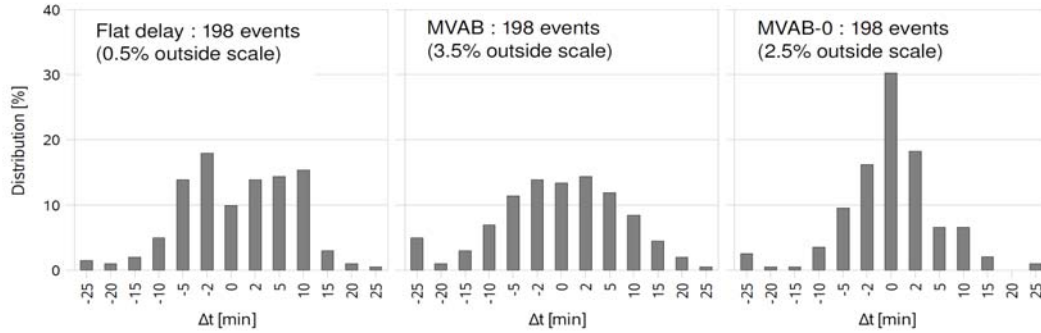
Figure 4: *A comparison of the error in the arrival time between different methods (flat delay, MVAB, and MVAB-0) for calculating the solar wind time delay [adapted from Mailyan et al. [17]]*

.

method MVAB-0. They considered all events they studied to be characterized as *tangential-discontinuity*, which makes the component of the magnetic field along the normal the surface of minimum variations vanish.

Mailyan *et al.* [2008] estimated the propagation time of the solar wind between ACE and Cluster for 198 events using the "Flat Delay", "MVAB", and "MVAB-0" methods. Then, they calculated the relative distribution of the timing errors from these methods using the difference between the estimated and observed arrival time, as shown in figure(4). They found that the error in the arrival time for "flat-delay" and "MVAB" for most of the events are within ±10 minutes, while more than two-third of the events arrived in the limit of ±5 minutes using "MVAB-0" method. Thus, a difference of only ±5 minutes was found between the best estimation method for the arrival time and the worst one. Because the solar wind variations are typically small on a 5 minute timescale, and we interpolated over data gaps slightly larger than this and used the "flat-delay" method (simple advection) in calculating the time shift.

4. Data Sources, Limitations, and Conditioning

To generate an ensemble for the solar wind parameters, such as velocity, density, and z-component of the IMF, we need to use the measurements from at least two monitoring stations or spacecraft in the heliosphere. The more upstream spacecraft is used as a reference for the solar wind measurements and the closest spacecraft is used as a target to generate the Kernel Density Estimation (KDE) function. The presence of the Advanced Composition Explorer (ACE) satellite in its halo orbit at the first Lagrangian point[1] (L_1) gives it an advantage over other solar wind mission satellites to be the reference point [Acuña *et al.* 1995 and Stone *et al.* 1998]. For the target monitoring station we found the Interplanetary Monitoring Platform-8 (IMP8) spacecraft spends most of its circular orbit around the Earth outside the magnetopause (i.e. it is immersed in the solar wind in the heliosphere before it starts its interaction with the nose of the magnetosphere at the bow shock) [Paularena and King 1999]. Also, having IMP8 very close to the magnetopause gives it an advantage over other solar wind missions because the ensemble that will be generated from its measurements will be very close to that at the magnetosphere nose.

Although choosing ACE and IMP8 to generate the ensemble is good regarding their locations and orbits,

_____

[1]At the Lagrangian points the gravitational forces on the spacecraft from the Earth and the Sun cancel out because they are equal to each other in magnitude but opposite in direction.
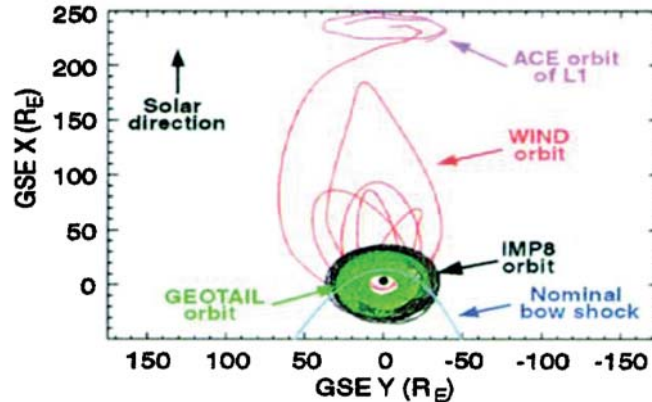
Figure 5: *Comparison of the location of ACE and IMP8 in the heliosphere to other spacecraft such as WIND and Geotail. ACE stays in its halo orbit at the first Lagrangian point and IMP8 orbits the Earth and stays outside the nominal bow shock location most of its orbital time. [Adapted after Haggerty et al. [12]]*

there are two main limitations in using this pair of spacecraft. The first limitation is that there are only three years (1998, 1999, 2000) of overlap between ACE and IMP8, which makes the concurrent measurements of the solar wind parameters from these spacecraft somewhat limited for deriving Kernel Density Estimation (KDE) functions. The second limitation is that the IMP8 solar wind data has many large gaps due to non-continuous telemetry as well orbits that are partially inside Earth's bow shock. Moreover, the different rates of recording the measured data in ACE and IMP8, and even between the measurements of the plasma parameters and magnetic field components in the same spacecraft is a factor that should be considered.

Because our current plan includes only the use of ACE and IMP8 spacecraft, the three years limita-tion has no solution which requires the use of measurements from other solar wind missions. On the other hand, to overcome the large gaps in data found in IMP8 measurements, we divided the three years of data into time-slots of four hours length [2]. Then, we employed a 15 minutes gap-length restriction in the contiguous data in both ACE and IMP8 in each time-slot. The gap-length restriction helps in minimizing the inaccuracy that might arise while using the linear interpolation method which is used to fill the gaps in measured data in both spacecraft. Finally, we tested that all the solar wind parameters we use in categorizing the solar wind and generating their ensembles are found in the corresponding time-slots in both spacecraft, and we filtered-out all the time-slots that do not pass this test.

5. Advected Solar Wind Parameters

To calculate the advection time we used $t = x/v_{sw,x}$, with a constant solar wind velocity over the interval $[t_1, t_2]$, where $t = t_2 - t_1$. This method does not consider the relative positions of ACE and IMP8 spacecraft in their orbits or the spatial variations of the interplanetary magnetic field components in the solar wind. These two factors will add some errors to our method, but as we mentioned earlier while discussing Mailyan *et al.* [2008] work, the total effect of these errors will not exceed 5-10 minutes. According to the scale-length of the variations in the solar wind parameters of interest, an error of 5-10 minutes in the arrival time is acceptable for the current phase of the work and will be considered for further improvements in future by using the MVAB method.

---

[2]The number of time-slots available to generate the solar wind ensembles of four hours length are found to be much more than those of six hours length.
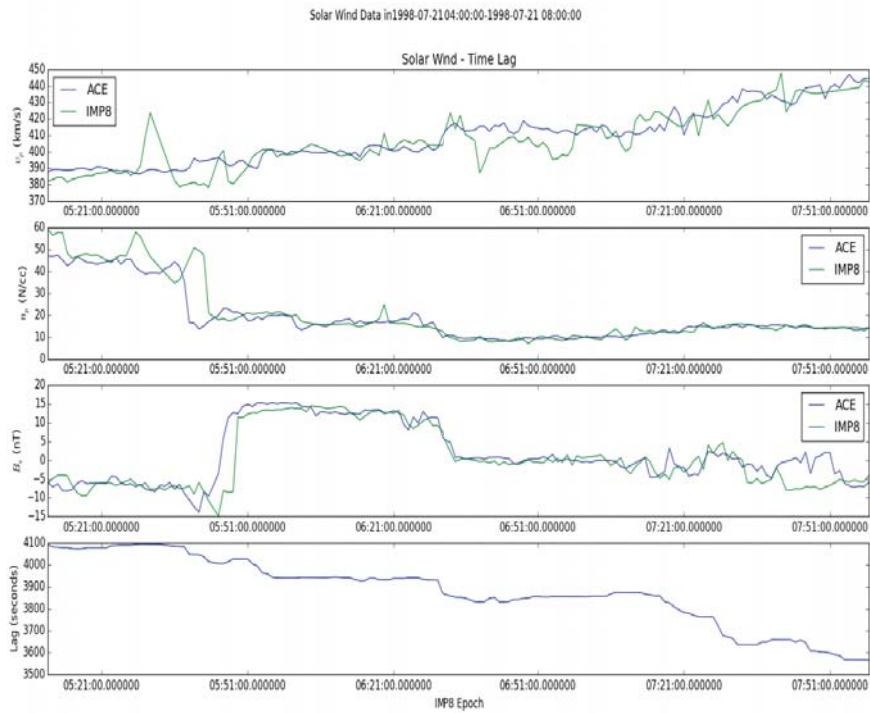
(a) Data measured on July 21, 1998.
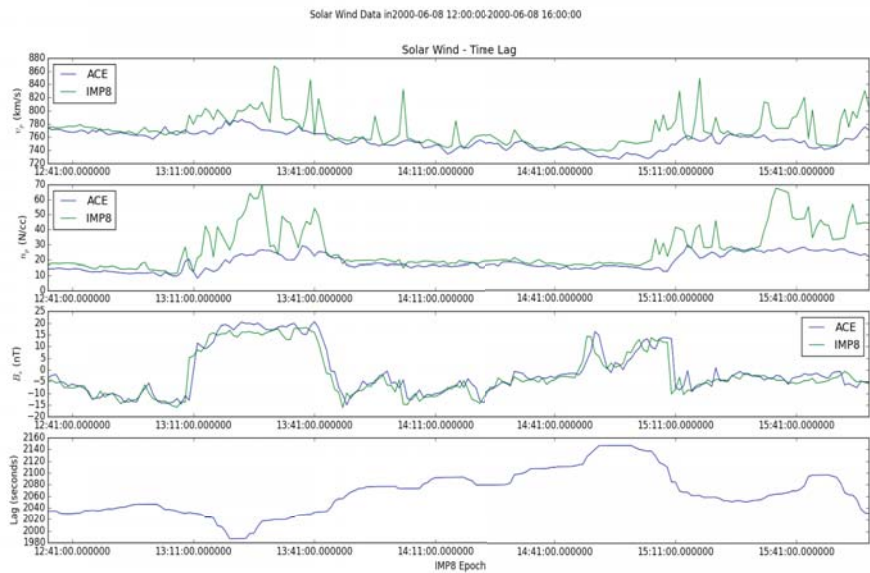
(b) Data measured on June 8, 2000.

Figure 6: *Two comparisons between the solar wind speed (first-panel), density (second-panel), and magnetic field (third-panel) measured at IMP8 spacecraft to those measured at ACE spacecraft and are the advected to IMP8 location. The calculated pointwise advection time (time-lag) is shown in the fourth-panel. The comparisons are made between these solar wind parameters that are measured in Summer 1998 (a) and Summer 2000 (b) that show different solar wind status.*

Our aim is to generate conditional probability distributions of solar wind parameters (P) just upstream, given a known value near L1, $p(P_{IMP}|P_{ACE})$. We therefore require that the measurements have a correspondence over the same time-scale. This requires all the measurements at the reference spacecraft (ACE) to be shifted in time to match the measurement time of the corresponding quantities at the target spacecraft (IMP8) in all the available time-slots. The required time-shifts can be estimated when calculating the advection time of solar wind parameters from ACE to IMP8 in these time-slots.

To find the advection time, there are two ways: (1) find the average advection time over the whole time slot using the average speed of $v_{sw,x}$, (2) find the advection time at each point measurement using the corresponding $v_{sw,x}$ at that point of time. We chose to use the second method to consider any variation in the solar wind parameters that might take place during the four hours time slot. To avoid any non-realistic variations or noise in the measurements that might give rise to a disturbance in the pointwise calculation of the advection time, we employed a 15-20 minute spatial median-filter[3] to smoothing the measured data.

In figure(6), we show a comparison between the measured solar wind parameters at ACE and IMP8, where ACE measurements are advected in time to be compared with a time-matched measurements at IMP8. Figures(6-a,b) present the solar wind speed, number density, interplanetary magnetic field, and pointwise lag-time between ACE and IMP8, respectively. The sharp transition in the magnitude and orientation of the interplanetary magnetic field (which can be described as a tangential discontinuity) is found in the two time-slots. The tangential discontinuity in the magnetic field helps as a feature that can be used in comparing or matching the measurements recorded in two distant monitoring stations.

In addition, although the measurements in subfigures(6-a,b) had been taken around the same time of Summer of 1998 and 2000, respectively, the solar wind parameters in subfigure(6-a) shows a low-speed and high-proton-density solar wind compared to the high-speed and low-proton-density solar wind in subfigure(6-b). So, the categorization scheme tells us that we have "streamer-belt-origin" and "coronal-hole-origin" solar winds in the respective presented intervals.

Comparing the trend and the fine details in the advected ACE measurements and the measured data in IMP8, we found that the IMF measurements match very nicely in both spacecraft datasets in 1998 and 2000. However, the IMP8 measurements for the solar wind speed and proton density in Summer of 2000 show many spikes all over the time-slot but they have a similar trend to the ACE advected measurements. Thus, we can rely on the flat-delay advection method for generating the ensemble for the solar wind measured parameters on IMP8.

6. Solar Wind Ensemble

To generate the solar wind ensemble ($p(V_{IMP}|V_{ACE})$) for the measurements of the solar wind speed at IMP8 based on the advected measurements of the speed at ACE, we grouped solar wind speed measurements into 25 km/s wide bins, and for every measured speed at the ACE spacecraft found to fall into that bin we recorded the concurrent speed at IMP8 in a corresponding interval. We therefore have approximated our conditional probability distributions by using data within the neighborhood of the exact value, i.e.
$p(V_{IMP}|V \in N (V_{ACE})$. Then we used all the intervals of IMP8 recorded solar wind speed to establish a Kernel Density Estimation (KDE) function for each interval. Basically, we establish a *conditional probability distribution (CPD)* for IMP8 solar wind measurements based on the corresponding recorded data advected from the ACE spacecraft. We in turn used this CPD to establish the KDE functions for IMP8 solar wind parameters [Sheskin 2003 and Wilks 2011].

---

[3]We chose the median-filter because of its superiority over the mean-filter in preserving all the useful details in the dataset.
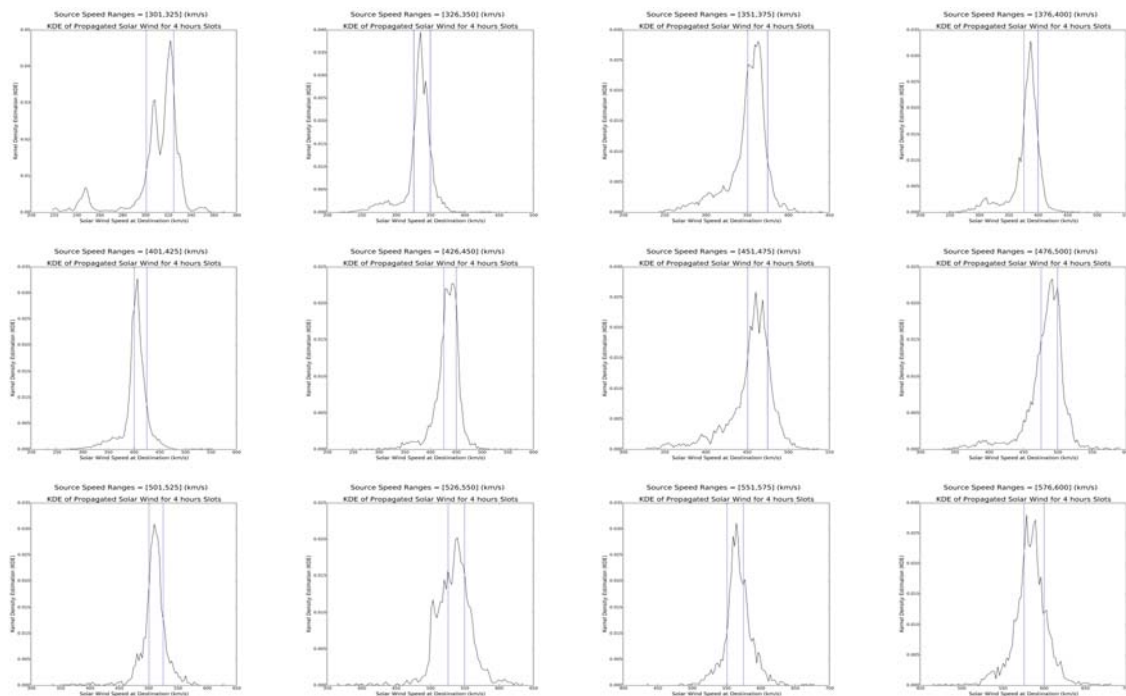
Figure 7: *Uncategorized Kernel Density Estimation (KDE) functions of solar wind wind that are measured at IMP8 spacecraft based on three years of advected measurements from ACE spacecraft to the IMP8 location using the flat-delay method. The vertical blue lines represent the interval of solar wind speeds measured at ACE.*

The Kernel Density Estimation (KDE) does not use a specific parametric variable to estimate the pa-rameters of a probability density. Instead, the KDE produces a smooth continuous density curve with bandwidth adapted to the sample data and its shape related to the Probability Density Function (PDF) generator. Although the histogram is similar to the KDE in building a function to represent the probability distribution, it distributes the sample data into discrete bins in such a way that can not be used to generate random numbers from the density distribution which requires a continuous probability density function. Because we need to draw random samples from the PDF functions, we prefer sampling the KDE (a continu-ous function) to simply resampling the measured data.
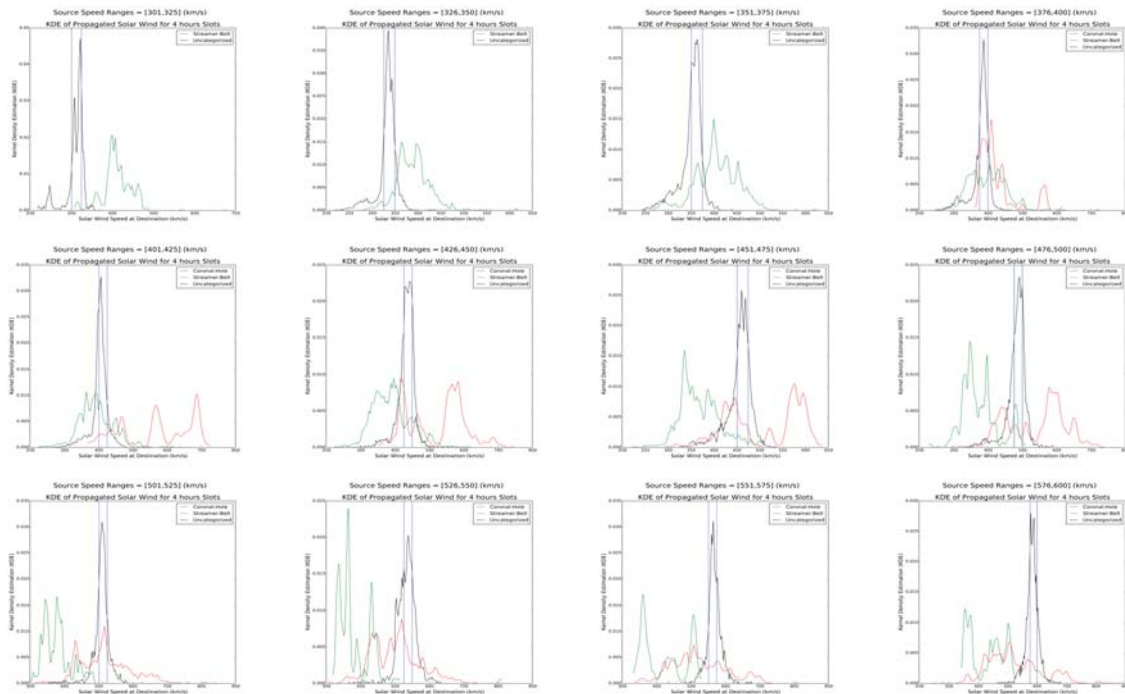
Figure(7) shows the KDE functions (solid black line) of the solar wind speed at IMP8 based on three years measurements. The two vertical lines represent the limits of the interval of solar wind speed at ACE. We found that in some cases about 65% of the solar wind speeds that are measured at IMP8 fall inside this interval. The lack of sufficient qualified measurements over the three years of overlap between ACE and IMP8 influenced the power of the established KDE functions. especially for the less frequently sampled solar wind speeds over that specific period of time in the solar cycle. This becomes more clear when we discuss the categorized KDE functions for different solar wind origins. Based on the 4-class categorization algorithm [Xu and Borovosky 2015], we used the solar wind measured speeds at ACE to establish KDEs for the "coronal-hole-origin" and "streamer-belt-origin" categories of the solar wind. Figure(8) shows the KDEs of the speed in the uncategorized solar wind (black solid line) and the categorized solar winds, coronal-hole-origin in red solid line and streamer-belt-origin in green solid line. The subplots in figure(8) shows the tendency of the uncategorized KDE of the solar wind speed toward the KDE of solar wind speed in the streamer-belt-origin category in the interval of slow solar winds, and this tendency shifts with the solar wind speed to be completely toward the KDE of solar wind speed in the coronal-hole-origin category.

Figure 8: *Categorized Kernel Density Estimation (KDE) functions (streamer-belt-origin in green and coronal-hole-origin in red) of solar wind speed at IMP8 spacecraft based on three years of advected measurements from ACE spacecraft, compared to the uncategorized KDE functions (solid black line). The vertical blue lines represent the corresponding interval of solar wind speed at ACE.*

Definitely, we can employ the KDE functions to generate an ensemble of the solar wind speed at IMP8 location in the upstream using one-point measurement at ACE. The ensemble of solar wind data can be generated by any number of random samples using the KDE functions for each measurement at ACE spacecraft. Then we can calculate any statistical quantity from these random samples depending on the calculations we want to use for. In figure(9) we used the established KDE functions to generate an ensemble of the solar wind speed to use it to calculate the range of speeds that is expected to be measured at IMP8 based on the measurement at ACE spacecraft. The interval of time we calculated the expected range of solar wind speed at IMP8 is Jan-Mar 2003 which is different from the interval we used to establish those KDE functions. This ensemble can be used to forecast the status of the solar wind right before it interacts with the bow-shock, which helps in forecasting the status of the magnetosphere and ionosphere about one hour in advance. Also, using the categorized KDE functions helps in forecasting the probability of the incoming solar wind to be fast or slow solar wind according to the historical events we studied. The three years of solar wind data availability limited our ability to establish better KDE functions for the categorized and uncategorized solar wind speed. This can be seen in the large bins which will give rise to random ensemble values that might lead to faster rate of variability in the solar wind parameters than observed. Because of the previous points "surrogate" time series of the solar wind should not be expected to preserve all properties of the solar wind, but should primarily be regarded as a first estimate of the uncertainty in the estimate of solar wind parameters impacting the magnetosphere. The results we showed for the categorized and uncategorized KDE functions give us a good sign for the applicability of this method to predict the solar wind status under certain limitations.
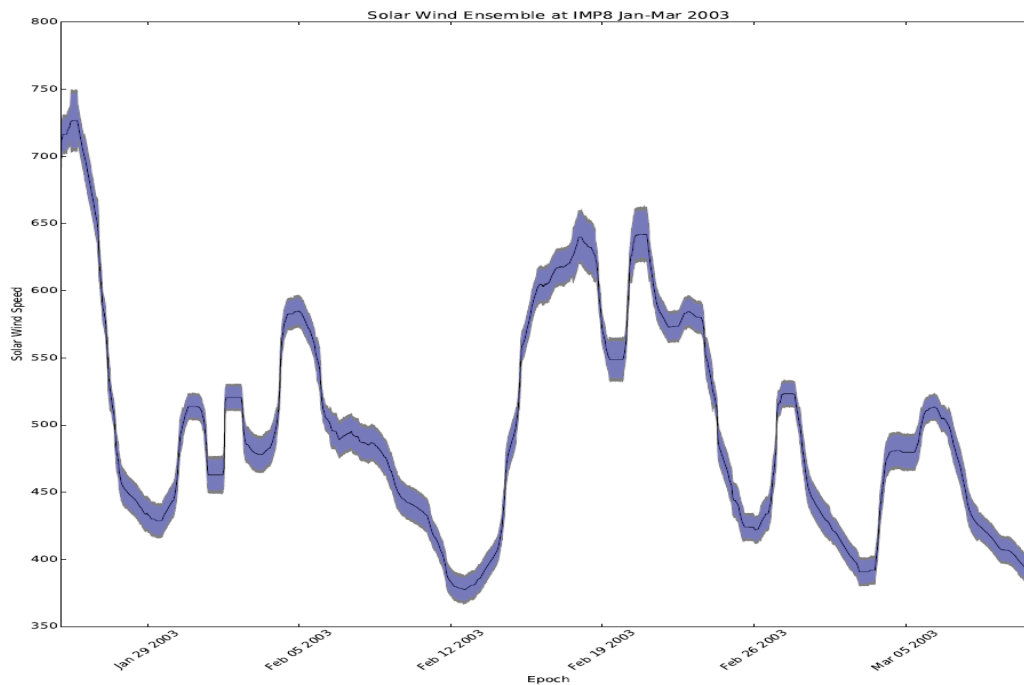
Figure 9: *An ensemble of solar wind speed at IMP8 location based on one-point of measurements at ACE spacecraft on Jan-Mar 2003 by using the KDE functions generated for the solar wind data in 1998 - 2000.*

7. Summary and Conclusions

We introduced the new 4-categorization scheme proposed by Xu and Borovoski [2015] for the type of the solar wind. Then we employed categorization empirical algorithm on solar wind data from OMNI dataset during solar maximum and solar minimum conditions to get the sense of the model applicability. Also, we employed that categorization algorithm on the measured solar wind data at both ACE and IMP8 to check the matching between findings in both missions which we expected should be the same in a four-hours time slot.

After we studied the comparison made by Mailyan *et al.* [2008] between different advection techniques (flat-delay, MVAB, and MVAB-0), we decided to accept the 5-10 minutes error and use the flat-delay method in the current phase of the work. We presented a comparison between the measured solar wind parameters, such as solar wind speed, proton density, and interplanetary magnetic field (IMF), at IMP8 with the advected solar wind measurements from ACE to IMP8 location. The comparison has been made for many time slots over three years, but we only presented the comparison between the summer of 1998 and 2000 to show the applicability of the technique under two different solar wind conditions. The comparison between the recorded solar wind measurements at IMP8 and the advected ones from ACE show a good agreement both in the overall trend and the fine details, especially when there is a sharp transition in the vertical component of the interplanetary magnetic field.

After checking the robustness of our advection model, we used the measured data at ACE and IMP8 to establish a Kernel Density Estimates of the conditional probability of solar wind speed at IMP8, given a certain speed at ACE. For this work we used bins of 25 km/s. The conditional probability distributions show a good fit inside the corresponding intervals of solar wind speed that measured at ACE and advected to IMP8. In some cases we found 65% of the IMP8 measurements fall inside the 25 km/s interval of solar

wind speed at ACE while the other cases have their measurements fall outside those intervals. The likely explanation for this is simply that IMP8 is sampling different solar wind plasma to ACE; the solar wind sampled by ACE may not have interacted with the magnetosphere. Some of the differences may be due to errors introduced by the simple advection scheme.

A comparison between the KDE functions of the uncategorized and categorized solar winds was made and showed a tendency of the uncategorized solar wind toward the expected category based on the solar wind speed. The KDE functions can be used to generate an ensemble of solar wind data which helps in forecasting the nature of interaction between the solar wind and the bow-shock and the status of the magnetosphere and ionosphere about two hours in advance. However, to acquire KDE functions that generate reliable ensembles of the solar wind data we need to have more measurements which can be achieved by including more missions in the upstream.

8.   Future Work

We believe that the error introduced by the flat-delay method is questionable based on the solar wind category. So, we are going to test the variations in the lag-time with solar wind categories. We are also plan to test the effect of different orientation of the solar wind surface on the accuracy of the advection technique we used and compare the results with MVAB-0 method that proposed by Weimer *et al.* [2008]. These tests will give us more information about the range of applicability, limitations, and caveats in different propagation model.

The work we have done using the Kernel Density Estimation (KDE) functions will be extended in two ways. First we will include the calculation of the KDE functions for more solar wind parameters such as the proton-density and interplanetary magnetic field components in addition to the solar wind speed. The establishment of the KDE functions for these three parameters will allow us to use the Burton's empirical equation [Burton *et al.* 1975] to estimate the Dst magnetic index and compare it to the measurements at the ground stations. This will show the confidence level of using this method as a reliable tool for forecasting. Next we will include the solar wind measurements from more missions such as Clusters and Wind to be able to cover longer time period, which will result in establishing better KDE functions.

Finally, some of the width of the conditional probability distributions may be due to the width of the bins used when constructing the KDEs. A possible solution that will minimize this extra source of uncertainty is to instead calculate conditional probability distributions of the error term; that is, instead of estimating $p(P_{IMP}|P \in N(P_{ACE}))$, we will estimate $p(P_{ACE} - P_{IMP}|P_{ACE})$.

References

[1] MH Acuña, KW Ogilvie, DN Baker, SA Curtis, DH Fairfield, and WH Mish. The global geospace science program and its investigations. *Space Science Reviews*, 71(1-4):5–21, 1995.

[2] Daniel N Baker. The occurrence of operational anomalies in spacecraft and their relationship to space weather. *Plasma Science, IEEE Transactions on*, 28(6):2007–2016, 2000.

[3] C Balch, B Murtagh, D Zezula, L Combs, G Nelson, K Tegnell, M Crown, and B McGehan. Service assessment: Intense space weather storms october 19–november 07, 2003. *NOAA Silver Spring, Md*, 2004.

[4] EE Benevolenskaya and IG Kostuchenko. The total solar irradiance, uv emission and magnetic flux during the last solar cycle minimum. *Journal of Astrophysics*, 2013, 2013.

[5] RK Burton, RL McPherron, and CT Russell. An empirical relationship between interplanetary conditions and dst. *Journal of geophysical research*, 80(31):4204–4214, 1975.

[6] Richard C Carrington. Description of a singular appearance seen in the sun on september 1, 1859. *Monthly Notices of the Royal Astronomical Society*, 20:13–15, 1859.

[7] Anthea Coster, John Foster, and Philip Erickson. Innovation-monitoring the ionosphere with gps-space weather-large gradients in the ionospheric and plasmapheric total electron content affects gps observations and measurements. gps data. *GPS World*, 14(5):42–49, 2003.

[8] James W Dungey. Interplanetary magnetic field and the auroral zones. *Physical Review Letters*, 6(2):47, 1961.

[9] CJ Farrugia, FT Gratton, VK Jordanova, H Matsui, S Mühlbachler, RB Torbert, KW Ogilvie, and HJ Singer. Tenuous solar winds: Insights on solar wind–magnetosphere interactions. *Journal of Atmospheric and Solar-Terrestrial Physics*, 70(2):371–376, 2008.

[10] HU Frey, TD Phan, SA Fuselier, and SB Mende. Continuous magnetic reconnection at earth's magnetopause. *Nature*, 426(6966):533–537, 2003.

[11] SA Fuselier, KJ Trattner, and SM Petrinec. Antiparallel and component reconnection at the dayside magnetopause. *Journal of Geophysical Research: Space Physics (1978–2012)*, 116(A10), 2011.

[12] DK Haggerty, EC Roelof, CW Smith, NF Ness, RL Tokar, and RM Skoug. Interplanetary magnetic field connection to the l1 lagrangian orbit during upstream energetic ion events. *Journal of Geophysical Research: Space Physics (1978–2012)*, 105(A11):25123–25131, 2000.

[13] TS Horbury, D Burgess, M Fränz, and CJ Owen. Prediction of earth arrival times of interplanetary southward magnetic field turnings. *Journal of Geophysical Research: Space Physics (1978–2012)*, 106(A12):30001–30009, 2001.

[14] Michael C Kelley, Jonathan J Makela, Jorge L Chau, and Michael J Nicolls. Penetration of the solar wind electric field into the magnetosphere/ionosphere system. *Geophysical Research Letters*, 30(4), 2003.

[15] Margaret G Kivelson and Christopher T Russell. *Introduction to space physics*. Cambridge university press, 1995.

[16] Jeffrey J Love. Magnetic monitoring of earth and space. *Physics Today*, 61(2):31, 2008.

[17] B Mailyan, C Munteanu, and S Haaland. What is the best method to calculate the solar wind propagation delay? In *Annales Geophysicae*, volume 26, pages 2383–2394. Copernicus GmbH, 2008.

[18] Robert L McPherron, James M Weygand, and Tung-Shin Hsu. Response of the earth's magnetosphere to changes in the solar wind. *Journal of Atmospheric and Solar-Terrestrial Physics*, 70(2):303–315, 2008.

[19] SE Milan, G Provan, and Benoît Hubert. Magnetic flux transport in the dungey cycle: A survey of dayside and nightside reconnection rates. *Journal of Geophysical Research: Space Physics (1978–2012)*, 112(A1), 2007.

[20] Keith W Ogilvie, A Durney, and TT von Rosenvinge. Description of experimental investigations and instruments for the isee spacecraft. *IEEE Transactions on Geoscience Electronics*, 16:151–153, 1978.

[21] Shinichi Ohtani, Teiji Uozumi, Hideaki Kawano, Akimasa Yoshikawa, Hisashi Utada, Tsutomu Nagatsuma, and Kiyohumi Yumoto. The response of the dayside equatorial electrojet to step-like changes of imf bz. *Journal of Geophysical Research: Space Physics*, 118(6):3637–3646, 2013.

[22] Matt J Owens and Robert J Forsyth. The heliospheric magnetic field. *Living Reviews in Solar Physics*, 10(5), 2013.

[23] Eugene N Parker. Dynamics of the interplanetary gas and magnetic fields. *The Astrophysical Journal*, 128:664, 1958.

[24] KI Paularena and JH King. NasaấŹs imp 8 spacecraft. In *Interball in the ISTP Program*, pages 145–154. Springer, 1999.

[25] TI Pulkkinen, M Palmroth, EI Tanskanen, N Yu Ganushkina, MA Shukhtina, and NP Dmitrieva. Solar windấmagnetosphere coupling: a review of recent results. *Journal of Atmospheric and Solar-Terrestrial Physics*, 69(3):256–264, 2007.

[26] IG Richardson, EW Cliver, and HV Cane. Sources of geomagnetic activity over the solar cycle: Relative importance of coronal mass ejections, high-speed streams, and slow solar wind. *JOURNAL OF GEOPHYSICAL RESEARCH-ALL SERIES-*, 105(A8):18–203, 2000.

[27] IG Richardson, EW Cliver, and HV Cane. Sources of geomagnetic storms for solar minimum and maximum conditions during 1972–2000. *Geophys. Res. Lett*, 28(13):2569–2572, 2001.

[28] AJ Ridley. Estimations of the uncertainty in timing the relationship between magnetospheric and solar wind processes. *Journal of Atmospheric and Solar-Terrestrial Physics*, 62(9):757–771, 2000.

[29] CT Russell. Solar wind and interplanetary magnetic field: A tutorial. *Space Weather*, pages 73–89, 2001.

[30] CT Russell, JG Luhmann, and LK Jian. How unprecedented a solar minimum? *Reviews of Geophysics*, 48(2), 2010.

[31] R Schwenn. Solar wind sources and their variations over the solar cycle. In *Solar Dynamics and Its Effects on the Heliosphere and Earth*, pages 51–76. Springer, 2007.

[32] EC Stone, AM Frandsen, RA Mewaldt, ER Christian, D Margolies, JF Ormes, and F Snow. The advanced composition explorer. In *The Advanced Composition Explorer Mission*, pages 1–22. Springer, 1998.

[33] Daniel R Weimer and Joseph H King. Improved calculations of interplanetary magnetic field phase front angles and propagation time delays. *Journal of Geophysical Research: Space Physics (1978–2012)*, 113(A1), 2008.

[34] DR Weimer, DM Ober, NC Maynard, WJ Burke, MR Collier, DJ McComas, NF Ness, and CW Smith. Variable time delays in the propagation of the interplanetary magnetic field. *Journal of Geophysical Research: Space Physics (1978–2012)*, 107(A8):SMP–29, 2002.

[35] DR Weimer, DM Ober, NC Maynard, MR Collier, DJ McComas, NF Ness, CW Smith, and J Watermann. Predicting interplanetary magnetic field (imf) propagation delay times using the minimum variance technique. *Journal of Geophysical Research: Space Physics (1978–2012)*, 108(A1), 2003.

[36] DT Welling. The long-term effects of space weather on satellite operations. In *Annales Geophysicae*, volume 28, pages 1361–1367. Copernicus GmbH, 2010.

[37] Daniel S Wilks. *Statistical methods in the atmospheric sciences*, volume 100. Academic press, 2011.

[38] Thomas N Woods. Irradiance variations during this solar cycle minimum. *arXiv preprint arXiv:1003.4524*, 2010.

[39] Fei Xu and Joseph E Borovsky. A new four-plasma categorization scheme for the solar wind. *Journal of Geophysical Research: Space Physics*, 120(1):70–100, 2015.

[40] L Zhao, TH Zurbuchen, and LA Fisk. Global distribution of the solar wind during solar cycle 23: Ace observations. *Geophysical Research Letters*, 36(14), 2009.

Observations and Models of Substorm Injection Dispersion Patterns

Nadine M. E. Kalmoni

Mullard Space Science Laboratory, University College London, Dorking, RH5 6NT, UK

Michael G. Henderson

Los Alamos National Laboratory, New Mexico, US

Abstract

We present observations and models of a dispersionless substorm injection observed by Van Allen Probe A as it was approaching apogee on 23 June 2013 at 05:24 UT. The injection was also observed from multiple geostationary Los Alamos National Laboratory satellites. We compare enhancements in differential energy flux observed by multiple spacecraft with dispersion signatures predicted by the Injection Boundary Model. By tracing particles backward in time in steady state conditions we show whether or not a flux enhancement due to an injection is expected and if so, what MLT location the particle originates from. This allows us localise the injection region radially as well as in MLT.

Keywords: substorm injections, dispersionless, dispersed, injection boundary model, Van Allen Probes, LANL

1. Introduction to Particle Motion in the Inner Magnetosphere

1.1. Single particle motion and particle drifts

Charged particles under the influence of electric and magnetic fields feel both the Coulomb force (due to the electric field) and Lorentz force (due to the magnetic field). This gives the equation of motion for a charged particle with charge q:

$$m\frac{d\mathbf{v}}{dt} = q(\mathbf{E} + \mathbf{v} \times \mathbf{B}) \tag{1}$$

Gyro Motion

The Lorentz force acts perpendicular to the particle velocity, causing it to gyrate around a magnetic field line. If the particle has a velocity component parallel to the magnetic field, then the particle will gyrate along the field line in a helical trajectory. This allows us to define the particle pitch angle, α:

$$\alpha = tan^{-1}\left(\frac{v_\perp}{v_\parallel}\right) \tag{2}$$

where $v_\perp$ and $v_\parallel$ are the velocity components perpendicular and parallel to the magnetic field direction respectively. The magnetic moment of a particle is given by the ratio between perpendicular energy and magnetic field strength. It is also known as the first adiabatic invariant and is conserved over timescales longer than the particle gyro period.

$$\mu = \frac{W_\perp}{B} = \frac{mv_\perp^2}{2B} = \frac{mv^2 sin^2\alpha}{2B} \tag{3}$$

Email addresses: `nadine.kalmoni.13@ucl.ac.uk` (Nadine M. E. Kalmoni), `mghenderson@lanl.gov` (Michael G. Henderson)

Bounce Motion

If there is an increasing magnetic field strength along the field line, the parallel particle velocity component decreases as the particle moves into a higher field strength. This corresponds to an increasing pitch angle. However as no work is done on the particle the energy is conserved. This means that $W_\perp$ increases and $W_\parallel$ decreases. As μ is conserved:

$$\mu_1 = \mu_2 = \frac{mv^2 sin^2\alpha_1}{2B_1} = \frac{mv^2 sin^2\alpha_2}{2B_2} \tag{4}$$

$$\frac{sin^2\alpha_2}{sin^2\alpha_1} = \frac{B_2}{B_1} \tag{5}$$

When the pitch angle becomes $\alpha = 90°$ the particle has no parallel energy and is reflected at its mirror point, B_m. The magnetic mirroring of particles as they gyrate along the dipolar field lines in the Earth's inner magnetosphere is the cause of bounce motion.

Drift motion

If an electric field is present this introduces an additional particle drift across magnetic field lines. This is also known as $\mathbf{E} \times \mathbf{B}$ drift and is perpendicular to both the electric and magnetic field and acts in the same direction for both ions and electrons.

$$v_E = \frac{\mathbf{E} \times \mathbf{B}}{B^2}$$

There are also particle drifts associated with a magnetic gradient or curvature of magnetic field lines.
A magnetic gradient leads to a drift perpendicular to both the magnetic field and its gradient.

$$v_\nabla = \frac{v_\perp^2}{2qB^3}(\mathbf{B} \times \nabla B)$$

The curvature of magnetic field lines causes a drift perpendicular to the radius of curvature and magnetic field.

$$v_R = \frac{mv_\parallel^2}{q} \frac{\mathbf{R_c} \times \mathbf{B}}{R_c^2 B^2}$$

Equatorially mirroring particles do not feel the curvature drift as they do not have a velocity component parallel to the magnetic field. Both the gradient and curvature drifts cause electrons to drift eastward and ions to drift westward. This results in the ring current.

1.2. Adiabatic Invariants

The adiabatic invariants are treated as characteristic constants of particles, however they can change over long time scales. Each of the particle motions outlined above has an adiabatic invariant associated with it:

- The first adiabatic invariant:
  The magnetic moment, μ, is associated with gyration about the magnetic field.

- The second adiabatic invariant:
  The longitudinal invariant, J, is associated with the motion along the magnetic field.

- The third adiabatic invariant:
  Φ is associated with the drift motion perpendicular to the magnetic field.
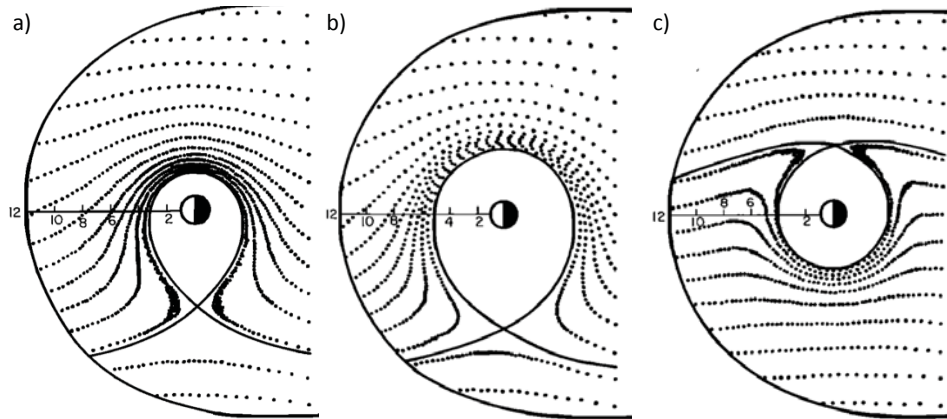
Figure 1: Particle drift paths for *a)* $\gamma\mu = 0$. Low energy particles of both species are dominated by electric field drifts. They have the stagnation point at dusk. *b)* electrons with $\gamma\mu = 0.05keV/\gamma$. *c)* protons with $\gamma\mu = 0.05keV/\gamma$. (where $\gamma = 1 \times 10^{-9}$ T) (Kavanagh et al., 1968).

1.3. Drift Paths & Alfvén layers

We have seen how electric and magnetic fields affect the particle trajectories. The magnetic field drifts are stronger closer to Earth as the total magnetic field strength is higher. There are two different electric fields which also affect particle motion due to $\mathbf{E} \times \mathbf{B}$ drift. This drift is not charge dependent and acts in the same direction for both ions and electrons.

- Convection Electric Field
  This dawn-dusk electric field is observed from the fixed frame of reference from the Earth due to solar wind draping around the magnetosphere. The electric field is enhanced during a southward interplanetary magnetic field (IMF) when the magnetosphere is in an 'open' configuration. The convection electric field dominates in the tail, causing Earthward flow of plasma due to $\mathbf{E} \times \mathbf{B}$ drift.

- Corotation Electric Field
  The corotation electric field is due to the rotation of the Earth and associated magnetic field lines which drag the plasma with it due to the frozen- in condition. This is equivalent to an inward pointing electric field which dominates over the convection electric field in the inner magnetosphere.

Taking into account all the electric and magnetic field drifts we can calculate the particle trajectories. These are the same for zero energy particles of both species as the electric field drifts are not charge dependent. However for non-zero energies the magnetic field drifts which are both energy and charge dependent cause differences between electron and proton drift paths.

The overall particle drift is given by the following equation:

$$v_d = v_{Ecor} + v_{Econv} + v_\nabla + v_R$$

This results in species and energy dependent particle trajectories. Particles which are far enough away from Earth whose trajectories are dominated by the convection electric field are on open drift paths. Particles closer to Earth are dominated by the corotation electric field and lie on closed drift paths. The boundary between the two region is called the Alfvén layer. Drift paths for different energy particles are shown in Figure 1. Figure 1*a* shows drift paths for low energy electrons and protons. The Alfvén layer stagnation point is located at dusk as this is whether the corotation and convection drifts act in opposite directions and cancel out. Any particles inside the Alfvén layer are stuck on closed drift paths. For higher energy electrons the Alfvén layer moves outwards. Higher energy protons have a stagnation point on the dawn side as magnetic drifts act in the opposite direction to corotation.
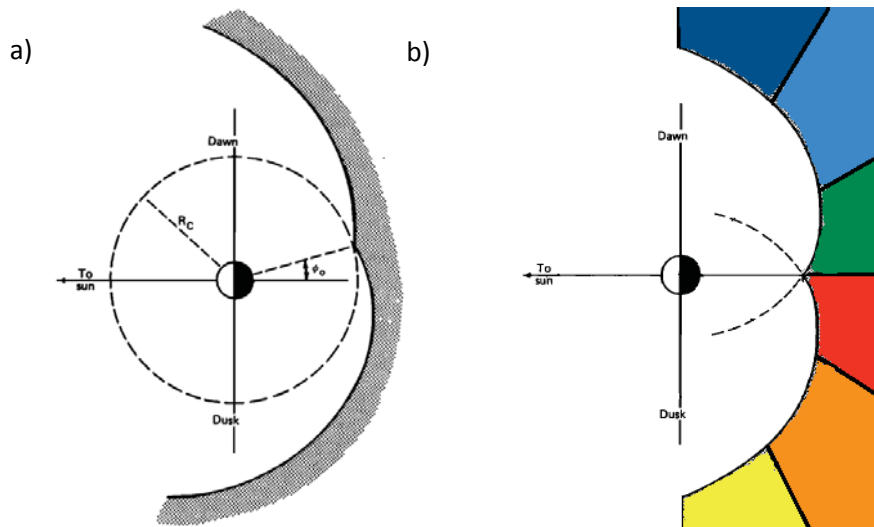
Figure 2: *a)* Proposed double spiral injection boundary behind which all particles are energised at the time of injection (Mauk and Meng, 1983). *b)* Injection boundary with colour coded MLT sections. The colours indicated are used to show the location of particle origin. If the initial particle position in local time is: 18:00-20:00 yellow, 20:00-22:00 orange, 22:00-00:00 red, 00:00-02:00 green, 02:00- 04:00 light blue, 04:00-06:00 dark blue (adapted from Mauk and Meng (1983)).

2. Introduction to Substorm Injections

Magnetospheric substorms are associated with multiple global and local signatures observed from the ground and space. One signature of the substorm expansion phase is a sudden increase in particle fluxes over a wide energy range observed from the nightside magnetosphere, usually from geosynchronous orbit (Konradi, 1967; Lanzerotti et al., 1971; Belian et al., 1981). This is known as a substorm injection.

Substorm injections can be observed when the particles fluxes for multiple energy channels increase at the same time i.e. dispersionless injections. If a satellite is in the injection region then the substorm injection will be dispersionless. However if the satellite is not in the injection region the particle fluxes will increase at different times. This can be explained by particle drifts. Faster moving particles (higher energy) will arrive at the satellite earlier than low energy particles. Arrival time also depends on the particle species and the location of the satellite in relation to the injection region. Drift echoes can also be observed after injections if particles of certain energies lie on closed drift paths at the satellite location.

The injection boundary model, is a phenomenological model used to predict the injection dispersion signatures observed by satellites at geosynchronous orbit (McIlwain, 1974; Mauk and Meng, 1983). The model describes a stationary boundary with the shape of a double spiral behind which protons and electrons of all energies are energised at the same time. The boundary is shown in Figure 2*a*. If a satellite is located behind this boundary at the time of injection a dispersionless injection is observed. A satellite which is not in the injection region will observed a dispersed signature due to the different drift times and paths the energised particles follow after the injection.

In this study we investigate whether the injection boundary model and 90° pitch angle particle drifts due to a Volland-Stern electric field and dipole magnetic field can explain substorm injection patterns observed by a satellite in an eliptical orbit, e.g. Van Allen Probes. We investigate how the shape and orientation of the boundary affects dispersion patterns and whether using multi-spacecraft measurements at geostationary orbit and the Van Allen Probes allows us to localise the injection region in local time.

3. Instrumentation

3.1. Los Alamos National Laboratory Geostationary Satellites

The Los Alamos National Laboratory (LANL) satellites are in a geostationary orbit.
The Magnetospheric Plasma Analyzer (MPA) consists of a single electrostatic analyser coupled to an array of channel electro multipliers. It measures ion and electron energies in the range $\sim$ 1 eV/q to greater than 40 keV/q (Bame et al., 1993).
The Synchronous Orbit Particle Analyzer (SOPA) consists of 3 solid state detector telescopes pointing at 30°, 90° and 120° to the satellite's spin axis. Differential fluxes of protons can be measured with energies from 50 keV to 50 MeV and electrons from 50 keV to 1.5 MeV (Belian et al., 1992).

3.2. Van Allen Probes

For this study we also use data from the Van Allen Probes Energetic Particle, Composition, and Thermal Plasma Suite (ECT) . The Van Allen Probes mission consist of two probes, A and B, in elliptical orbits to study the radiation belts with an apogee of 5.8 R_E and orbital period of $\sim$ 9 hours.
The instruments used for this study are:

- Helium Oxygen Proton Electrion (HOPE) is an electrostatic top-hat analyser which measures electrons and ions from below 20 eV (or spacecraft potential) to greater than 45 keV.

- Magnetic Electron Ion Spectrometer (MagEIS) measures electrons from 30 keV to 4 MeV and ions from 20 keV to 1MeV.

- Relativistic Electron Proton Telelscope (REPT) measures electrons from 4-10 MeV and protons from 20-75 MeV.

4. Observations

We present observations of a dispersionless substorm injection as observed at 05:24 UT by Van Allen Probe A in Figure 3 on 23 June 2013. The top panel shows differential electron flux from the HOPE, MagEIS and REPT instruments with increasing particle energy upwards on the y-axis. The second panel is the HOPE differential proton flux with increasing particle energy downwards. This is so that the zero energy electrons and protons which follow the same drift paths share a common axis. The third panel shows the MagEIS and REPT differential proton flux with increasing particle energy downwards on the y-axis. In this plot the background flux has been removed in order to show flux enhancements. Electrons and protons are energised up to 2 MeV in both species. Clear drift echoes are then observed in the proton observations. This injection is shortly followed by a second injection at $\sim$ 06:00 UT. The locations of the Van Allen Probes and geostationary LANL satellites at the time of the first injection are shown in Figure 4.

5. Models of Substorm Injections based on the Injection Boundary Model

In order to investigate whether the injection boundary model can be used to explain the injection dispersion pattern at multiple satellite locations, we trace protons and electrons with energies of 0 - 500 keV. This is done from the satellite location at a time after the injection tracing backward to the injection time to find the particle position of origin. If the location of the particle at the time of injection is on or tail ward of the injection boundary then it is possible that the particle was energised due in the substorm injection. The particle tracing was done by numerically solving the equation of motion (backwards in time) for equatorially mirroring particles in the guiding centre approximation as given in Buzulukova et al. (2002):

$$\frac{dr}{dt} = \frac{1}{B \cdot r} \cdot \left[\mu \cdot \frac{\partial B}{\partial \phi} \Big|_r + \frac{\partial \Phi}{\partial \phi} \Big|_r \right] \qquad (6)$$

$$\frac{d\phi}{dt} = -\frac{1}{B \cdot r} \cdot \left[\mu \cdot \frac{\partial B}{\partial r} \Big|_\phi + \frac{\partial \Phi}{\partial r} \Big|_r \right] \qquad (7)$$

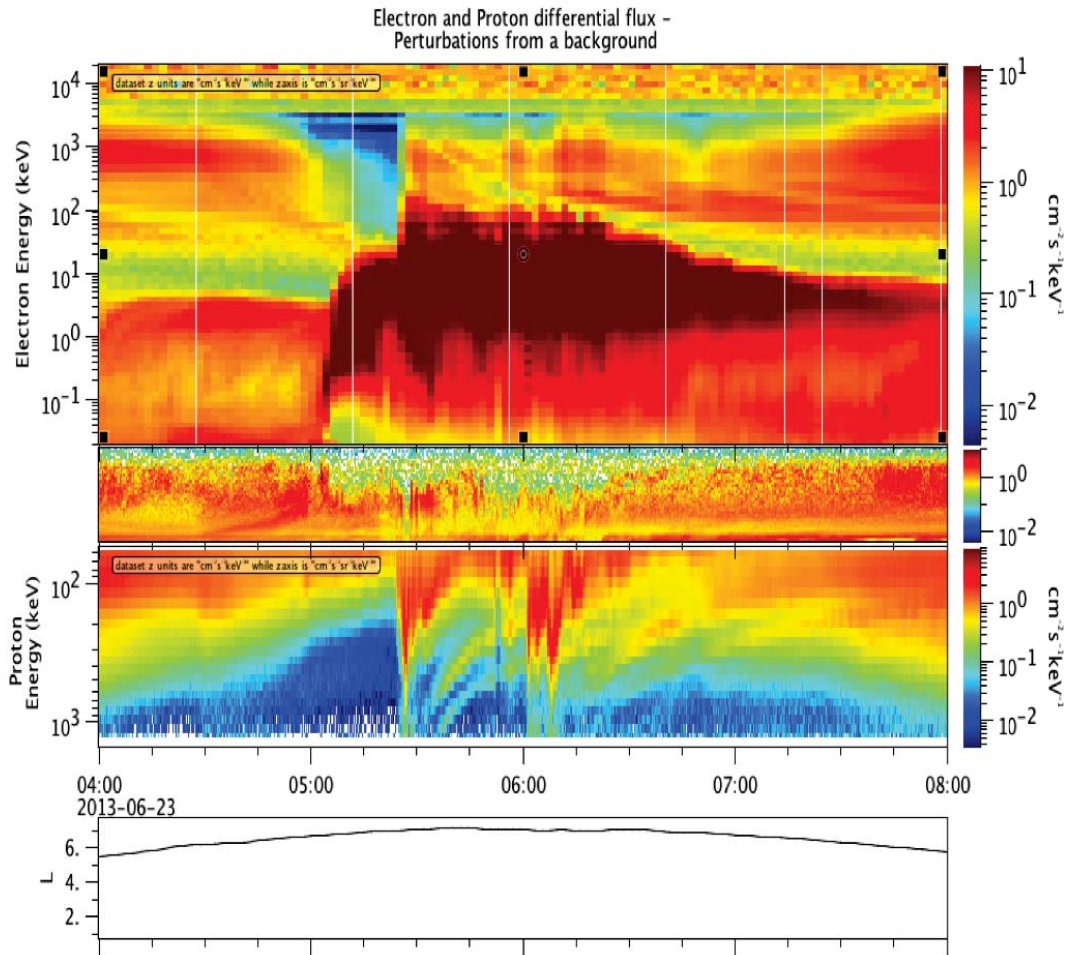Figure 3: Dispersionless injection observed by Van Allen Probe A on 23 June 2013 at 05:24 UT. Top panel- detrended differential electron flux observed form HOPE, MagEIS and REPT instruments. Middle two panels- detrended differential proton flux observed form HOPE, MagEIS and REPT instruments. Note unconventional plot axes- electron energy increasing upwards and proton energy increasing downwards. Bottom panel- satellite L-shell.
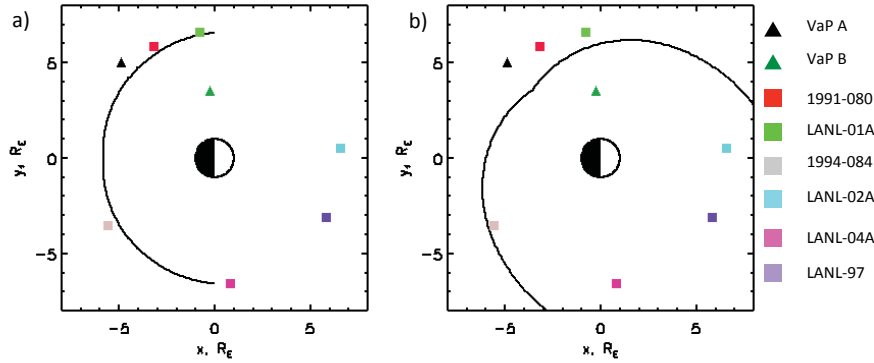
Figure 4: Locations of the LANL and Van Allen Probe satellites at the time of the substorm injection at 05:24 UT with*a)* an almost circular injection boundary symmetric round 00:00 MLT, *b)* a more pronounced double spiral boundary rotated by $\pi/4$

where r and ϕ are the particle coordinates in the equatorial plane, μ is the particle magnetic moment divided by q, and B is the dipole magnetic field strength in the equatorial plane. The electric potential is given by

$$\Phi = -\frac{91.5 \text{ keV}}{r} + \Phi_{\text{CONV}}$$

where Φ_{CONV} is the Volland-Stern electric field and is given in Ejiri (1978).

$$\Phi_{\text{CONV}} = AR^{\gamma} sin\phi$$

where

$$A = \frac{0.045}{(1 - 0.159 \text{Kp} + 0.0093 \text{Kp}^2)^3} \text{kV/R}_E^2$$

and the shielding factor, $\gamma = 2$ as proposed by Volland (1973) and Stern (1975).

If the particle traces back to the injection boundary it is colour coded depending on its MLT at the time of injection. The colours used are shown in Figure 2*b*.

Electrons and protons with energies 0 - 500 keV are traced back to the time of injection. If they originate from behind the injection boundary they are coloured according to the MLT of their initial location. This is done for the dispersion less injection observed by Van Allen Probe (VAP) A and is shown in Figure 5. At the time of injection VAP A is located at ~ 21:00 MLT. The models give a direct comparison with the observations, allowing us to determine whether there are flux enhancements as expected due to an injection region spanning from dawn to dusk, or otherwise a more localised injection region. The model shows that there is an instantaneous enhancement in particle flux from the 20:00-22:00 MLT (orange) region at the time of the injection. This is because the satellite is in the injection region at the time of injection. Shortly after high energy electrons from 18:00-20:00 MLT (yellow) are observed at the satellite and high energy protons from 22:00-00:00 MLT (red) and 00:00-02:00 MLT (green). Drift echoes are also predicted, but only clearly visible from observations in the proton data. The patterns observed as the satellite travels back out to apogee on subsequent orbits is also visible. These are very similar to the structures observed in the differential flux spectogram where protons with 10s keV arrive at the satellite before lower energy protons and electrons, followed by electrons of a similar energy. This type of dispersion is visible in the observational data on the second orbit after the injection. The first and second injection boundary topology gives very similar results for the model, however the flux enhancement for the more rotated boundary lasts for a much longer time as the satellite is located further tail ward of the boundary in this case.

The injection was also observed by other spacecraft located behind the injection region as shown in Figure 4. The LANL-01A spacecraft which was located at ~ 18:30 MLT also observed a dispersion less injection as shown in

Figure 6. This suggests that this satellite is also in the injection region, meaning that it spans at least form ~ 18:30-21:00 MLT. Again the flux enhancements in Figure 6*e* last longer than in *c* as the satellite is located further from the boundary in this case. The two modelled dispersion patterns do not differ enough from each other to be able to deduce whether the first or second injection boundary is more realistic.

Spacecraft 1994-084 was located at ~ 02:00 MLT at the time of the injection. At this satellite no obvious flux enhancement is observed, however according to Figure 7*b* the satellite is located behind the injection boundary and therefore is expected to see a dispersionless injection. Even if the satellite is Earthward of the injection region we would still expect to see a slightly dispersed signature shortly after the injection. From the data there is a flux enhancement visible around the 100 keV electrons, however nothing at lower energies or in the proton data. The model from the first injection boundary predicts a dispersion less injection at 05:24 UT from the 02:00-04:00 MLT (light blue) region. This is clearly not visible in the observations. However the flux enhancement in high energy electrons originates from the pre midnight 22:00-00:00 region. This suggests that particles in the post midnight region behind the injection boundary are not energised. In order to test this the boundary was rotated in such a way that the satellite was not behind the boundary at the time of injection. However the complex signature expected to be observed at a later time in both electrons and ions from the 02:00-04:00 MLT region is not observed. This suggests that the injection region in this case does not span from dawn to dusk and is more localised in MLT towards the pre-midnight sector.

6. Conclusions & Further Work

From this study we can see that the patterns observed in low energy electron and proton Van Allen Probe data in orbits after a substorm injection can be explained by simple particle drifts. The patterns observed differ from the models due to the steady-state conditions used to run the model. In reality the strength of the convection electric field changes on shorter timescales. In our example the influence of a substorm injection can be measured in the inner magnetosphere up to two orbits later.

Using measurements from multiple spacecraft it is possible to narrow down the MLT width of the injection region for individual events and compare the differential flux enhancements and dispersion patterns with those predicted by particle drifts. These methods can also allow future investigations into the shape of the injection region, whether it is centred around midnight, and how far behind the injection region the particles are energised. Future work on this subject includes:

- Investigating the shape of the injection boundary and the effect on the expected dispersion pattern. This can include how important a rounded/spiral injection boundary is to reproduce observations.

- It is unclear how much the width of the energisation behind the injection boundary affects dispersion patterns.

- The effect of rotating the boundary on the dispersion patterns

- Testing the consistency between observations of injections and the results from the model.

References

Bame, S.J., McComas, D.J., Thomsen, M.F., Barraclough, B.L., Elphic, R.C., Glore, J.P., Gosling, J.T., Chavez, J.C., Evans, E.P., Wymer, F.J., 1993. Magnetospheric plasma analyzer for spacecraft with constrained resources. Review of Scientific Instruments 64, 1026–1033.

Belian, R.D., Baker, D.N., Hones, E.W., Higbie, P.R., Bame, S.J., Asbridge, J.R., 1981. Timing of energetic proton enhancements relative to magnetospheric substorm activity and its implication for substorm theories. Journal of Geophysical Research: Space Physics 86, 1415–1421.

Belian, R.D., Gisler, G.R., Cayton, T., Christensen, R., 1992. High-z energetic particles at geosynchronous orbit during the great solar proton event series of october 1989. Journal of Geophysical Research: Space Physics 97, 16897–16906.

Buzulukova, N.Y., Galperin, Y.I., Kovrazhkin, R.A., Glazunov, A.L., Vladimirova, G.A., Stenuit, H., Sauvaud, J.A., Delcourt, D.C., 2002. Two types of ion spectral gaps in the quiet inner magnetosphere: Interball-2 observations and modeling. Annales Geophysicae 20, 349–364.

Ejiri, M., 1978. Trajectory traces of charged particles in the magnetosphere. Journal of Geophysical Research: Space Physics 83, 4798–4810.

Kavanagh, L.D., Freeman, J.W., Chen, A.J., 1968. Plasma flow in the magnetosphere. Journal of Geophysical Research 73, 5511–5519.

Konradi, A., 1967. Proton events in the magnetosphere associated with magnetic bays. Journal of Geophysical Research 72, 3829–3841.

Lanzerotti, L.J., Maclennan, C.G., Robbins, M.F., 1971. Proton drift echoes in the magnetosphere. Journal of Geophysical Research 76, 259–263.

Mauk, B.H., Meng, C.I., 1983. Characterization of geostationary particle signatures based on the injection boundary model. Journal of Geophysical Research: Space Physics 88, 3055–3071.

McIlwain, C.E., 1974. Substorm injection boundaries, in: McCormac, B.M. (Ed.), Magnetospheric Physics, pp. 143–154.

Stern, D.P., 1975. The motion of a proton in the equatorial magnetosphere. Journal of Geophysical Research: Space Physics 80, 595–599.

Volland, H., 1973. A semiempirical model of large-scale magnetospheric electric fields. Journal of Geophysical Research: Space Physics 78, 171–180.

Figure 5: *a)* Detrended differential electron and proton flux on 23 June 2013 for Van Allen Probe A which is at ∼ 21:00 MLT at the time of injection. The dispersionless injection is visible at 05:24UT. *b)* The injection boundary used for the modelled dispersion pattern in *c)*. *c)* The modelled dispersion pattern where the colours indicate whether a particle from the injection region has access to the satellite at a particular time and if so, the MLT sector from which the particle originates. *d)* The double spiral rotated by $\pi/4$ injection boundary used in *e)* for the modelled dispersion pattern. *e)* The modelled dispersion pattern using a rotated injection boundary. The axes for the observations and models are in the same layout as Figure 3.
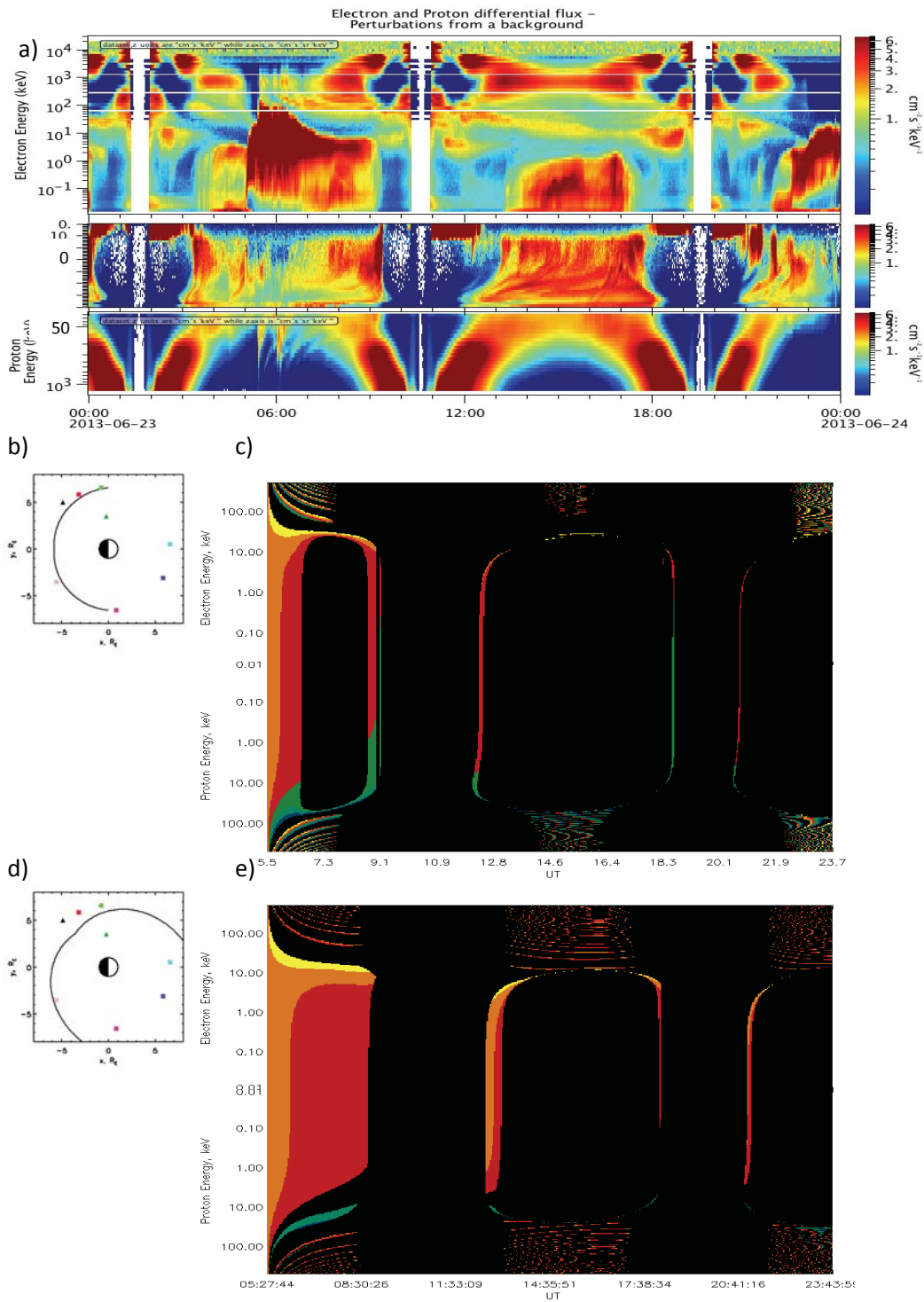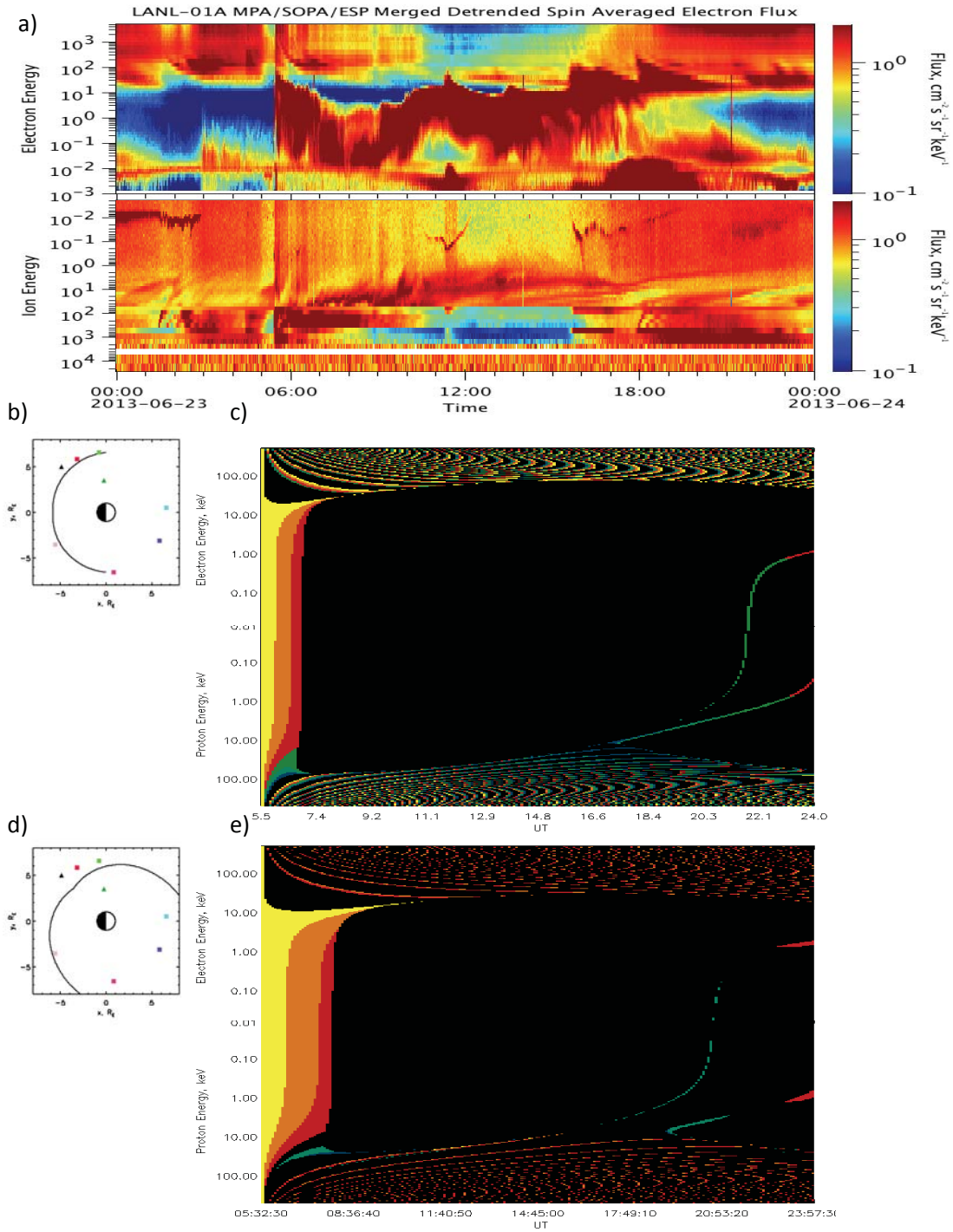
Figure 6: *a)* Detrended differential electron and proton flux on 23 June 2013 for LANL-01A which is at ∼ 18:30 MLT at the time of injection. At this satellite a dispersionless injection is also observed at 05:24 UT. *b)* The injection boundary used for the modelled dispersion pattern in *c)*. *c)* The modelled dispersion pattern where the colours indicate whether a particle from the injection region has access to the satellite at a particular time and if so, the MLT sector from which the particle originates. *d)* The double spiral rotated by $\pi/4$ injection boundary used in *e)* for the modelled dispersion pattern. *e)* The modelled dispersion pattern using a rotated injection boundary. The axes for the observations and models are in the same layout as Figure 3.
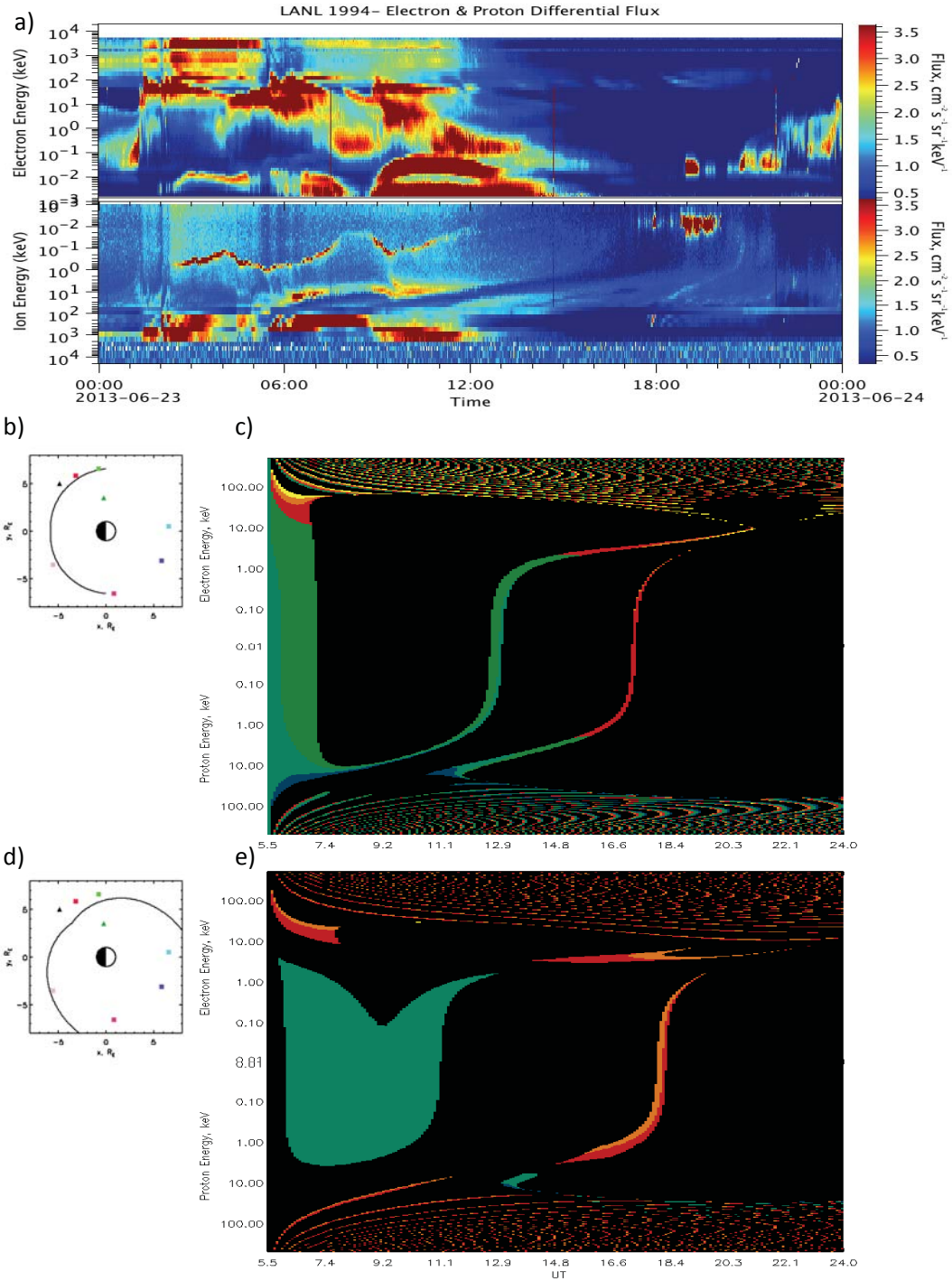
Figure 7: *a)* Detrended differential electron and proton flux on 23 June 2013 for 1994-084 which is located at ~ 02:00 MLT at the time of injection. At this satellite no obvious flux enhancement is observed at the time of injection even though the spacecraft is located behind the injection boundary dispersion less injection is expected. *b)* The injection boundary used for the modelled dispersion pattern in *c)*. *c)* The modelled dispersion pattern where the colours indicate whether a particle from the injection region has access to the satellite at a particular time and if so, the MLT sector from which the particle originates. *d)* The double spiral rotated by $\pi/4$ injection boundary used in *e)* for the modelled dispersion pattern. *e)* The modelled dispersion pattern using a rotated injection boundary. The axes for the observations and models are in the same layout as Figure 3.

Heavy Ion Effects on Kelvin-Helmholtz Instability: Hybrid Study

Dong Lin

Department of Electrical & Computer Engineering, Virginia Polytechnic Institute and State University, Blacksburg, VA.

Misa Cowee, Dan Winske, Xiangrong Fu

Los Alamos National Laboratory, Los Alamos, NM

Abstract

We investigated the effects of heavy ions on the Kelvin-Helmholtz instability (KHI) via hybrid simulation. In a two-dimensional setup, the density and temperature is uniform across the shear layer. The magnetic field is also uniform and perpendicular to the simulation plane. The heavy ion effects are explored by varying the mass number of the ion species while keeping the mass density constant for four simulation runs. The mass numbers involved are 1, 4, 8 and 16. By doing spatial Fourier analysis for the perpendicular velocity disturbance on the central line of the simulation box, we characterized the growth rate of the KH instability for different wave mode numbers. The wave mode dependent growth rate is compared with theoretical predictions and good agreement is found. Comparison of growth rates for different ion species shows the instability grows slower with a heavier ion species. Possible influences of shear layer thickness, system size, and grid spacing are discussed.

Keywords: Kelvin-Helmholtz Instabiltiy, Heavy Ion, Hybrid Simulation

1. Introduction

KHI is also called the "wind-blow-water instability" in fluid dynamics, which occurs on the interface of two fluids when there is a strong velocity shear. Such a strongly sheared interface is also present in space plasma, which is often characterized by magnetohydrodynamics (MHD). KHI is suggested as a candidate mechanism in solar wind-magnetosphere coupling and contributes to the transport of solar wind mass, momentum and energy into the magnetosphere (*Hasegawa et al.*, 2004). An early estimation by *Pu and Kivelson* (1983) shows that the energy power supplied to the magnetosphere by KHI is only next to that by magnetic reconnection and preponderates over other mechanisms like diffusion, injection, etc.

The linear MHD theory of *Chandrasekhar* (1961) gives the unstable criteria:

$$[\vec{k} \cdot (\vec{V}_1 - \vec{V}_2)]^2 > \frac{\rho_1 + \rho_2}{\mu_0 \rho_1 \rho_2}[(\vec{k} \cdot \vec{B}_1)^2 + \vec{k} \cdot \vec{B}_2)^2] \tag{1}$$

and the growth rate on an infinitely thin shear layer:

$$\gamma = \sqrt{\frac{\rho_1 \rho_2}{(\rho_1 + \rho_2)^2}[\vec{k} \cdot (\vec{V}_1 - \vec{V}_2)]^2 - \frac{\rho_1}{\rho_1 + \rho_2}(\vec{k} \cdot \vec{V}_{A1})^2 - \frac{\rho_2}{\rho_1 + \rho_2}(\vec{k} \cdot \vec{V}_{A2})^2} \tag{2}$$

where the subscripts "1" and "2" denote the velocity, mass density, and magnetic field at the two sides of the shear layer. From the unstable criteria we see that the most unstable condition is when the magnetic field is perpendicular to the velocity shear. Based on the frame work of MHD, *Miura and Pritchett* (1982) did eigen-mode analysis for the instability growth rate dependence on the wave number. Figure 1 gives the result for the case of magnetic field
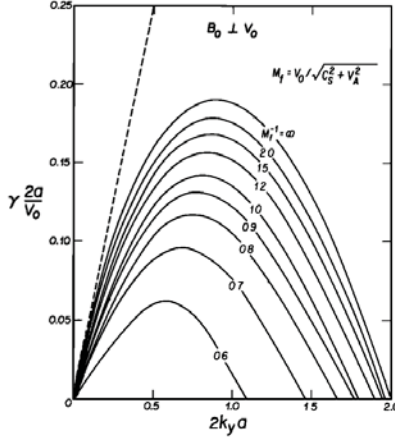
Figure 1: Normalized growth rate dependence on the normalized wavenumber for inverse magnetosonic Mach numbers ranging from 0.6 to ∞ from the eigen-mode analysis of *Miura and Pritchett* (1982).

Table 1: Parameters of the hybrid simulation

n_0	B_0	$T_i = T_e$	$\beta_i = \beta_e$	ω_{ci}^{-1}	$l_0 = c/\omega_{ci}$	V_A
$5cm^{-3}$	20 nT	10 eV	0.05	0.5 s	101 km	195 km/s
Grids	NPPC	Size	η	dt	2a	V_0
512^2	200	$(160l_0)^2$	10^{-4}	$0.05\ \omega_{ci}^{-1}$	$2.0l_0$	$1.0V_A$

perpendicular to the velocity with different magnetosonic Mach numbers. The fastest growing mode generally falls in the range of

$$0.5 < k \cdot 2a < 1.0 \tag{3}$$

where $k \cdot 2a$ is the wavenumber k normalized by the initial shear width $2a$. The growth rate γ is normalized by $2a/V_0$, where V_0 is the total velocity shear.

The KHI has been frequently seen in the observations of diverse spacecraft. The statistical study of *Lin et al.* (2014) shows the occurrence of KHI on the magnetopause from the dayside to the nightside. At the same time, heavy ions are also reported to dominate the magnetopause for as much as 30% of the time on the dusk side (*Bouhram et al.*, 2005). Possible sources of these heavy ions include O^+ from the ionospheric outflow, He^{++} and other ion species from the solar wind, and so on.

The MHD theory does not include any ion effects and the growth rate appears to be the same for different ion species. Previous studies on the possible influences of heavy ions have not yet come to an agreement. On one hand, the heavy ions will contribute to a higher mass density, and thus lower the Alfvèn speed and reduce the magnetic tension effects. The instability threshold is supposed to decrease (e.g., *Johnson et al.*, 2009; *Yu and Ridley*, 2013). On the other hand, heavy ions have stronger inertial effects as single particles. They are thought to be able to stream through the KH vortices and break them down. Consequently, the instability is likely to be suppressed and mixing reduced (e.g., *Delamere et al.*, 2011; *Merkin*, 2011). With these competing hypotheses, it naturally raises the question: do heavy ions promote or inhibit the KH instability?

2. Methodology

Since we are interested in the potential ion effects, the hybrid model in which ions are treated as particles and electrons as massless fluid (*Winske et al.*, 2003) would be an appropriate method. The hybrid simulation could study phenomena on the spatial scale of ion inertial length and gyro-radius with a low frequency approximation for the

electromagnetic fields. Here are the basic equations for the hybrid model (*Winske and Omidi*, 1993):

$$\nabla \times \vec{B} = \frac{4\pi}{c}\vec{J} \tag{4}$$

$$\nabla \times \vec{E} = -\frac{1}{c}\frac{\partial \vec{B}}{\partial t} \tag{5}$$

$$\nabla \cdot \vec{B} = 0 \tag{6}$$

$$\frac{\partial}{\partial t}n_e m_e \vec{V}_e = 0 = -en_e(\vec{E} + \frac{\vec{V}_e \times \vec{B}}{c}) - \nabla \cdot \overset{\leftrightarrow}{P}_e + en_e \overset{\leftrightarrow}{R} \cdot \vec{J} \tag{7}$$

$$\frac{d\vec{x}_i}{dt} = \vec{v}_i \tag{8}$$

$$m_i \frac{d\vec{v}_i}{dt} = q_i(\vec{E} + \frac{\vec{v}_i \times \vec{B}}{c}) - q_i\eta\vec{J} \tag{9}$$

The pressure and resistivity tensor are simplified as isotropic. The electron and ion number density are connected by the charge neutrality condition, namely we do not solve the Poisson's equation in this hybrid model. Thus we have the following additional equations:

$$\overset{\leftrightarrow}{P}_e = n_e T_e \overset{\leftrightarrow}{I} \tag{10}$$

$$\overset{\leftrightarrow}{R} = \eta \overset{\leftrightarrow}{I} \tag{11}$$

$$n_i q_i = n_e q_e \tag{12}$$

$$\vec{J} = n_e q_e(\vec{V}_i - \vec{V}_e) \tag{13}$$

In this summer program, we started with the simplest situation of two-dimensions with only one ion species involved in each run. The mass density is uniform across the shear layer and kept as a constant for different runs. The magnetic field is set to be perpendicular to the simulation plane, which is the most unstable configuration as discussed before. The boundary is periodic in the flow direction Y and reflecting in the other direction X. Typical values in spacecraft observations are adopted for the plasma and magnetic field, as shown in Table 1. The simulation system size is $160l_0 \times 160l_0$, where l_0 is the ion inertial length, with 512×512 grid cells. The number of super particles per cell is 200. We use a numerical resistivity of $\eta = 10^{-4}$ and time step of $0.05\omega_{ci}^{-1}$, where ω_{ci}^{-1} is the inverse of ion gyro frequency. The shear width is $2l_0$ and velocity shear is $1.0V_A$, where V_A is the plasma Alfvèn speed. In the shear layer, the transition of shear velocity is proscribed by the typical hyperbolic tangent function:
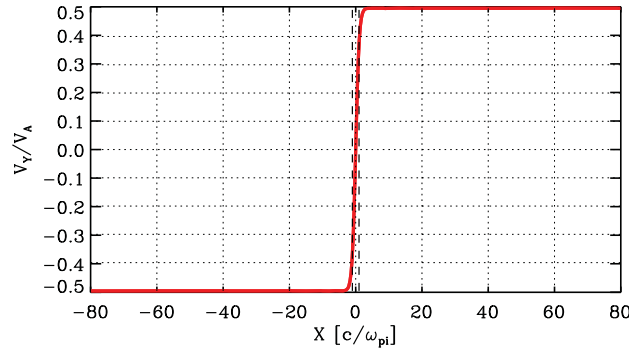
$$V_Y = \frac{V_0}{2}tanh(\frac{X}{a}) \tag{14}$$

Figure 2: Velocity profile at the initial time.

3. Results

3.1. The case of protons

We started with the most fundamental ion species: protons. Figure 2 shows the flow velocity profile in the beginning of the simulation. The dash lines denote the nominal width of the shear layer. Figure 3 gives the simulation
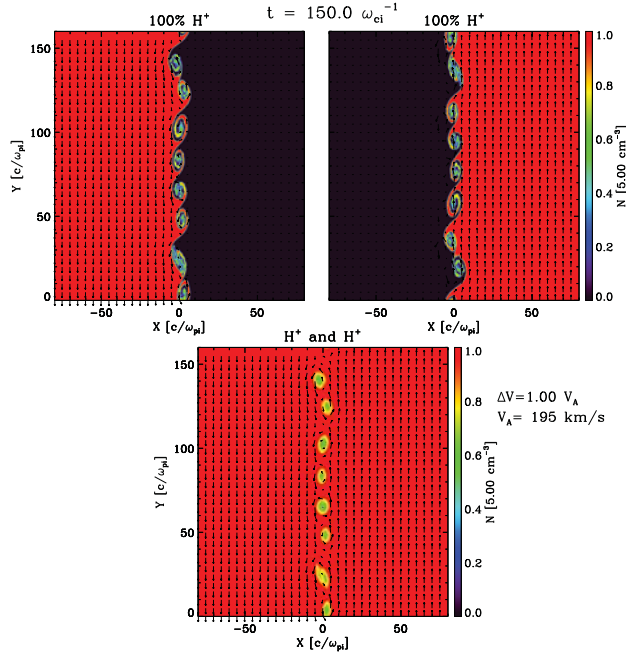
Figure 3: Density contour and flow field at $t = 150\omega_{ci}^{-1}$.

result of KHI for protons. The top left panel gives the density contour and flow field at $t = 150\omega_{ci}^{-1}$ for ions initially located at the left side of the shear layer, and top right panel for ions initially at the right. The bottom panel plots the total density and velocity distribution. About eight KH vortices can been seen from the density contour. The coalescence of vortices to larger ones is also evident. In order to quantify the growth rate of the instability, a spatial

Figure 4: Temporal evolution of the spatial Fourier spectrum of perpendicular velocity disturbance at $X = 0$.

Fourier transform is performed for the perpendicular velocity disturbance on the central line of the simulation domain.

Figure 4 is a collage of the Fourier spectrum of each time moment. The vertical axis is the wavenumber normalized by the shear width. The color bar gives the magnitude of the velocity disturbance Fourier spectrum. The white curve is the connected peak spectrum at each time. The decrease of dominant 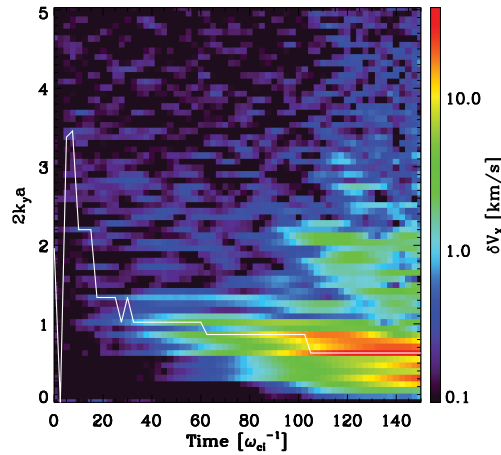spatial frequency, namely the wavenumber, is a representation of the inverse cascade. The KH vortices are evolving into longer wavelengths with time, which can be also seen in the density plot.

As a comparison with the linear theory prediction by *Miura and Pritchett* (1982), we calculated the growth rates for individual wave modes around the fastest growing mode. The growth profiles of Fourier spectrum is plotted in Figure 5 in the logarithm manner. The discrete normalized wavenumbers used here are $k \cdot 2a = 0.31, 0.39, 0.55, 0.63,$ and 0.71, as shown in the first five panels. The red dash-dotted line is a linear fitting to get the growth rate. Combining the results of these growth rates and wavenumbers, we get a similar pattern to that in Figure 1 in the bottom right panel. The inverse magnetosonic Mach number in this case is calculated to be 1.0. The fastest growing mode has $k \cdot 2a = 0.55$ with a growth rate of $\gamma \, 2a/V_0 = 0.12$, in agreement with linear theory predictions.
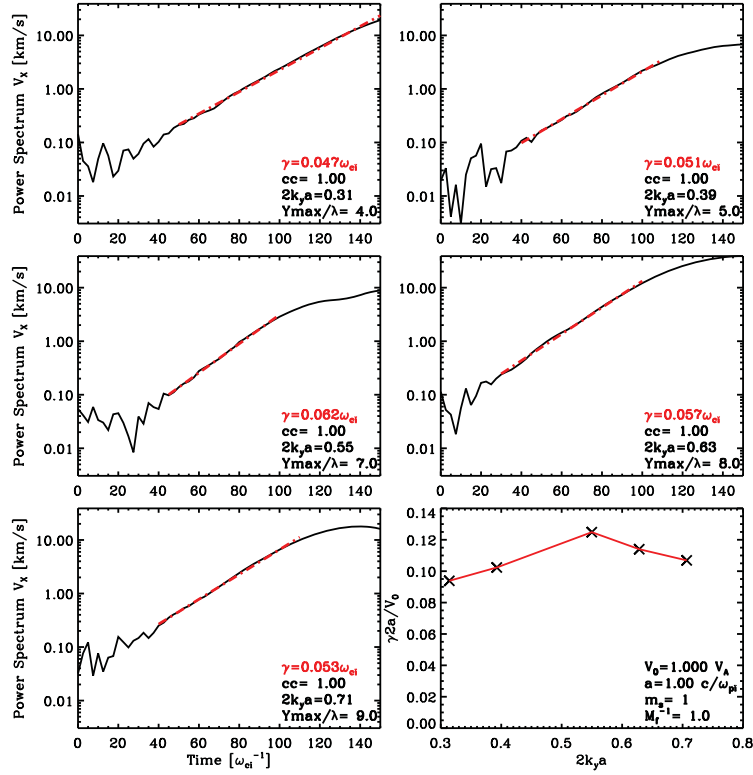

Figure 5: Growth profile of individual wave modes and growth rate with wave number.

3.2. *Varying the ion mass number*

We explore the heavy ion effects by testing the following mass numbers: 1, 4, 8, and 16. The mass density hence Alfvèn speed, systems size, velocity shear, and shear width are all kept constant and the same as used in the proton case. Figure 6 gives an overview of the instability growth for different ion species. The four rows correspond to the four mass numbers, and the four columns are for $t = 0, 50, 100,$ and $150 \, \omega_{ci}^{-1}$. In all the four cases, the instabilities have evolved into the stage of several dominant wavelength occupying the simulation box. Qualitatively, there is a trend that the case of a heavier ion species grows slower than that of a lighter ion species.

With the similar method to calculate the growth rate in the previous subsection, we get the growth rate curves for all the species in Figure 7. The black, red, green, and blue curves stand for the growth rate patterns of mass numbers of 1, 4, 8, and 16. They all have a fastest growing wavenumber around $k \cdot 2a = 0.5$ and fastest growing rate around $\gamma \, 2a/V_0 = 0.10$. There is a trend that the growth rate is lower for heavier ion species. This pattern is consistent with the
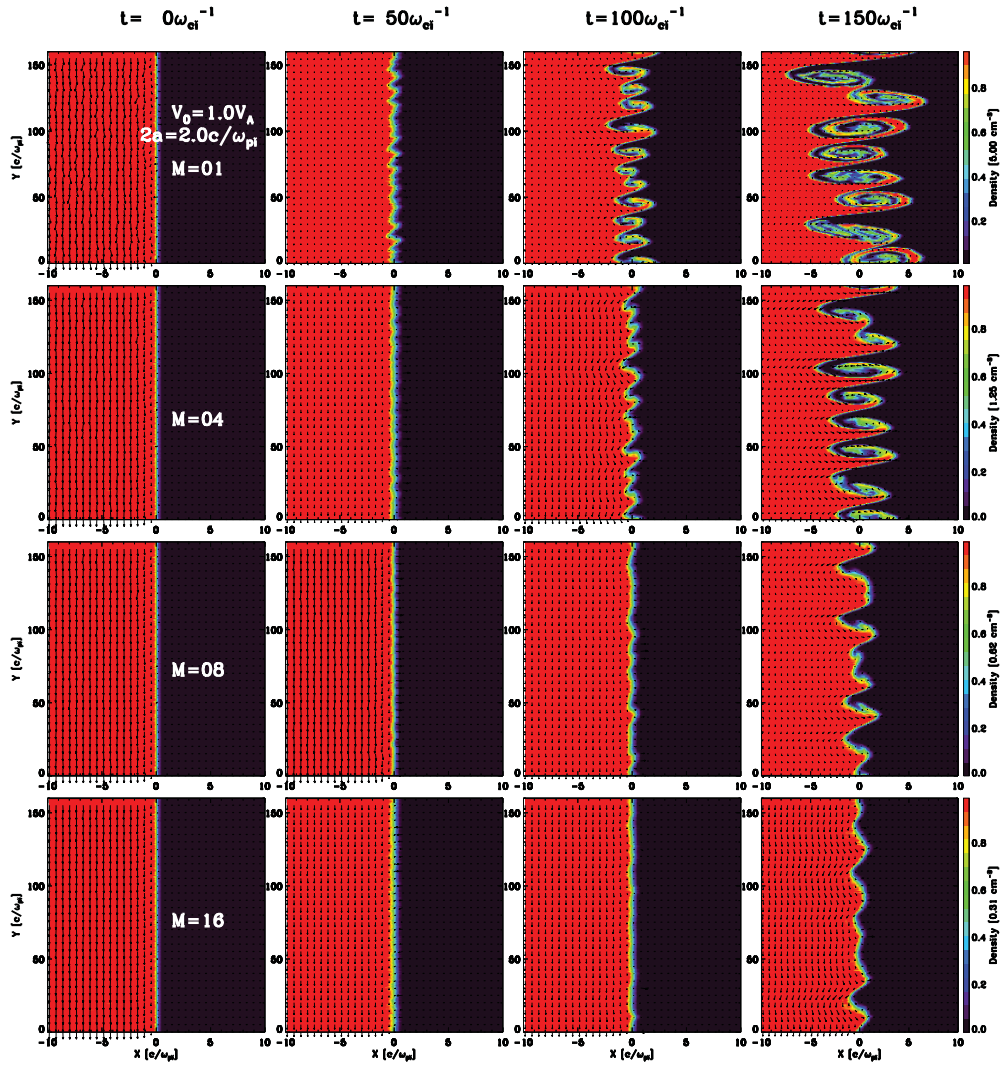
Figure 6: KHI growth for different ion species: mass number $M = 1, 4, 8, 16$.

result of Case 3 in *Delamere et al.* (2011) although the dependence of growth rate on wavenumber is not discussed in that study.

3.3. Additional sensitivity tests

Before we attempt to find a physical explanation for the growth rate pattern found above, we did several more sensitivity tests of growth rate to the shear width, grid spacing, and system size. In a simulation box of $80l_0 \times 80l_0$, we vary the shear width $2a$ among 0.32, 0.62, 1.24, 2.00, to 4.00. The corresponding growth rate curves are shown in Figure 8 with black, red, green, blue, and yellow, respectively. Note the legend in Figure 8 is for half shear width a. Only when $2a = 1.24, 2.00$ can we see a growth rate curve close to the prediction. For too wide or too narrow shear width, the fastest growing mode and growth rate are much deviated from the predicted value. For the too narrow case, for example $2a = 0.32$, the shear width is just around one grid cell. The transition of shear velocity would be too abrupt on the grids. For too wide shear width in a given system size, the limiting effects of the boundaries in the perpendicular direction may come out. Thus it is necessary to find out the appropriate range of shear width given the system size of a simulation box.

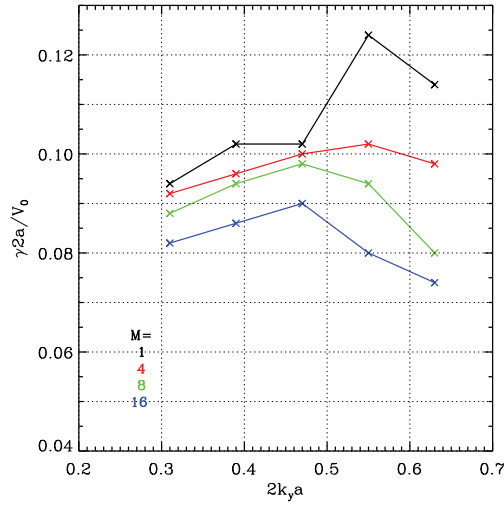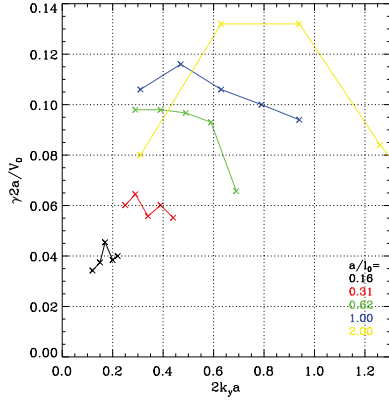Figure 7: KHI growth rate with wavenumber for different ion species: mass number $M = 1, 4, 8, 16$.

Figure 8: KHI growth rate with wavenumber for different shear widths: $a = 0.16$ (black), 0.31 (red), 0.62 (green), 1.00 (blue), and 2.00 (yellow).
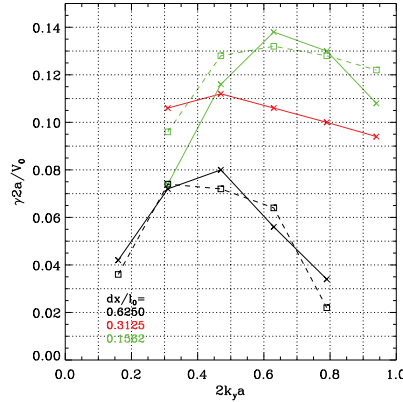
Figure 9: KHI growth rate with wavenumber for different grid spacings: $dx = 0.6250$ (black), 0.3125 (red), and 0.1562 (green).
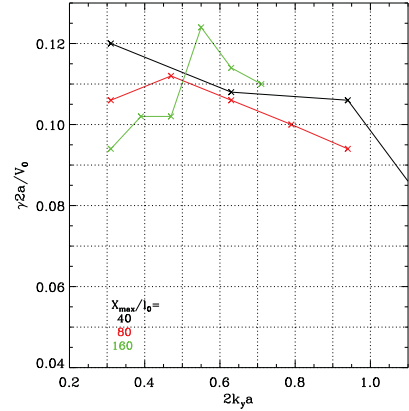
Figure 10: KHI growth rate with wavenumber for different system sizes: $X_{max} = 40\ l_0$ (black), 80 l_0 (red), and 160 l_0 (green).

The grid spacing and system size give the lower and upper limit of wavelength that could be resolved. In a system size of 80 $l_0 \times 80\ l_0$, we tested the effects of grid spacing by varying the number of grid cells from 128^2, 256^2 to 512^2, shown by the black, red, and green curves, respectively in Figure 9. The black and green dashed lines are when the number of super particles per cell is 400 for $dx = 0.6250$ and 100 for $dx = 0.1562$ so that the total number of super particles is all the same for three grid spacings. It is found that the growth rate for a larger grid spacing is relatively lower. The number of super particles per cell does not produce significant changes. This could result from that more short wavelength modes are cut off by a larger grid cell, thus reducing the number of seeds for the instability growth, or could be due to numerical effects associated with the initial conditions.

In another sensitivity test, the system size X_{max} is the only variable: 40 $l_0 \times 40\ l_0$, 80 $l_0 \times 80\ l_0$, 160 $l_0 \times 160\ l_0$. The growth rate curves are basically unchanged, which maybe because the instability has not evolved to a wavelength comparable to the system size by the time the growth rate is calculated.

4. Summary

In this study, we use the hybrid model to simulate the KHI for different ion species. The growth rate dependence on wavenumber is in good agreement with the linear theory prediction of *Miura and Pritchett* (1982). As the mass number of the ions increases to 4, 8, and 16, the growth rate appears to decrease. The test runnings show that instability growth is also sensitive to the shear width, grid spacing. Although variations of growth rate caused by shear width and/or grid spacing may be attributed to numerical effects, it is necessary to have more tests to validate the outcomes for further study.

The linear theory of *Miura and Pritchett* (1982) is essentially based on the frame work of MHD. It is important to derive the linear theory for kinetic KHI in the future research. Full particle simulations of *Nakamura et al.* (2010) have shown that the shear layer is prone to broaden if the initial width is comparable to or less than one ion gyro-radius when the vorticity of shear flow is anti-parallel to the magnetic field. It is thus noteworthy if these broadening effects are strengthened by the presence of a heavier ion species, whose gyro-radius is larger. We have not considered the magnetic shear in this study. When the instability is stabilized by the parallel magnetic tension, the difference between ion species may stand out. Thus runs with a finite magnetic shear are suggested for future work to provide helpful hints for the investigation of heavy ion effects on the Kelvin-Helmholtz instability.

5. References

Bouhram, M., B. Klecker, G. Paschmann, and et al. (2005), Survey of energetic O+ ions near the dayside mid-latitude magnetopause with Cluster, *Ann. Geophys.*, *23*, 1281–1294

Chandrasekhar, S. (Ed.) (1961), *Hydrodynamic and Hydromagnetic Stability*, Oxford Univ. Press, New York.

Delamere, P. A., R.J.Wilson, A. Masters, Kelvin-Helmholtz instability at Saturn's magnetopause: hybrid simulations, *J. Geophys. Res.*, *116*, 10222, doi:10.1029/2011JA016724.

Hasegawa, H., M. Fujimoto, T. D. Phan, and et al. (2004), Transport of solar wind into Earth's magnetosphere through rolled-up Kelvin-Helmholtz vortices, *Nature*, *430*(7001), 755–758, doi:10.1038/nature02799.

Johnson, J., A. Otto, Y. Lin, and et al. (2009), Heavy ion effects on magnetopause transport, *AGU FallMeeting Abstracts*, 2

Lin, D., C. Wang, W. Li, and et al. (2014), Properties of Kelvin-Helmholtz waves at the magnetopause under northward interplanetary magnetic field: Statistical study, *J. Geophys. Res.*, *119*, 7485–7494, doi:10.1002/2014JA020379.

Merkin, V. G., Effects of ionospheric O+ on the magnetopause boundary wave activity, *American Institute of Physics Conference Series*, ed. by D. Vassiliadis et al., *1320*, 208–212, doi:10.1063/1.3544326.

Miura, A., and P. L. Pritchett (1982), Nonlocal stability analysis of the MHD Kelvin-Helmholtz instability in a compressible plasma, *J. Geophys. Res.*, *87*(A9), 7431–7444, doi:10.1029/JA087iA09p07431.

Nakamura, T. K. M., H. Hasegawa, I. Shinohara (2010), Kinetic effects on the Kelvin-Helmholtz instability in ion-to-magnetohydrodynamic scale transverse velocity shear layers: particle simulations, *Phys. Plasmas*, *17*(4), 042119. doi:10.1063/1.3385445.

Pu, Z. Y., and M. G. Kivelson (1983), Kelvin-Helmholtz instability at the magnetopause: Solution for compressible plasmas, *J. Geophys. Res.*, *88*(A2), 841–852, doi:10.1029/JA088iA02p00841.

Winske, D., and N. Omidi (1993), Hybrid codes. *Computer space plasma physics: Simulation techniques and software*, 103–160.

Winske, D., L. Yin, N. Omidi, and et al. (2003), Hybrid simulation codes: past, present and future-a tutorial, *Space Plasma Simulation*, 136–165, Springer Berlin Heidelberg.

Yu, Y., and A.J. Ridley (2013), Exploring the influence of ionospheric O+ outflow on magnetospheric dynamics: the effect of outflow intensity, *J. Geophys. Res.*, *118*, 5522–5531, doi:10.1002/jgra.50528.

Simulating Plasmaspheric Electron Densities with a Two-Component Electric Field Model

Sebastian De Pascuale

Department of Physics & Astronomy, University of Iowa, Iowa City, IA, 52242

Vania Jordanova

Los Alamos National Laboratory, Los Alamos, NM 87545

Abstract

We simulate equatorial plasmaspheric electron densities in the inner-magnetosphere with a fluid-physics model (RAM-CPL) based on empirical parameters governing the source and loss processes of refilling and erosion. A virtual plasmasphere is compared with Van Allen Probe (RBSP-A) EMFISIS density measurements along the orbital track of the satellite on 15 - 20 January, 2013. The evolution of the simulation is driven by a combined Volland-Stern and SAPS electric potential, parameterized by solar wind measurements and the K_p index respectively to account for the convection of plasma in the inner-magnetosphere. Globally, the simulations indicate the compression of the plasmapause boundary, defined as a low-density threshold of 20 cm^{-3}, to $L = 4$ and the narrowing of a plume-like structure of plasma during the onset of geomagnetic activity, which is consistent with other modeling efforts. Locally, the RAM-CPL simulation achieves favorable agreement within an order of magnitude of EMFISIS density measurements and a mean model-observation difference in plasmapause detections of $\Delta L_{AVG} = 0.52 \pm 0.15 R_E$. We discuss further the effects of EMFISIS density determinations and the parameterization of the convection electric field on this reported disagreement.

Keywords: plasmaspheric erosion & refilling, convection electric field, Van Allen Probes, RBSP, EMFISIS, EFW

1. Introduction

Entrained by Earth's dipolar magnetic field and subsequently corotating with the planet, the plasmasphere is a toroidal interface of cold, dense plasma (≤ 20 eV, $10 - 10^4$ cm^{-3}, and primarily H$^+$) coupled to the ionosphere and inner-magnetosphere (Lemaire and Gringauz, 1998). Dayside magnetic reconnection at the the magnetopause drives the sunward convection of near-Earth plasma caused by a duskward electric field, which contributes to the erosion of the plasmasphere and related dynamics on the order of hours during periods of geomagnetic activity (Carpenter and Lemaire, 1997). The time history of a geomagnetic storm further influences the formation of plume-like structures and other morphological features of the plasmasphere (Goldstein and Sandel, 2005; Darrouzet et al., 2009). Plasmaspheric drainage plumes, in particular, can interact with and modify regions of magnetic reconnection as they channel escaping plasma towards the magnetopause (Walsh et al., 2014). Nonetheless, the origin of plasma sustaining long-lived plumes is unknown, requiring full-scale simulations and further work to uncover the role of the plasmasphere on inner magnetospheric processes (Borovsky et al., 2014).

During periods of extended geomagnetic inactivity (Kp < 2), the plasmasphere refills more effectively from the continual supply of particles escaping from the dayside ionosphere (Darrouzet et al., 2009). Outflow along co-rotating flux tubes, dominated by the charge exchange reaction liberating H$^+$ protons, returns the plasmasphere to an extended state on a timescale of days that is dependent inversely on ionospheric latitude or inner-magnetospheric L-shell (Rasmussen et al., 1993). The outer boundary of the plasmasphere, the plasmapause, is identified as a discontinuity in the

---

radially decaying profile describing equatorial densities, and its location (from $3 < L < 8$) is inversely dependent on geomagnetic activity and well described by E x B convection models (Carpenter and Anderson, 1992; Goldstein et al., 2005). Specification of the forcing electric field can include modifications to simple convection from electromagnetically coupled plasma and particle populations in the ionosphere and inner-magnetosphere.

The subauroral polarization stream (SAPS) phenomenon, for example, arises from a global electrical circuit between the partial ring current during disturbance times and field-aligned and poleward Pedersen currents in the ionosphere. When this feedback effect is mapped from ionospheric latitudes to the inner-magnetosphere, SAPS accounts for radial electric fields producing westward flows in the plasmasphere (Goldstein et al., 2005). Thermal plasma density content in the plasmasphere is responsible for the collisional loss of ions and host to the plasma waves that scatter electrons from the surrounding hot (>1 keV) ring current and (>1 meV) radiation belts (Lyons, et al. 1998; Fok, et al. 1991; and Jordanova et al., 1996). The advanced ring-current atmosphere interaction and radiation belt model (RAM-SCB) is coupled to a time-dependent equatorial plasmaspheric density model (RAM-CPL; cold plasma) to study the acceleration, transport, and loss of energetic electrons and ions in the inner magnetosphere, a prime scientific objective of the recently completed main Van Allen Probes mission (Jordanova and Miyoshi 2005; Jordanova et al., 2010a, 2010b).

Formerly known as the Radiation Belt Storm Probes (and hereafter as RBSP-A & -B), the presently orbiting Van Allen Probes mission is providing a detailed perspective of the relationship between the plasma populations of the radiation belts, ring current, and plasmasphere. At near equatorial (10°) geostationary transfer orbits (period 9h), the two lapping satellites extend from a perigee of 600 km to an apogee of 5.8 R_E. Measurements of the electromagnetic environment allow direct contextualization of particle observations and associated plasma waves. The Electric Field and Waves (EFW) instrument (Wygant et al., 2013) measures three-axis electric fields driving the system and the spacecraft potential that serves as a proxy of the ambient plasma density. A reliable determination of the electron number density is obtained from frequency signatures in spectral data captured by the Electric and Magnetic Field Instrument Suite and Integrated Science (EMFISIS) suite (Kletzing et al., 2013; Kurth et al., 2015). These local in situ measurements can be compared to global models of the equatorial plasmasphere in order to constrain the dependence of its behavior on key variables.

Promoted by a host of specialized missions (multipoint, sounding, and imaging), the last decade of plasmaspheric research has focused on developing better understanding of the influence of geomagnetic events on the plasmasphere as a two-way coupling problem between the magnetosphere-plasmasphere and plasmasphere-ionosphere (Ganguli et al., 2000). Early empirical work utilized the identification of the plasma oscillation frequency, similar to the EMFISIS method (Kurth et al., 2015), to determine electron density profiles of half (00-15 hrs; Carpenter and Anderson, 1992) and full (00-24 hrs; Sheeley et al., 2001) MLT coverage. Recent analysis demonstrates that conventional empirical models fall short of reproducing observations when compared to direct *in situ* measurements, indicating that the ambient electron density of the plasmasphere is a critical parameter to theoretical wave and particle investigations (Ni et al., 2013; Thorne et al., 2013).

In this paper we assess the performance of equatorial plasmaspheric electron density simulations produced by RAM-CPL (cold plasma), a coupled component of the newly-developed RAM-SCB (eg. Jordanova et al., 2006). We consider two geomagnetic events on 15 - 20 January and 31 May - 5 June, 2013 during Van Allen Probes observations separated by a quarter sector in MLT from pre- to post-midnight regions. Although the initial and steady-state conditions of this study are static, the simulations are driven by an empirical description of the convection electric field chosen to reflect two distinct processes: magnetospheric dayside reconnection and sub global current system feedback in the ionosphere. We use the Kp geomagnetic activity index to parameterize the evolution of the plasmasphere and define a plasmapause boundary to systematically contextualize actual and virtual observations. For both events, the agreement in plasmapause location of the encounters was reproduced to within 0.50 Re. As the mean separation between spacecraft during both of these events is $\sim$ .5 L, we present simulation comparisons at a resolution of .5 hr MLT by 0.25 L bins against RBSP-A only, and for brevity will discuss only the results from the 15 - 20 January, 2013 event.

The subsequent sections of this paper are organized in the following manner: we describe the RAM-CPL modeling scheme used in this study and the representations for the source and loss processes of refilling and erosion, then we highlight density features of the EMFISIS observations captured by the simulation, and close by presenting an assessment of using RAM-CPL to provide plasmapause locations as a threshold in density. Future work will be discussed following a summary of the results of this study.

2. Modeling Framework

We ran two simulations of the ring-current atmosphere interaction cold plasma (RAM-CPL) in order to validate empirical models describing convective erosion and ionospheric refilling of the plasmasphere when compared to measurements obtained by the Van Allen Probes. A series of similar studies carried out by Liemohn et al. (2004, 2005, and 2006) linked RAM to the Dynamic Global Core Plasma Model (DGCPM; Ober et al. 1997) and found that coupling to the ring current and ionosphere for calculation of a self-consistent inner magnetospheric electric field better reproduced plasmapause locations as extracted from IMAGE EUV observations. DGCPM, while solving for total magnetic flux tube density content by a continuity equation in the same manner as RAM-CPL, is developed separately to be integrated with arbitrary magnetic and electric field specifications as well as to be coupled to other codes (Chen and Wolf, 1972; Rasmussen et al., 1993). We study RAM-CPL, which can also specify an arbitrary electric field, as a subroutine of the existing RAM suite to assess its utility in describing inner-magnetospheric cold plasma.

The two-dimensional equatorial plasmaspheric electron density model of RAM-CPL (illustrated in **Figure 1**) incorporates a parametric function of particle refilling due to ionosphere-magnetosphere coupling during $\mathbf{E}$ x $\mathbf{B}$ plasmaspheric evolution (Rasmussen et al., 1993). Two empirically derived components, a static refilling rate and a time-dependent driver, are utilized to dynamically progress the simulated configuration of plasma through the observed history of a geomagnetic event. The simulation will be compared to RBSP-A EMFISIS measurements by flying a virtual satellite through its orbit in the model plasmasphere output to record electric field and electron density values. A detailed examination of the role of a duskward electric field on ring current and plasmasphere formation for the 31 May - 5 June, 2013 storm is carried out by the work Thaller et al., 2015, which indicates that the EFW measured enhanced electric field is coincident with plasmasphere erosion. As an additional metric of comparison, the plasmapause will be defined as a low-density threshold of 20 cm^{-3} for the outermost occurrence (in L) of the number density level. This value is chosen to correspond to the same signatures identified in Goldstein et al., 2014's plasmapause test particle (PTP) $\mathbf{E}$ x $\mathbf{B}$ study of the 15 - 20 January, 2013 event, which reports a 0.40 ± 0.05 R_E mean model-data difference in radial plasmapause location.
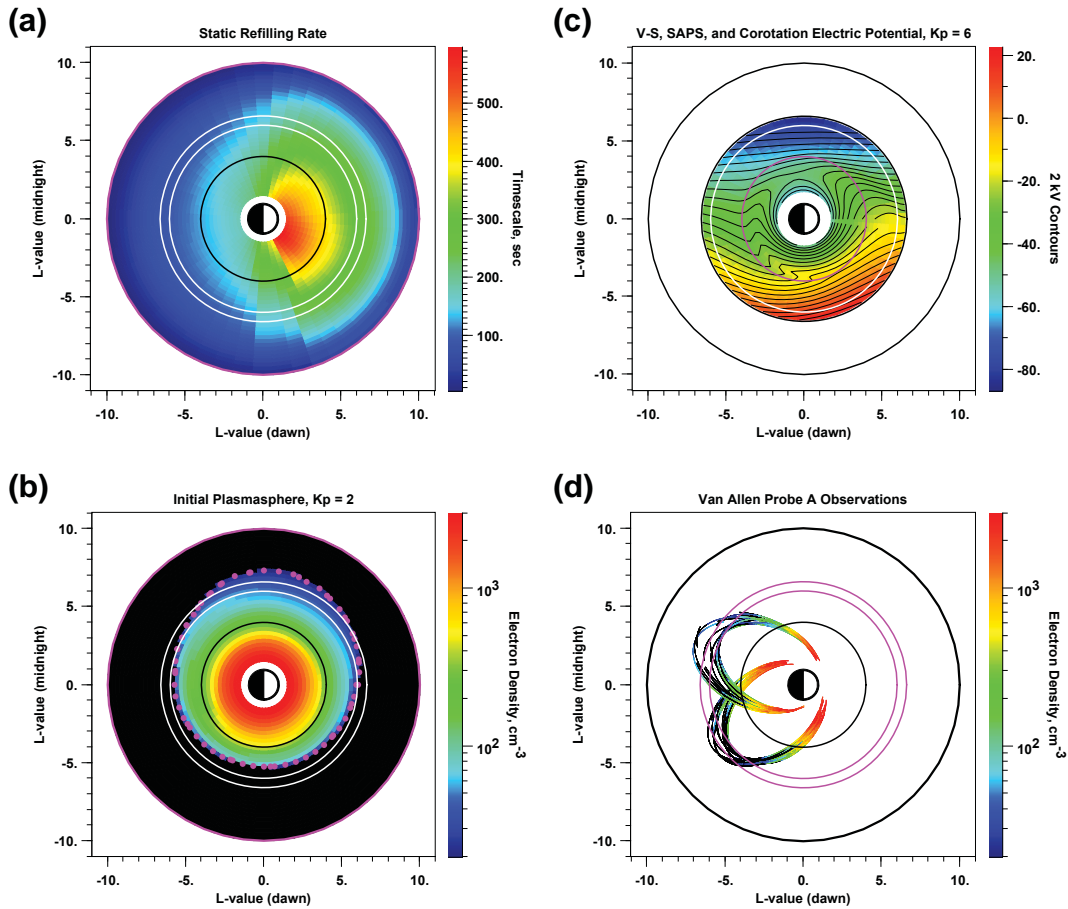
Figure 1: Overview of the equatorial plasmaspheric electron density model, RAM-CPL, used in this study with each plot presented in SM-equatorial coordinates with the sun to the right and earth at center and circles drawn at 4, 6, 6.6, and 10 R_E. The simulations are initialized at a resolution of .25 L by .5 MLT with an extended plasmasphere (b) that is specified by refilling the system to saturation during gemagnetically quite conditions ($K_p < 2$). Empirical models of outgoing particle flux from the ionosphere yield the diurnally dependent rate of refilling (a), which is effective on the dayside. The evolution of plasmaspheric densities driven by $\mathbf{E} \times \mathbf{B}$ convective erosion is described by a Volland-Stern and Subauroral Polarization Stream (SAP) electric potential (c) parameterized by the solar wind and K_p. Simulations are restricted from $1.75 < L < 6.5$ to compare with the limits of Van Allen Probes EMFISIS density observations shown for RBSP-A in panel (d) where 31 May - 5 June, 2013 observations occur in the pre-midnight magnetic local time sector while 15 - 20 January, 2013 observations fall in the post-midnight sector. A low-density threshold (20 cm^{-3}) plasmapause is indicated by the broken magenta line surrounding (b) the initial two-dimensional plasmasphere for illustration.

2.1. Approximating Ionospheric Refilling

RAM-CPL accounts for the ionospheric origin of particles in the plasmasphere contained by Earth's corotating magnetic field. Outward flow along closed magnetic field lines into the refilling plasmasphere is balanced by the transport of plasma. While connected to the ionosphere, a magnetic flux tube element can change in volume and density content. Convective motion, nevertheless, separates this plasma source from the plasmasphere by venting in the content of a flux tube open at the magnetopause of the magnetosphere into interplanetary space (Rasmussen et al., 1993). The predominant ion population in the plasmasphere is composed of H$^+$, which is balanced by an equal number of electrons assuming the quasi-neutrality of the plasma. This plasma species is produced diurnally on the dayside

ionosphere through the charge exchange reaction with oxygen, contributing to a limited upward flux of particles that sustains the plasmasphere. In the simplest scenario, plasma freely exits downward on the nightside back into the ionosphere at an equal rate unless electric fields convect plasma across magnetic field lines during geomagnetic storms (Gordon et al., 1978).

A conservation equation describing the total number of ions due to outflow in a flux tube is obtained by integration of the continuity equation along a field line such that the evolution of average plasma density is given by:

$$\frac{\partial \bar{n}}{\partial t} = \frac{F_N + F_S}{B_i V} \tag{1}$$

assuming no perpendicular transport, where F_N and F_S (positive upward) are the contribution of ionospheric fluxes for the northern and southern hemispheres, respectively. We define a curvilinear magnetic dipole coordinate system (ϕ, θ, L) using the GMXX model, where B_i is the magnetic field at the conjugate ionosphere. Here we have applied the simplification that

$$\bar{n} = \frac{N}{V(L)} \quad \text{and} \quad \bar{n} \cong n_{eq} \tag{2}$$

for the total content N in a volume, V, per unit magnetic flux of a tube of plasma and the equatorial density n_{eq} (at $\theta = \pi/2$) as argued by Rasmussen et al., 1993.

This formulation describes a simple model where the number of ions in a flux tube remains constant, except for the difference in flux accounted for at ionospheric boundaries. An empirical timescale, τ_s, for refilling, can then be obtained by assuming that the approach to equilibrium densities depends on the variation from hemispheric saturation levels, n_N and n_S, according to:

$$\frac{F_N + F_S}{B_i V} = \sum_{s=N,S} \frac{n_s(L, \phi) - n_{eq}(L, \phi)}{\tau_s} \tag{3}$$

Under these approximations, at the time when a flux tube is completely empty ($n_{eq} = 0$) the upward ionospheric fluxes are maximum (no loss) such that the refilling timescale can be written as:

$$\tau_s = \frac{n_s(L, \phi) B_i V}{F_{ls}} \tag{4}$$

In the RAM-CPL scheme, the limiting particle fluxes F_{ls} from the ionosphere are calculated analytically (Richards and Torr, 1985) and further parameterized by empirical models for neutral temperatures and densities (MSIS-86; Hedin, 1987) as well as charged particle temperatures (IRI; Bilitza, 1986). We further take the simplification that τ_s is calculated for a time-independent plasmaspheric density saturation profile (Carpenter and Anderson, 1992):

$$n_{sat} = 10^{(-0.3145L + 3.9043)} \tag{5}$$

and produce a diurnally calculated map from low geomagnetic activity, $\tau_0(L, \phi)$ in **Figure 1a**, which is not averaged like the treatment in DGCPM of Ober et al., 1997. RAM-CPL thus models the evolution of plasmaspheric equatorial density for each magnetic flux tube by specifying a constant rate of refilling:

$$\frac{\partial n_{eq}}{\partial t} = \frac{n_{sat}(L) - n_{eq}(L, \phi)}{\tau_0(L, \phi)} \tag{6}$$

2.2. Specifying the Inner-Magnetospheric Electric Field

During geomagnetically active conditions, a time-variable convection electric field in conjunction with the corotation electric field of Earth will also change the distribution of density in the plasmasphere. The process of erosion begins on the scale of hours as a new mapping of the trajectories of magnetic flux tube of plasma on open (closed) trajectories from the tail (Earth) to closed (open) ones such that refilling (venting can now occur on the scale of days (Nishida, 1966; Chen and Wolf, 1972). As a consequence, the outer boundary of the plasmasphere (the plasmapause) becomes distorted with time and can assume a variety of configurations (e.g. plumes) depending on the history of erosion and refilling. We take a two-component approach validated by Goldstein et al., 2014 for specifying the inner-magnetospheric electric field responsible for erosion. A shielded Volland-Stern electric potential (Volland, 1973;

Stern, 1975) is scaled by the observed solar wind electric field, representing global convection as driven by dayside magnetic reconnection (Goldstein et al., 2005.

In combination, we consider separately the contribution of the subauroral polarization stream (SAPS) phenomenon. SAPS arrises from feedback in a global electrical current circuit between the ring current and high-latitude ionosphere, resulting in a radially narrow, westward flow channel for dusk-to-midnight magnetic local times (MLT) (Burke et al., 1998; Foster and Vo, 2002). When mapped to the magnetospheric equatorial plane, SAPS has the effect of depressing (inwards in L) the stagnation region of the plasmasphere that occurs due to the balance between the convection and corotation electric fields. We choose to parameterize SAPS using the analytical model derived by Goldstein et al., 2005, based on average SAPS properties, that is dependent on the K_p geomagnetic activity index. The model is more effective for moderate to high geomagnetic activity ($K_p > 4$), but is 50% less effective on the post-midnight sector than in the pre-midnight sector.

Figure 2 displays the inputs used by the RAM-CPL model to specify the inner-magnetospheric electric model E_{IM} for the post-midnight event on 15 - 20 January, 2013. The driving solar wind electric field in **Figure 1a** is calculated as $E_{SW} = V_{SW}B_{Z,IMF}$ based on measurements at a 5-minute cadence taken in GSE coordinates by OMNI solar wind monitors. For southward turning of the interplanetary magnetic field (IMF, negative E_{SW} values), which would incite dayside magnetic reconnection at the magnetopause and sunward convection within the magnetosphere, we assume that the inner magnetospheric electric field is characterized by $E_{IM} = 0.2E_{SW}$ where we impose $E_{IM} \geq 0.5$ mV/m during northward IMF following Goldstein et al., 2014 in the middle panel. The final plot of **Figure 2** displays the 5-minute effective K_p as determined from the now defunct DMSP auroral boundary index.
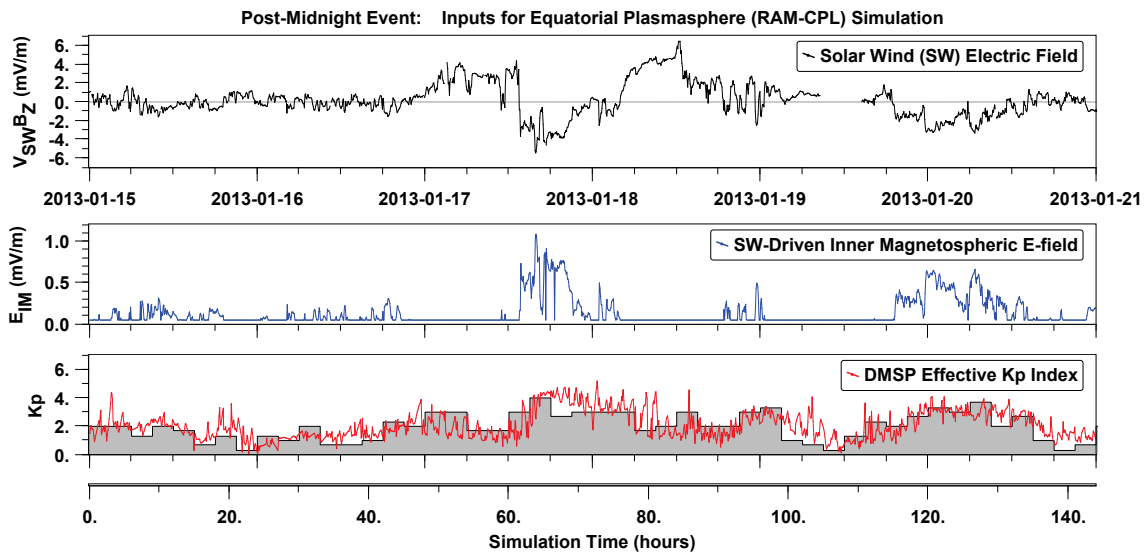
Figure 2: Geomagnetic conditions for the post-midnight event on 15 January, 2013 used to as inputs to drive **E x B** erosion in the RAM-CPL simulations considered here. The solar wind electric field $V_{SW}B_{Z,IMF}R$ (from OMNI data) is scaled as described in the text to produce an inner magnetospheric electric field E_{IM} to parameterize a Volland-Stern model for convection. Asymmetric and enhanced flows are included by the addition of an analytical SAPS electric field component whose strength varies by the effective K_p index derived from DMSP with the 3-hour K_p geomagnetic activity index shown for reference.

3. Plasmasphere Dynamics on 15-20 January, 2013

Simulated equatorial plasmaspheric densities are produced at the 5-minute cadence of the input parameters shown in **Figure 2**. Proceeding from the 15 of January, 2013 onwards over the next few days we see the formation of a narrowly extended plasmapause suggestive of a plume of plasma whose evolution is expressed in **Figure 3**. This geomagnetic event, observed by Van Allen Probes A in the post-midnight magnetic local time sector is moderate in strength yet still compresses part of the plasmasphere within $L = 4$ as seen 75 hours into the simulation by the indicated 20 cm^{-3} low-density threshold plasmapause. We find good agreement with the behavior of the plasmasphere for this same time interval as that reported for a plasmapause test particle model in Goldstein et al., 2014. This work, however, expands the previous investigation by also comparing simulated density values of a virtual satellite pass through the RAM-CPL produced equatorial plasmasphere and the actual density measurements reported by EMFISIS. **Figure 4** highlights from 12:00 UT on the 15th to 00:00 UT on 18th of January, 2013. RAM-CPL shows less than an order of magnitude difference fidelity with EMFISIS densities, lending support that it is a useful tool to study the plasmasphere. Although the actual identified plasmapause locations do not always correspond to steepest density gradients in the observations or simulations, there is still a close proximity between the two that we will investigate further in this paper. It is worth noting that regions in which EMFISIS density has been extracted from continuum radiation at the low-frequency cutoff of the plasma frequency provide only an upper limit to the expected electron density (Kurth et al., 2015). Thus, the strictly defined low-density (20 cm^{-3}) threshold of the plasmapause located at 21:00 UT on 17 January, 2013 constitute perhaps a misidentification.
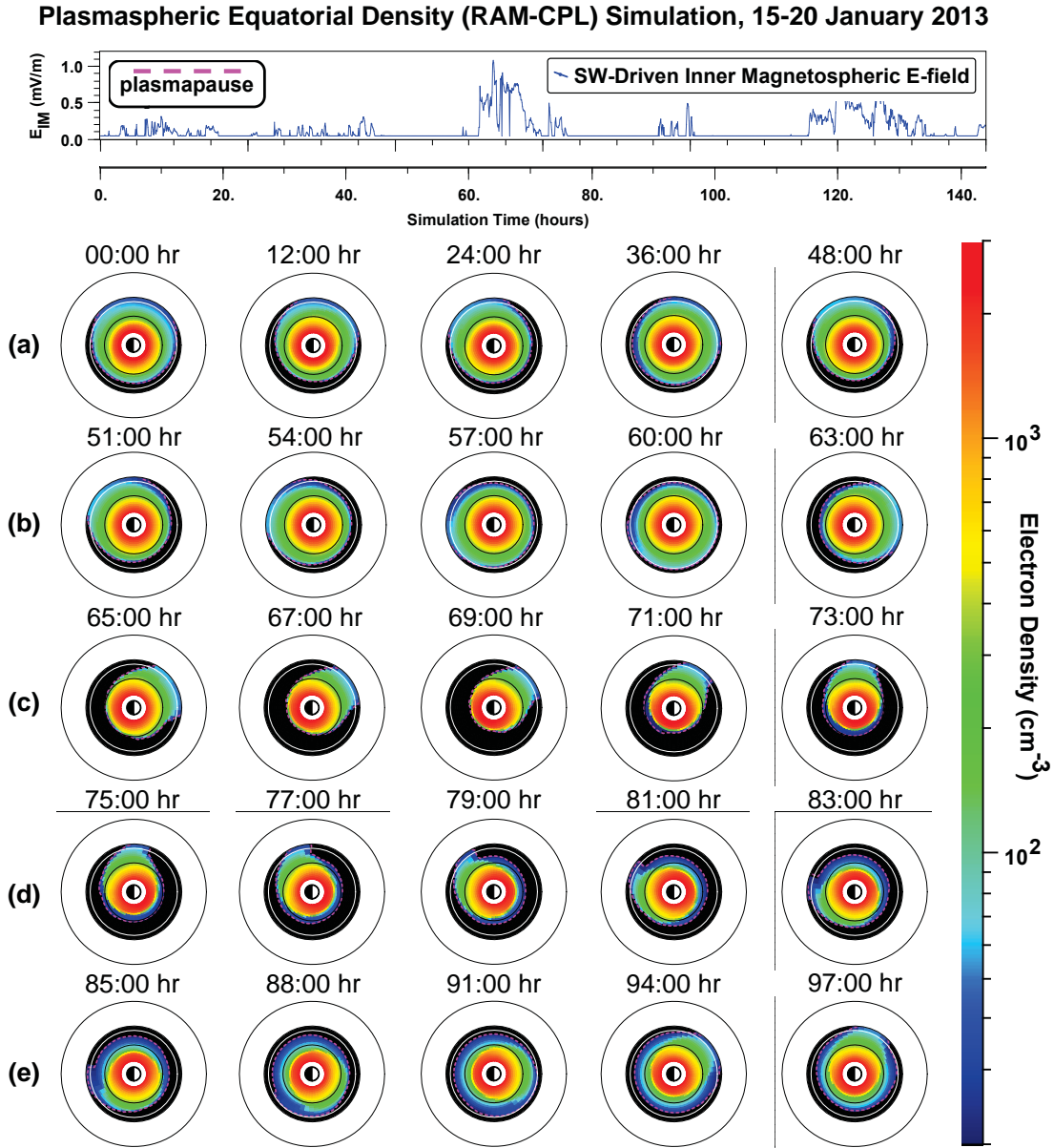
Figure 3: Summary of RAM-CPL simulation for the post-midnight event on 15 - 20 January, 2013. Each dial plot is presented in the SM-coordinate equatorial system with the sun at right and the earth at center. Circles drawn provide an approximate indication of radial distance for 4, 6, 6.6, and 10 L. Each timestamp above the output dial gives the number of hours since the initialization of the equatorial plasmaspheric density model on 00:00 UT 15 January, 2013. The hours during storm onset between 63:00 and 97:00 as indicated by the panel of the solar wind driven inner magnetospheric electric field parameterizing a Volland-Stern convection potential show the formation of a narrow extension of plasma on the dayside that subsequently corotates with the main body of the plasmasphere as the level of geomagnetic activity subsides.

Figure 4: Highlight of EMFISIS RBSP-A *in situ* density measurements (black) compared to virtual observations (green) through the equatorial plasmaspheric density model RAM-CPL from 12:00 UT on 15th to 00:00 UT on the 18th of January, 2013. Light vertical bars correspond to actual plasmapause crossings of the RBSP-A spacecraft as determined by a low-density (20 cm^3) threshold. As described in the text, a region in which continuum radiation was used to identify the upper limit of the local plasma density is labeled.

4. Determining Plasmapause Encounters

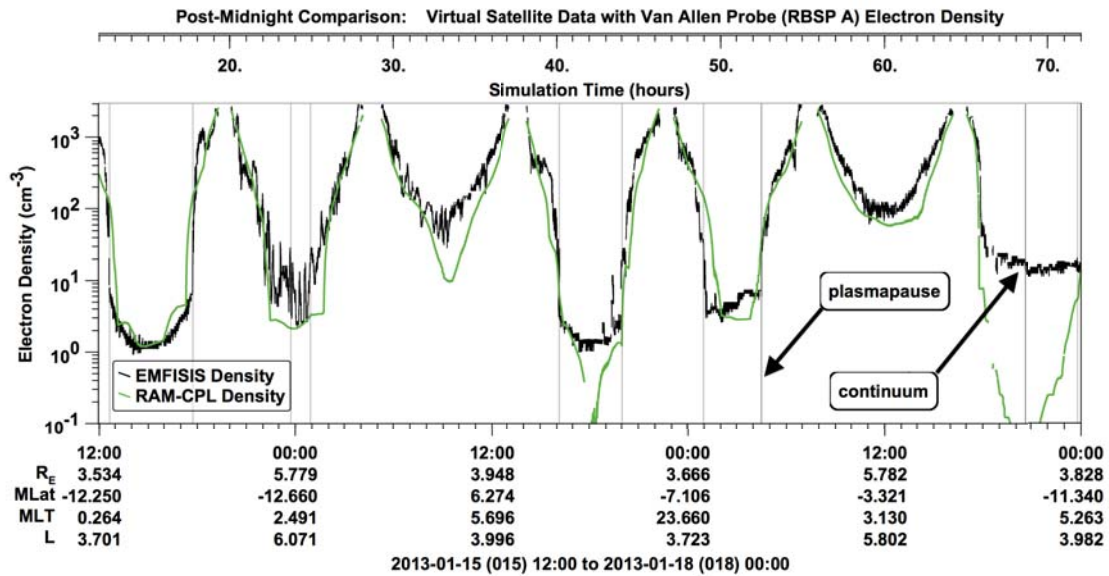We further investigate the correspondence between actual plasmapause crossings from EMFISIS measurements and virtual plasmapause crossings from the RAM-CPL simulation. For this post-midnight event on 15 - 20 January, 2013 we find a mean agreement between the model and observations of $\Delta L_{AVG} = 0.52 \pm 0.15 R_E$ as shown in **Figure 5** and **Figure 6a**. The case in which continuum radiation was used to provide a density measurement does affect this analysis slightly, but only 1 case out of the 28 total palsmapause crossings had this caveat. Moreover, the model plasmapause locations only contained 2 false positives, demonstrating the validity of RAM-CPL. When this comparison is expressed in terms of the driving inner magnetospheric electric field conditions we see that the largest range of errors is correlated with quiet levels of geomagnetic activity at the defined $E_{IM} \geq 0.5$ mV/m. The pre-midnight 31 May - 5 June, 2013 event was deliberately excluded from this paper because this effect was more pronounced for that storm and inhibited a sufficient analysis. But, **Figure 6b** does imply, at least super superficially, that the specified level of viscous solar wind interaction with the magnetosphere during northward turning of the interplanetary magnetic field does regulate to some degree the RAM-CPL modeled extent of the plasmasphere.
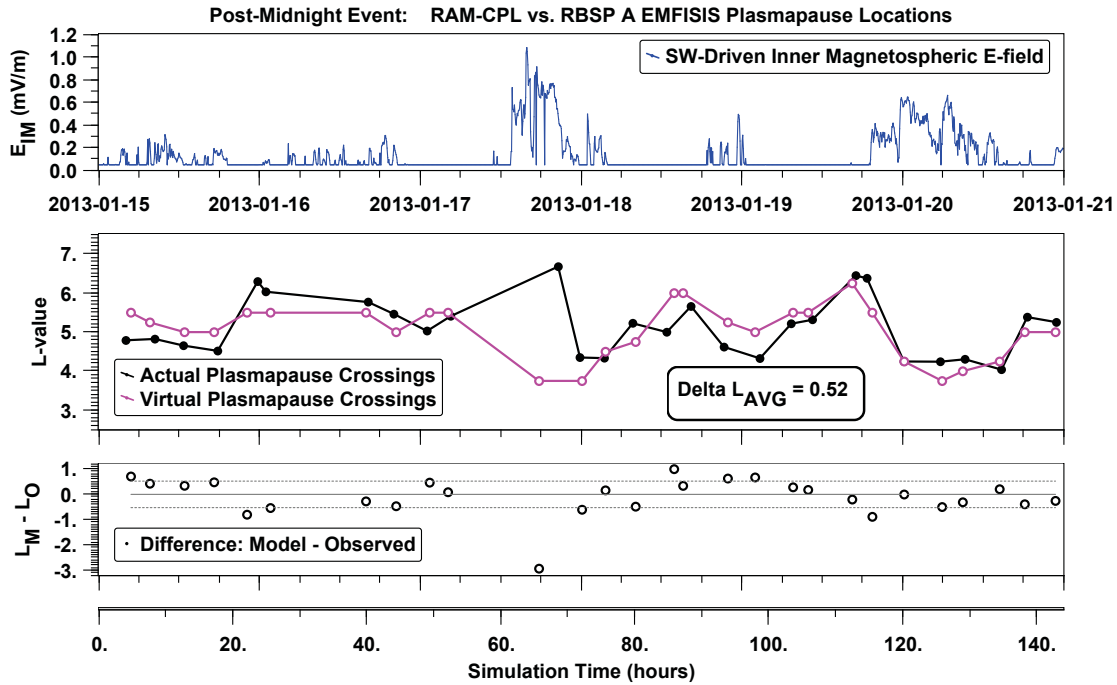
Figure 5: Simulated plasmapause locations from RAM-CPL vs RBSP-A EMFISIS density identifications on 15 - 20 January, 2013. The inner magnetospheric electric field (top panel) controls the extent of the plasmasphere in these simulations and also, to some degree, corresponds to the geomagnetic activity level affecting the actual plasmasphere. Both the actual crossings (black line) and virtual crossings (magenta line) show the relationship between inward plasmapause movement and convection (increased E_{IM}). The mean difference between both actual and virtual detections is $\Delta L_{AVG} = 0.52 \pm 0.15 R_E$ as presented in the bottom panel.
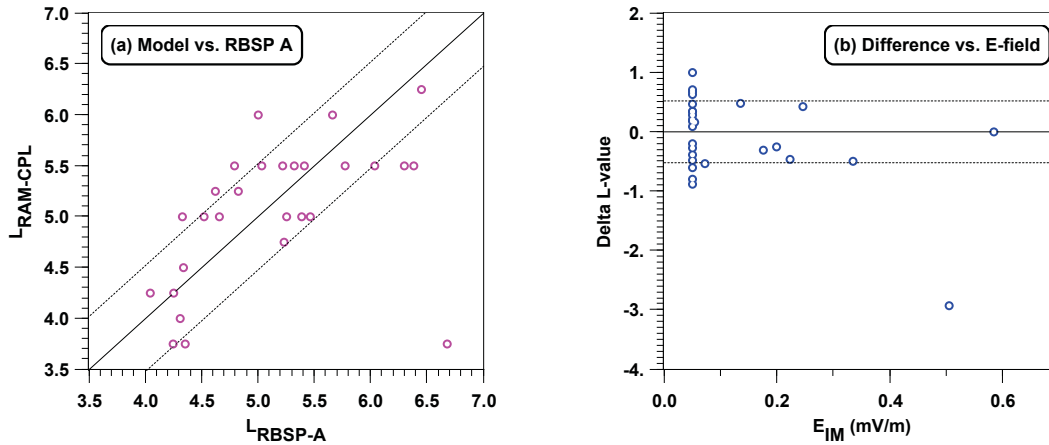

Figure 6: Simulated plasmapause locations versus actual plasmapause locations on 15 - 20 January, 2013 with respect to their correspondence (a) and correlation (b) with the driving inner magnetospheric electric field, E_{IM}. Greater disagreement was found during quieter conditions.

5. Summary and Conclusions

This paper demonstrates the applicability of a two-component electric field model driving convective erosion in the plasmasphere during 15 - 20 January, 2013. A combined Volland-Stern and SAPS electric potential, driven separately by the solar wind and K_p index respectively, produced favorable agreement between the equatorial plasmaspheric density simulations and RBSP-A EMFISIS observations. The virtual satellite pass encountered electron densities within an order of magnitude of RBSP-A measurements and all 28 plasmapause crossings during the post-midnight event with only 2 false positives. This reliability is further bolstered by valid identification of the plasmapause, as defined by a low-density threshold of 20 cm^{-3}, for a mean model-observation difference of $\Delta L_{AVG} = 0.52 \pm 0.15 R_E$. It is suggested that the noted correlation between greater disagreement and quieter geomagnetic conditions should be further inspected with other case studies. A detailed comparison with the pre-midnight 31 May - 5 June, 3013 event will help to identify this source of error as a physical or analytical consequence.

References

Bilitza, D. (1986). International Reference Ionosphere: recent developments. Radio Sci 21, 343, 1986.

Borovsky, J.E., D.T Welling, M.F. Thomsen, M.H. Denton (2014). Long-lived plasmaspheric drainage plumes: Where does the plasma come from? J Geophys Res 119, 6496-6520.

Burke, W.J., et al. (1998). Electrodynamics of the inner magnetosphere observed in the dusk sector by CRRES and DMSP during the magnetic storm of June 4-6, 1991. J of Geophys Res 105, 18, 391.

Carpenter, D.L. (1963). Whistler evidence of a "Knee" in the magnetospheric ionization density profile. J of Geophys Res 68, 1675 - 1682.

Carpenter, D.L. and Anderson, R.R. (1992). An ISEE/Whistler model of equatorial electron density in the magnetosphere. J of Geophys Res 97, A2, 1097-1108.

Carpenter, D.L. and Lemaire, J. (1997) Erosion and recovery of the plasmasphere in the plasmapause region. Space Sci Rev 80, 153-179.

Chappell, Cr., Harris, K.K., Sharp, G.W. (1970). The morphology of the bulge region of the plasmasphere. J of Geophys Res 75, 19, 3848-3861.

Chen, A.J., and Wolf, R.A. (1971). Effects on the plasmasphere of a time-varying convection electric field. Planet Space Sci 20, 483-509.

Darrouzet, F. et al. (2009). Plasmaspheric density structures and dynamics: Properties observed by the CLUSTER and IMAGE missions. Space Sci Rev 14, 55-106.

Foster, J.C., and Burke, W.J. (2002). SAPS: A new categorization for sub-auroral electric fields, Eos Trans AGU 83, 36, 393.

Foster, J.C., and Vo, H.B. (2002). Average characteristics and activity dependence of the sub auroral polarization stream. J of Geophys Res 107. A12), 1475.

Fok, M.C., Kozyra, J.U., Nagy, A.F., Cravens, T.E. (1991). Lifetime of ring current particles due to Coulomb collisions in the plasmasphere. J of Geophys Res 96, 7861-7867.

Ganguli, G., Reynold, M.A., Liemohn, M.W., 2000. The plasmasphere and advances in plasmaspheric research. J of Atmos and Solar-Terrestrial Physics 62, 1647-1657.

Goldstein, J. Burch, J.L., and Sandel, B.R. (2005). Magnetospheric model of sub auroral polarization stream. J of Geophys Res 110, A09222.

Goldstein, J., De Pascuale, S., Kletzing, C., Kurth, W., Genestreti, K.J., Skoug, R.M., Larsen, B.A., Kistler, L.M., Mouikis, C., Spence, H. (2014). Simulation of Van Allen Probes plasmapause encounters. J of Geophys Res, doi:10.1029/2014JA020252, in press.

Gordon, C.W., Canuto, V., and Axford, W.I. (1978). The Earth, 1: The Upper Atmosphere, Ionosphere, and Magnetosphere. Gordon and Breach Science Publishers. 40.

Hedin, A.E. (1987). MSIS-86 thermospheric model. J Geophys Res 92, 4649.

Jordanova, V.K., Kistler, L.M., Kozyra, J.U., Khazanov, G.V., Nagy, A.F. (1996). Collisional losses of ring current ions. J of Geophys Res 101, A1, 111-126.

Jordanova, V.K. and Miyoshi, Y. (2005). Relativistic model of ring current and radiation belt ions and electrons: initial results. Geophys Res Lett 32.

Jordanova, V.K., Miyoshi, Y.S., Zaharia, S., Thomsen, M.F., Reeves, G.D., Evans, D.S., Mouikis, C.G., and Fennell, J.F. (2006). Kinetic simulations of ring current evolution during the Geospace Environment Modeling challenge events. J of Geophys Res 111, A11S10.

Jordanova, V.K., Thorn, R.M., Miyoshi, Y. (2010a). Excitation of whistler-mode chorus from global ring current simulations. J Geophys Res 115.

Jordanova, V.K., Zaharia, S., Welling, D.T. (2010b) Comparative study of ring current development using empirical dipolar, and self-consistent magnetic field simulations. J Geophys Res 115 (2010b).

Kletzing, C.A. et al. (2013). The Electric and Magnetic Field Instrument Suite and Integrated Science (EMFISIS) on RBSP. Space Sci Rev 179, 127-181.

Kurth, W.S. et al. (2015). Electron densities inferred from plasma wave spectra obtained by the Waves instrument on Van Allen Probes. J Geophys Res 120, 904-914.

Liemohn, M.W., Ridley, A.J., Gallagher, D.L., Ober, D.M., and Kozyra, J.U. (2004). Dependence of plasmaspheric morphology on the electric field description during the recovery phase of the 17 April 2002 magnetic storm. J Geophys Res 109, A03209.

Liemohn, et al. (2005). Parametric analysis of nightside conductance effects on inner magnetospheric dynamics for the 17 April 2002 storm. J Geophys Res 110, A12S22.

Liemohn, et al. (2006). Analyzing electric field morphology through data-model comparisons of the GEM Storm Assessment Challenge events. J Geophys Res 111, A11S11.

Lemaire, J.F., and Gringauz, K.I. (1998). The Earth's Plasmasphere. Cambridge University Press, New York.

Lyons, L.R., Thorn, R.M., Kennel, C.F. (1972). Pitch-angle diffusion of radiation belt electrons within the plasmasphere. J Geophys Res 77, 19, 3455.

Maynard, N.C., and Chen, A.J. (1975). Isolated cold plasma regions: Observations and their relation to possible production mechanisms. J of Geophys Res 80, 1009.

Moldwin, M.B. et al. (2002). A new model of the location of the plasmapause: CRRES results. J Geophys Res 107, A11, 1339-1348.

Nishida, A. (1966). Formation of plasmapause by the combined action of magnetospheric convection and plasma escape from the tail. J of Geophys Res 71, 23, 5669-5679.

Ni, B., et al. (2013). Resonant scattering and resultant pitch angle evolution of relativistic electrons by plasmaspheric hiss. J Geophys Res 118, 7740-7751.

Ober, D.M., et al. (1997). Formation of density troughs embedded in the outer plasmasphere by sub auroral ion drift events. J Geophys Res 102, A7, 14595-14602.

O'Brien, T.P. and Moldwin, M.B. (2003). Empirical plasmapause models from magnetic indices. Geophys Res Letters 30, 4, 1152-1156

Rasmussen, C.E., Guiter, S.M., and Thomas, S.G. (1993) A two-dimensional model of the plasmasphere: refilling time constants. Planet Space Sci 41, 1, 35-43.

Richards, P.G., and Torr, D.G. (1985). Seasonal, Diurnal, and Solar Cyclical Variations of the Limiting H^+ Flux in the Earth's Topside Ionosphere. J of Geopphys Res 90, A6, 5216-5268

Singh, A.K., Singh, R.P., Siingh, D. (2011). State studies of Earth's plasmasphere: A review. Planet Space Sci 59, 810-834.

Stern, D.P. (1975). The motion of a proton in the equatorial magnetosphere. J of Geophys Res 80, 595.

Thaller, S.A. et al. (2015). Van Allen Probes investigation of the large-scale dusk ward electric field and its role in ring current formation and plasmasphere erosion in the 1 June 2013 storm. J of Geophys Res 120, 4531-4543.

Thorne, R.M. et al. (2013). Rapid local acceleration of relativistic radiation-belt electrons by magnetospheric chorus. Nature 504, 411-414.

Volland, H. (1973). A semi empirical model of large-scale magnetospheric electric fields. J of Geophys Res 78, 171.

Walsh, B.M., et al. (2014). Simultaneous ground- and space-based observations of the plasmaspheric plume and reconnection. Science 343, 6175, 1122-1125.

Weimer, D.R. (2005). Improved ionospheric electrodynamic models and application to calculating Joule heating rates. J of Geophys Res 110, A05306.

Wygant, J.R., et al. (2013). The Electric Field and Waves Instruments on the Radiation Belt Storm Probes Mission. Space Sci Rev 179, 183-220.

Ion and Electron Heating by Whistler Turbulence: Parametric Studies via Particle-In-Cell Simulation

R. Scott Hughes

University of Southern California, Los Angeles, CA 90089

S. Peter Gary

Space Science Institute, Boulder, CO 80301

Joseph Wang

University of Southern California, Los Angeles, CA 90089

Abstract

Wave-particle interactions are studied in a 3D Particle-In-Cell (PIC) model of a homogeneous, collisionless magnetized plasma subjected to an initially narrowband isotropic spectrum of relatively long wavelength whistler fluctuations. A series of simulations is carried out in order to determine the manner in which the heating rate of each population scales with initial fluctuating magnetic energy density ε_o. In each simulation the plasma β is held fixed at $\beta_e=\beta_i= 0.25$ within a simulation domain of length $L\omega_{pi}/c = 5.12$, where ω_{pi} denotes the ion plasma frequency, and ε_o is varied as $\varepsilon_o = 0.01, 0.025, 0.05, 0.1, 0.25$. As the initial spectrum undergoes a forward cascade to shorter wavelengths with a preference to propagate at highly oblique angles relative to the background magnetic field, the fluctuations resonate with both the electron and ion populations resulting in heating of each respective species. While the electrons are heated primarily along the mean magnetic field lines, the ions experience enhanced heating primarily in the perpendicular direction. These temperature anisotropies are amplified for each species with increasing ε_o. Furthermore, the spectral anisotropy factor of the cascaded magnetic fluctuation energy grows larger with increasing initial amplitude signifying an increasing preference for propagation across the background magnetic field. The primary result of this study is given by the scaling of maximum particle heating rate as a function of ε_o. It is shown that the electron heating rate maintains a proportional relationship, while the ion heating rate increases according to a power law ε_o^{σ} with $\sigma>1$. This suggests that ion heating may become the primary mode of whistler turbulence dissipation at sufficiently high fluctuation amplitudes.

Keywords: Solar Wind, Turbulence, Whistler, Heating, Ion Heating

1. Introduction

Solar wind turbulence near 1 AU is observed as large-amplitude, broadband energy spectra of magnetic field fluctuations with a dependence on the observed frequency f of $f^{-5/3}$ and the inferred wavenumber (by Taylor's frozen in flow hypothesis [*Taylor*, 1938]) $k^{-5/3}$ over more than three orders of magnitude variation [*Alexandrova et al.*, 2013]. This regime, termed the *inertial range*, is understood as a nonlinear forward cascade of fluctuations from very long wavelength sources down to a spectral break near 0.2 Hz $< f < 0.5$ Hz which corresponds approximately to either $kc/\omega_{pp} \sim 1$ or $k\rho_p \sim 1$ [1] [*Chen et al.*, 2014]. These two wavenumbers, which are equivalent at $\beta_p = 2$, are characteristic scale-lengths of the proton population in a proton-electron plasma.

---

[1] Here ω_{pj} represents the jth species plasma frequency, ρ_j represents the jth species thermal gyroradius. $j = i$, p and e denotes ions, protons and electrons respectively.

At higher frequencies and shorter wavelengths solar wind magnetic spectra are observed to have steeper wavenumber dependences, following a power law $\propto k^{-\alpha}$ with $\alpha > 2$ [*Alexandrova et al.*, 2013], and strong wavevector anisotropies with $k_\perp >> k_\parallel$ [2] [*Sahraoui et al.*, 2009, 2010, 2013; *Narita et al.*, 2011]. A number of solar wind observations indicate that turbulent fluctuations in the wavenumber range $1 < kc/\omega_{pp} < 10$ consist primarily of incompressible kinetic Alfvén waves [*Sahraoui et al.*, 2009, 2010; *Salem et al.*, 2012; *Podesta*, 2013; *Kiyani et al.*, 2013; *Chen et al.*, 2013; *Roberts et al.* 2013]. This short-wavelength regime is frequently called the *dissipation range* under the assumption that the spectral break corresponds to the onset of dissipation as fluctuation wavelengths become shorter. A minority view is that this regime should be called the *dispersion range* [*Stawicki et al.*, 2001] because the inertial range break approximately corresponds to the onset of dispersion in magnetosonic-whistler waves. However, observational evidence for the presence of magnetosonic-whistler turbulence at such short wavelengths is weaker [*Gary and Smith*, 2009; *Narita et al.*, 2011; *Perschke et al.*, 2013, 2014]. As the relative roles of dissipation and dispersion are not yet well established in this regime, the name for this domain adopted here is the *kinetic range*.

At even shorter, electron scales corresponding to $kc/\omega_{pe} \sim 1$ and $k\rho_e \sim 1$, magnetic fluctuation spectra observed in the solar wind show still steeper wavenumber dependences. At and beyond these scales, spectra can be fit with either a power-law dependence with $\alpha > 3$ [*Sahraoui et al.*, 2009, 2010, 2013] or an even more rapid exponential decrease [*Alexandrova et al.*, 2009, 2012, 2013]. An exponential decay in the power spectrum is what would be expected at dissipation scales if parallels are drawn with neutral fluid turbulence [*Frisch*, 1995].

Explaining kinetic range plasma turbulence requires understanding not only nonlinear processes which drive the field fluctuation cascade, but also linear dispersion (that is, the wavevector dependence of the fluctuation mode frequency) and both linear and nonlinear dissipation processes at short wavelengths. The quasilinear premise [*Klein et al.,* 2012] states that some properties of magnetized plasma turbulence can be understood by modeling that turbulence as a collection of randomly phased linear waves. Computer simulations provide substantial evidence that this premise is valid at short wavelengths [*Saito et al.*, 2008; *Howes et al.*, 2011; *Chang et al.* 2013]; assuming its validity, the approach taken here is to use linear theory to supply the initial dispersion properties of whistler range modes, and utilize fully nonlinear particle-in-cell (PIC) simulations to address the fundamentally nonlinear properties of turbulent cascade and dissipation.

2. Background

Recent PIC studies of the forward cascade of whistler turbulence in collisionless, homogeneous, magnetized electron-ion plasmas include 2D PIC studies with $\mathbf{B}_0$ in the computational plane [*Gary et al.*, 2008; *Saito et al.*, 2008, 2010; *Saito and Gary*, 2012] and fully 3D PIC studies [*Chang et al.*, 2011, 2013, 2014, 2015; *Gary et al.*, 2012]. In each of these works an ensemble of relatively long-wavelength, approximately isotropic, relatively narrowband whistler fluctuations are imposed at $t=0$, and the simulations follow the subsequent temporal evolution of the fluctuating fields and particles. For all parameter values studied, the whistler fluctuations undergo a forward cascade to a broadband turbulent spectrum extending to shorter wavelengths with wavevector anisotropies of the type $k_\perp >> k_\parallel$. These studies addressed only electron heating, demonstrating

1. Electron heating is substantially stronger in $T_{e\parallel}$ than in $T_{e\perp}$.
2. If the initial electron temperature is $\beta_e = 0.10$, the late-time electron heating increases with increasing initial fluctuating magnetic field energy ε_o [*Gary et al.*, 2012].
3. Over $0.10 < \beta_e < 1.0$ the late-time heated electrons exhibit bi-Maxwellian-like velocity distributions, but at $\beta_e = 0.01$ turbulent heating produces extended tails in the suprathermal parts of the electron velocity distribution [*Chang et al.*, 2013].
4. If the initial fluctuation amplitudes and the initial electron temperature are fixed so that β_e is varied due to changes in ω_{pe}/Ω_e (here Ω_e denotes the electron cyclotron frequency), the total late-time electron heating rate normalized to Ω_e increases with increasing β_e. Furthermore the late-time electron temperature anisotropy $T_{e\parallel}/T_{e\perp}$ decreases with increasing β_e [*Chang et al.*, 2013].

More recent studies have begun to address how whistler turbulence may heat ions as well as electrons. *Saito and Nariyuki* [2014] used 2D PIC simulations with $\mathbf{B}_0$ in the simulation plane to show that forward cascading whistler fluctuations could heat ions in directions perpendicular to the background magnetic field. *Hughes et al.* [2014] carried out 3D PIC simulations at $\beta_e = 0.05$ with computational domains large enough to accommodate both magnetosonic and whistler fluctuations. This study showed

---

[2] The subscripts $\perp$ and $\parallel$ denote directions relative to the background magnetic field $\mathbf{B}_0$.

1. Ion heating is stronger in $T_{i\perp}$ than in $T_{i\parallel}$.
2. Increasing the simulation domain size (allowing for larger initial fluctuation wavelengths) yields reduced electron heating.
3. Increasing the simulation domain size yields enhanced ion heating.
4. The late-time heated ions exhibit bi-Maxwellian-like velocity distributions.

Several different calculations have been used to examine plasma species heating by fluctuations in turbulent collisionless plasmas. *Markovskii et al.* [2010] and *Markovskii and Vasquez* [2010] carried out 2D hybrid simulations (PIC ions, fluid electrons) of magnetosonic turbulence in collisionless plasmas with $\mathbf{B}_0$ in the simulation plane and $\beta_i = 0.02$ in a simulation domain of size $L_{\parallel}\omega_{pi}/c = L_{\perp}\omega_{pi}/c = 30\pi$ with minimum wavenumber $kc/\omega_{pi} \cong 0.067$. The forward cascade developed the same $k_{\perp} \gg k_{\parallel}$ wavevector anisotropy as in the whistler turbulence PIC simulations mentioned above. For runs with initial spectra consisting of fluctuations propagating parallel but not antiparallel to $\mathbf{B}_0$ the ion heating is preferentially perpendicular to the background magnetic field. For initially isotropic spectra the ion heating changes to be predominantly in the parallel/antiparallel directions, but for initial spectra which are bidirectional but only quasi-perpendicular to $\mathbf{B}_0$ the ion heating reverts to $T_{\perp} > T_{\parallel}$.

Howes [2010] used a cascade model for Alfvénic turbulence to calculate the ratio of ion and electron heating rates, Q_i/Q_e, using damping rates derived from linear gyrokinetic dispersion theory. For typical solar wind parameters, the heating rates are weak functions of T_e/T_i. If $\beta_i = \beta_e < 1$, only the electrons are Landau-resonant with Alfvén waves, and electron heating dominates; at $\beta_i = \beta_e \cong 3$ the two heating rates are approximately equal, and as β further increases, ions become Landau resonant and that species gains the stronger heating. *Wu et al.* [2013] used forward cascading Alfvénic turbulence in a 2D PIC model with $\mathbf{B}_0$ oblique to the simulation plane in a $\beta_i = \beta_e = 0.1$ plasma to show that at relatively weak turbulence amplitudes the electrons are preferentially heated, whereas at larger amplitudes ion heating becomes more important.

The intention of the work presented here is to add to the findings of *Hughes et al.* [2014] by studying the relative rates of ion and electron heating in a collisionless magnetized plasma subjected to whistler turbulence through the use of large-scale three-dimensional PIC simulations. The focus of this study is to characterize the heating rate of each species as a function of the initial magnetic fluctuation amplitude while the system is constrained to an initial β appropriate to typical solar wind conditions near 1 AU.

3. Methodology

3.1. Simulations

The present study is carried out using a three-dimensional electromagnetic particle-in-cell code 3D-EMPIC, as described in *Wang et al.* [1995] which has been further modified to run at high parallel efficiency on distributed memory architectures. By this algorithm, ions and electrons are treated as individual entities and their six-dimensional phase space trajectories are tracked through the self consistent solution to Maxwell's equations along with Newton's equation of motion. The initial conditions consist of a uniform background magnetic field and each particle species is loaded into the domain with a homogeneous spatial distribution and a Maxwellian velocity distribution. Electromagnetic fluctuations having properties consistent with those of whistler modes are then loaded into the domain. The component relative magnitudes of these modes are derived from the numerical solution to the electromagnetic kinetic linear dispersion relation [*Gary*, 1993]. In total, 150 normal mode fluctuations possessing relatively long wavelengths and random phases are loaded into the domain at various directions of propagation. These modes form an initially long wavelength isotropic wavevector spectrum.

In order to improve the consistency between the initial electromagnetic fluctuations and the initial phase space configuration of the particles, each particle distribution is formed from the superposition of a thermal Maxwellian distribution and a perturbation velocity distribution associated with the field fluctuations. The latter distribution obtains by perturbing the velocity components of each individual particle according to the fluctuating field magnitudes at the location of that particle. The perturbation velocity component amplitudes for each whistler mode for each species are derived from the numerical solution to the electromagnetic kinetic linear dispersion relation, and the phases are calculated via phase relations with the fluctuating electric fields.

The simulations described here consist of a three dimensional Cartesian domain of shape $L_x = L_y = L_z = L$ with length $L = 102.4 \ c/\omega_{pe} = 5.12 \ c/\omega_{pi}$. The cell spacing is equal to the Debye length, λ_D, leading to a total of 1024^3 cells. The electron thermal velocity is set as $v_{te}/c = 0.1$ and initially $T_e = T_i$. The mass ratio was chosen as $m_i/m_e = 400$ in order to accelerate the ion dynamics and reduce the required simulation run time. Here it is assumed that qualitatively the physics is unaffected by this choice of mass ratio as long as $m_i \gg m_e$. In *Hughes et al.* [2014] the plasma β was set at $\beta_e = 0.05$. This value is relatively low for realistic conditions in the solar wind near 1 AU

(typically β ∼ 1) but allowed for a very clear depiction of ion heating. The current simulations move toward more realistic conditions with a value $\beta_e = 0.25$. The single parameter allowed to vary in this study was the initial dimensionless magnetic fluctuation energy density, defined as

$$\varepsilon_0 = \sum_{\mathbf{k}} \delta |\boldsymbol{B}_{\mathbf{k}}|^2 / B_0^2 \qquad (1)$$

where $\delta|\boldsymbol{B}_{\mathbf{k}}|$ is the magnetic fluctuation amplitude of the mode with wavevector $\mathbf{k}$ (each initial mode is given equal amplitude) and B_0 is the background magnetic field strength. Five simulations were run with values $\varepsilon_o = 0.01$, 0.025, 0.05, 0.1, 0.25. A point was made to chose values which satisfy the condition $\varepsilon_o \leq \beta$ as in the solar wind the thermal pressure is typically greater than the fluctuation energy density on kinetic scales.

3.2. Numerical Validation

The particle-in-cell algorithm can introduce nonphysical heating, in part resulting from the use of a discretized mesh but also due to a limited number of particles per cell. Due to computational memory constraints 32 super-particles of each species (i.e. 32 ions, 32 electrons) per cell were used in this study. In order to quantify the effects of this choice of particle count and the ensuing "thermal" noise, a run was carried out with no initial fluctuations in the system. All other parameters are the same as those described above. Under these conditions the simulated plasma should remain in an equilibrium condition and no heating should occur. Figure 1 displays the energy density profiles with time for this test run. While zero energy exchange is not achieved the effect of the numerical techniques employed is actually to slightly and gradually cool the particles. The ion cooling is proportional to the electron cooling by the square root of their mass ratio. The source of this cooling can be attributed to the use of a Gaussian filter which is applied to the calculated current density at each time step in order to counteract numerical heating. Figure 1 reveals that the Gaussian filter over-corrects, and the particles are slightly cooled. In any event, the level to which the particles are cooled is, in most cases, well below that of the level to which they are heated when initial fluctuations are present. For example, in comparing with the case of $\varepsilon_0 = 0.05$ from figure 3, the electrons are heated to 10 times that by which they are cooled in this test case. Thus, such effects are justifiably neglected in the following results.
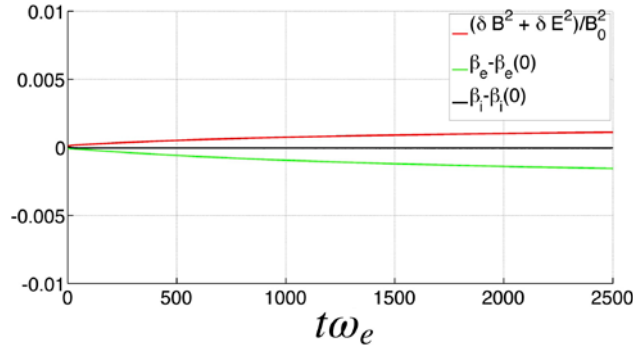

Figure 1: Results of a run with no initial fluctuation energy, quantifying the numerical effects on particle heating. The electromagnetic (red), electron (green) and ion (black) energy densities normalized by the background magnetic field energy density are shown.

3.3. Diagnostics

The primary plasma property under investigation here is the temperature of each species, along with the rate of change in temperature. Previous studies (e.g. *Hughes et al.,* 2014) calculated this property by finding the variance in velocity of each species over the entire domain. This provided a calculation of thermal velocity from which the temperature in each direction can be obtained according to $k_B T_j = m_j v_{tj}^2$. Calculating the temperature in this way resulted in rapid ion heating followed by large oscillations in the ion temperature time history (see figure 2). The problem was that the measured value was composed of two components: the energy associated with irreversible heating of the population, i.e. the temperature, along with a component attributed to reversible oscillatory motions induced through interactions with the field fluctuations. The latter component is associated with spatial structure and should not be accounted for in the calculation of temperature.

To this end, an improved temperature diagnostic was developed for this investigation. The approach to removing the fluctuation component was to calculate the temperature at each individual cell, rather than throughout the entire domain, then to remove any oscillatory structures in the calculated temperature field. From a Fourier-space perspective this is synonymous with keeping only the $k = 0$ mode of the temperature wavevector spectrum, which can be calculated more simply as the average temperature across all cells. The improved temperature diagnostic is therefore given as

$$k_B T_j = \frac{1}{N_x N_y N_z} \sum_{l=1}^{N_x N_y N_z} \frac{1}{2} m_j [<v^2>_{jl} - <v>_{jl}^2] \qquad (2)$$

Where l is the scan-line coordinate of each cell and j denotes the species. This calculation is carried out for each velocity vector component to obtain a temperature in each orthogonal direction.

As previous work was performed according to a less than ideal method for calculating the temperature, it is appropriate to perform a comparison study in order to understand the consequences in this change in diagnostics. Figure 2 shows the results of this study. The parameters used in this comparison are those as used in *Hughes et al.* [2014], namely $\beta_e = 0.05$, $\varepsilon_o = 0.1$ in a three dimensional domain of size L = 51.2 c/ω_{pe}. Panel (a) of figure 2 shows that there is little difference in diagnostic method for the electrons. The new diagnostic differs from the old at the beginning of the simulation, where the new diagnostic reveals the electron's attempt to become self consistent with the initial spectrum of fluctuations. Shortly after time t=0, both diagnostics agree well. A much more obvious difference is revealed in panel (b) for the ion population. The temperature profiles are more gradual and smooth under the new diagnostic. The most important feature of figure 2 is that, in the asymptotic limit, both diagnostics agree well, that is, the solutions converge at late simulation times. The new diagnostic is far better suited to studying heating rates as the ion temperature profiles appear to behave more appropriately. However, results from *Hughes et al.* 2014 remain valid, as heating rates weren't investigated, rather the important feature there was the total (late time) heating, which converges under the previously used temperature diagnostic.
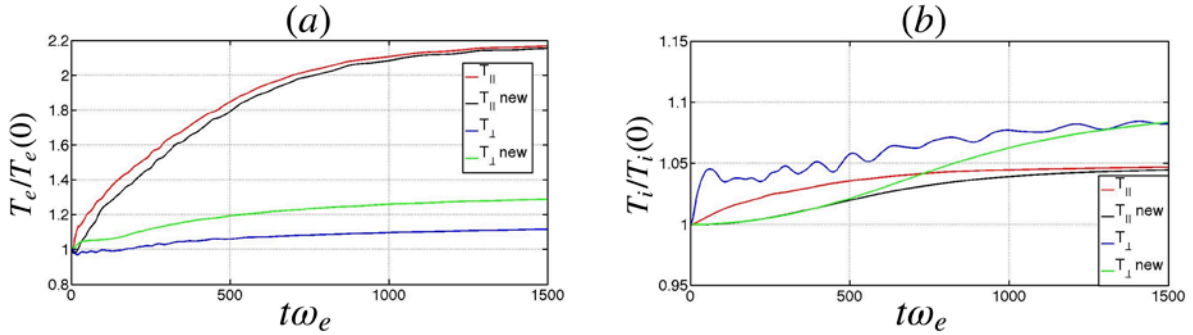

Figure 2: Comparison of the previously used temperature diagnostic with the improved (new) temperature diagnostic. (a) Electron temperatures (b) ion temperatures normalized by initial temperature. Parallel and perpendicular temperatures are shown.

4. Results

Following the simulation set up described in section 3.1, the results of this study are now presented. Figure 3 shows properties of the fluctuating fields as a function of time at each initial value of ε_o. Panel (a) illustrates that in each case the fields undergo and exponential-like decay of energy as the plasma constituents resonate with the fluctuations. The fraction of initial fluctuation energy transferred to the particles increases monotonically with increasing initial amplitude. The fluctuation half-life can be fitted to the power law

$$t_{1/2} = 528\varepsilon_0^{-0.34} \qquad (3)$$

with $R^2 = 0.95$. Panel (b) shows the spectral anisotropy factor over the duration of each run. The spectral anisotropy factor is defined as [*Gary et al.* 2012]

$$\tan^2(\theta_B) = \frac{\sum_k k_\perp^2 |\delta \boldsymbol{B}(k_\perp, k_\parallel)|^2}{\sum_k k_\parallel^2 |\delta \boldsymbol{B}(k_\perp, k_\parallel)|^2} \qquad (4)$$

and describes the preferential angle of propagation relative to the background magnetic field. Values greater than 1 correspond to a preferential angle greater than 45° and signify a highly oblique spectrum, that is a spectrum satisfying $k_\perp \gg k_\parallel$. The results of panel (b) are calculated over the region of wavevector space which excludes the initial fluctuations so as to observe the behavior of the fluctuations generated through the forward cascade process. In all runs the spectrum evolves into a perpendicularly anisotropic state. Early simulation times show a rapid increase of this factor as fluctuation energy flows from the initial spectrum into previously empty regions of wavevector space and establishes the forward cascade. After $t\omega_{pe} \sim 650$ the behavior becomes approximately linear, with the lowest values of ε_o maintaining their degree of anisotropy. The three highest values of ε_o continue to grow

more anisotropic with time, with a higher rate of growth at larger initial fluctuation amplitude. This behavior is interpreted as follows: at early times fluctuation energy cascades to shorter wavelengths, primarily in the perpendicular direction, at a high rate. After the initial fluctuations have transferred energy to sufficiently short wavelengths, dissipation begins to play a prominent role and acts to prevent the spectrum from becoming more anisotropic by removing energy from the quasi-perpendicular, short wavelength region of the spectrum. However, as ε_o increases more energy is available to continue to drive the quasi-perpendicular cascade and the transfer rate remains larger than the dissipation rate for a longer period of time, allowing the spectrum to grow more anisotropic.
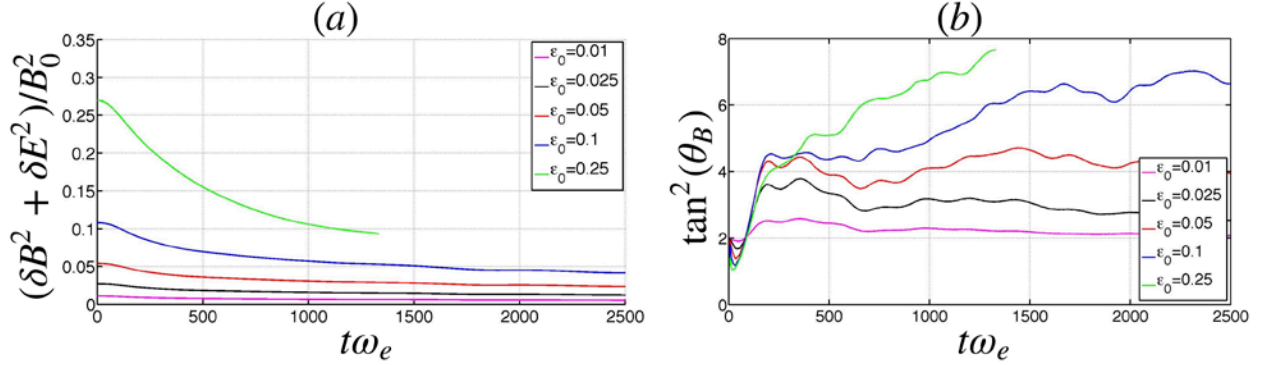

Figure 3: Temporal evolution of field quantities at $\beta = 0.25$ and various values of ε_o as labeled. (a) Total magnetic plus electric field fluctuation energy (b) Wavevector anisotropy factor calculated over the cascaded region of wavevector space.

The parallel and perpendicular temperature profiles for each species are shown in figure 4. All four panels give the expected result that the heating rate increases monotonically with increasing ε_o. The electrons are heated significantly more than the ions and experience greater heating rates at early simulation times, which gradually drop and result in a plateau of the temperature profiles by the end of the simulations. The ion temperature profiles, on the other hand, grow more gradually and steadily maintain nearly linear curves from $t\omega_{pe} \sim 500$ through the end of the simulations. While the electrons immediately begin interacting with the fluctuations and provide the primary means by which the forward cascade can proceed, the ions show little interaction until the fluctuation spectrum has had time to become sufficiently anisotropic. Linear theory of whistler modes at quasi-perpendicular propagation
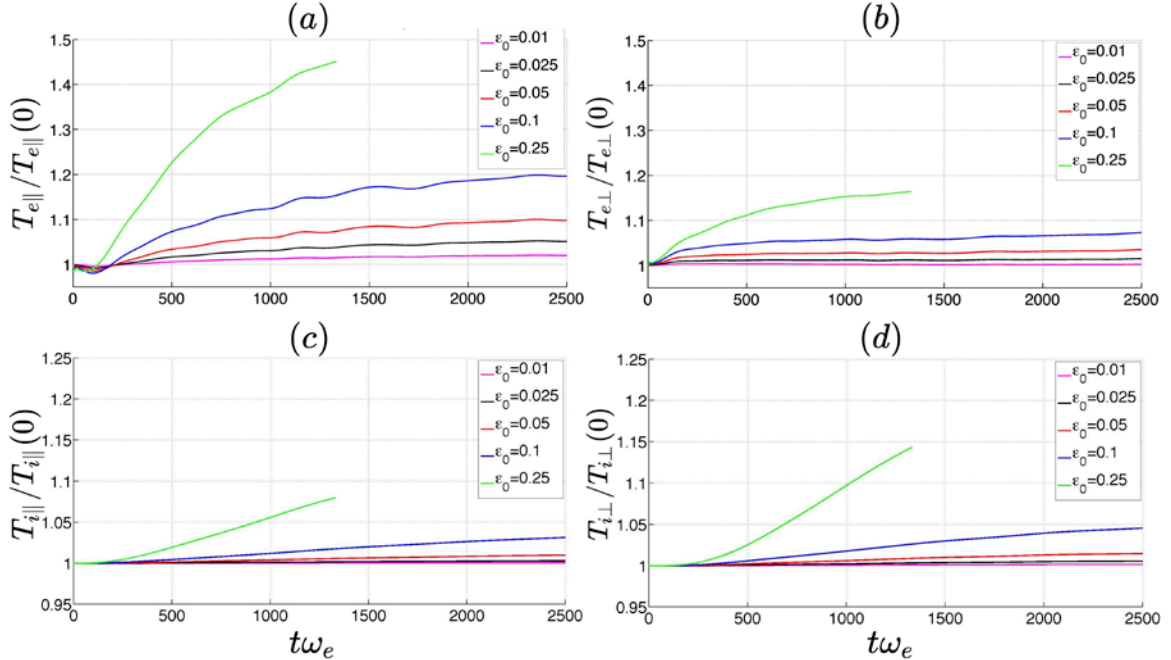

Figure 4: Temporal evolution of the plasma temperatures, normalized by initial temperature, at $\beta = 0.25$ and various values of ε_o as labeled. (a) Electron parallel temperature (b) electron perpendicular temperature (c) ion parallel temperature (d) ion perpendicular temperature.

predicts that $0 < |\delta E_\parallel|^2 \ll |\delta E_\perp|^2$. This condition, along with the anisotropic character of the fluctuation spectrum, implies that such modes will energize the magnetized electrons in directions parallel to the mean field, while the unmagnetized ions will primarily gain energy perpendicular to $\mathbf{B}_0$. This is precisely what is observed, as electrons show preferential parallel temperature gain, while the ions are more greatly heated in perpendicular directions.

The temperature anisotropies are made clearer by figure 5. For both the electron and ion populations, the respective anisotropic character is enhanced as ε_o is increased. As illustrated in figure 3(b) the fluctuation spectrum becomes more anisotropic with ε_o. As the modes responsible for preferential parallel heating of the electrons and perpendicular heating of the ions propagate at quasi-perpendicular directions, the more anisotropic spectrum implies an increase in the temperature anisotropy. In comparing figures 3(b), 4(a) and 5(a) at times between $t\omega_{pe} = 0 - 200$, the early time decrease in electron parallel temperature, and associated increase in the anisotropy factor appears to be associated with the establishment of the anisotropic cascaded spectrum. While the initial isotropic fluctuations heat electrons in the perpendicular direction, interactions in the parallel direction drive fluctuation energy toward shorter perpendicular wavelengths rather than toward higher parallel electron temperatures. Once these quasi-perpendicular fluctuations are established, the primary mode of dissipation is through parallel heating of the electrons, and the temperature anisotropy rapidly drops below 1.
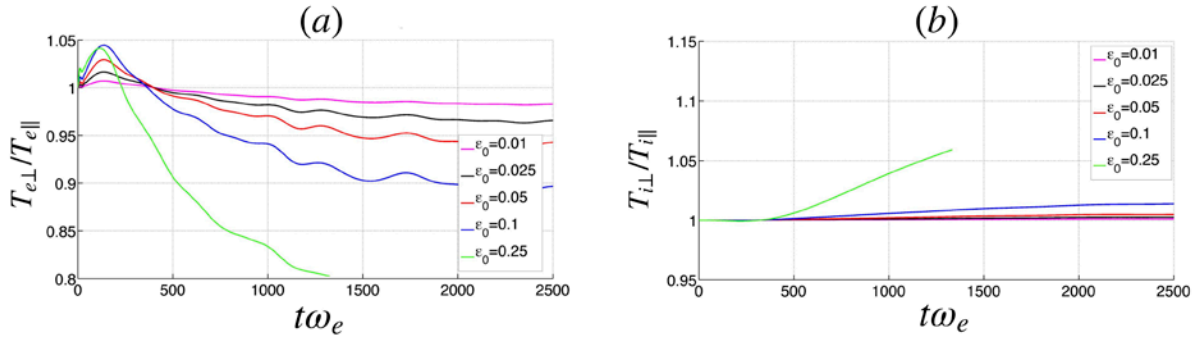

Figure 5: Plasma temperature anisotropy factors with time. (a) Electron $T_\perp/T_\parallel$ (b) ion $T_\perp/T_\parallel$.

The maximum heating rate of each plasma population as a function of initial fluctuation amplitude is illustrated in figure 6. That is, the maximum value of energy gain at any time after $t\omega_{pe} = 200$, when the cascaded spectrum has become established, is determined from the calculated heating rate profiles (not shown) and plotted for each simulation. The dimensionless time rate of energy gain of species j is defined as $Q_j = [dT_j/dt]/[T_j\,(t=0)\omega_{pj}]$. The dotted and dashed lines provide linear profiles which aren't fit to the data, but rather allow for visual comparison with the trends in the data. The electron data points agree well with the dotted line, maintaining a linear

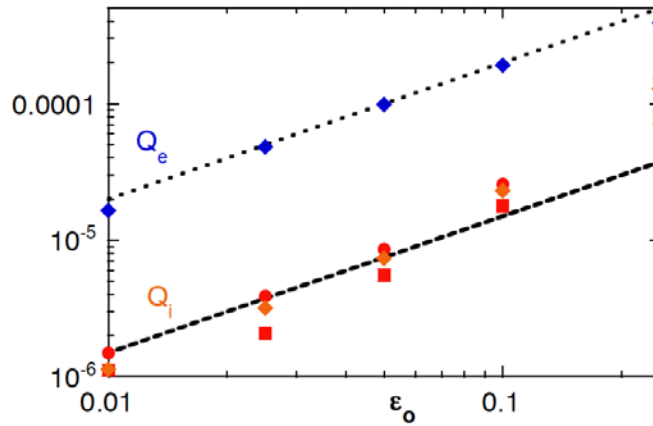Figure 6: The maximum values of the dimensionless time rates of change of the perpendicular ion temperature (red dots), the parallel ion temperature (red squares), the total ion temperature (orange diamonds), and the total electron temperature (blue diamonds) as functions of ε_o at $\beta = 0.25$. The dashed lines represent the equations $Q_i = 0.00015\varepsilon_o$ and $Q_e = 0.002\varepsilon_o$ drawn to guide the eye.

progression over the range of values of ε_o. The ion heating trend is rather different. At very low values of ε_o the trend is nearly linear. However, for $\varepsilon_o = 0.05 - 0.25$ the values increase at a rate greater than linear, scaling as $\varepsilon_o{}^\sigma$ with $\sigma > 1$. As the fluctuation amplitudes become larger the ion heating rates approach those of the electron heating rates. This suggests that at sufficiently large amplitude, ion heating may become the primary mode of dissipation.

An important simulation result here is that both species heating rates scale with fluctuating field energy density at small values of ε_o, consistent with predictions of quasilinear-like second order perturbation theories [*Gary and Feldman*, 1978]. This suggests that quasilinear-like heating rate calculations such as those of *Howes* [2010] are likely to be valid for sufficiently weak magnetic field fluctuations. The second important result is that the late-time ion heating rates increase as $\varepsilon_o{}^\sigma$ with $\sigma > 1$ for sufficiently large ε_o. This transition to an apparently nonlinear ion heating rate is consistent with the results of *Wu et al.* [2013] who used two-dimensional PIC simulations in much larger simulation domains to show that at sufficiently large amplitudes of Alfvénic turbulence ion heating dominates electron heating.

5. Conclusions

Three-dimensional particle-in-cell simulations were carried out to examine the temporal evolution of initially narrowband spectra of whistler fluctuations in homogeneous, collisionless plasmas with initial $\beta_e = 0.25$. The fluctuations undergo a forward cascade to shorter wavelengths, developing a broadband, anisotropic spectrum of turbulence which dissipates energy on both electrons and ions. The simulations confirm earlier results for whistler turbulence that electrons gain energy primarily in the direction parallel/antiparallel to the background magnetic field, but that ions are heated primarily in directions perpendicular to $\mathbf{B}_0$. Several simulations at different initial fluctuation energy densities were carried out; the computations show that both the perpendicular ion heating rate and the total electron heating rate scale approximately as ε_o at $\varepsilon_o \ll 1$. The computations further demonstrate that the perpendicular ion heating rate increases more rapidly than ε_o for sufficiently large values of ε_o.

Whistler fluctuations are of high frequency compared to the proton cyclotron frequency, so that one expects, and our simulations show, that ion heating by whistler turbulence is relatively weak compared to the heating of electrons. However, our results also show that ion turbulent heating appears as preferential energy gain in directions perpendicular to the background magnetic field. Solar corona and solar wind observations show a strong preference for perpendicular ion heating [*Cranmer*, 2014, and references therein], but at present there is no consensus as to the source of this energy gain. One possible source of such heating is resonant Alfvén-cyclotron waves with $kc/\omega_{pi} \sim 1$ [*Gary and Saito*, 2003; *Hollweg and Isenberg*, 2002; *Cranmer*, 2014]; another potential source is "stochastic heating" by nonresonant MHD fluctuations [*Chandran*, 2010], and a third plausible source is resonant magnetosonic-whistler waves [*Markovskii et al*, 2010; *Markovskii and Vasquez*, 2010]. Although relatively weak compared to electron heating, the perpendicular heating of the ions demonstrated in these simulations is consistent with the hypothesis that the obliquely propagating component of magnetosonic-whistler turbulence contributes to the persistent perpendicular heating of protons observed in the solar wind. As *Hughes et al.* [2014] has shown that the efficacy of ion perpendicular heating by whistler fluctuations substantially increases with increasing simulation domain size, it is important that further PIC simulations of magnetosonic-whistler turbulence be carried out at larger computational systems than those used here in order to quantify ion heating rates for comparison against competing candidates for ion energization in the solar wind.

References

Alexandrova, O., J. Saur, C. Lacombe, A. Mangeney, J. Mitchell, S. J. Schwartz, and P. Robert (2009), Universality of solar-wind turbulent spectrum from MHD to electron scales, *Phys. Rev. Lett., 103,* 165003.

Alexandrova, O., C. Lacombe, A. Mangeney, R. Grappin, and M. Maksimovic (2012), Solar wind turbulent spectrum at plasma kinetic scales, *Ap. J., 760,* 121.

Alexandrova, O., C. H. K. Chen, L. Sorriso-Valvo, T. S. Horbury, and S. D. Bale (2013), Solar wind turbulence and the role of ion instabilities, *Space Sci. Rev., 178,* 101.

Chandran, B. D. G. (2010), Alfven-wave turbulence and perpendicular ion temperatures in coronal holes, *Ap. J., 7820,* 548.

Chang, O., S. P. Gary, and J. Wang (2011), Whistler turbulence forward cascade: Three- dimensional particle-in-cell simulations, *Geophys. Res. Lett., 38,* L22102.

Chang, O., S. P. Gary, and J. Wang (2013), Whistler turbulence and variable electron beta: Three-dimensional particle-in-cell simulations, *J. Geophys. Res., 118,* 2824.

Chang, O., S. P. Gary, and J. Wang (2014), Energy dissipation by whistler turbulence: Three-dimensional particle-in-cell simulations, *Phys. Plasmas, 21,* 052305.

Chang, O., S. P. Gary, and J. Wang (2015), Whistler turbulence forward cascade versus inverse cascade: Three-dimensional particle-in-cell simulations, *Ap. J., 800,* 87.

Chen, C. H. K., S. Boldyrev, Q. Xia, and J. C. Perez (2013), Nature of subproton scale turbulence in the solar wind, *Phys. Rev. Lett., 110,* 225002.

Chen, C. H. K., L. Leung, S. Boldyrev, B. A. Maruca, and S. D. Bale (2014), Ion-scale spectral break of solar wind turbulence at high and low beta, *Geophys. Res. Lett., 41,* 8081.

Cranmer, S. (2014), Ensemble simulations of proton heating in the solar wind via turbulence and ion cyclotron resonance, *Ap. J. Supplement Series, 213,* 16.

Frisch, U. (1995), Turbulence: The Legacy of A. N. Kolmogorov, Cambridge University Press, Cambridge.

Gary, S. P. and W. C. Feldman (1978), A second-order theory for k ∥ B0 electromagnetic instabilities, *Phys. Fluids, 21,* 72.

Gary, S. P. (1993), Theory of space plasma microinstabilities, Cambridge University Press, New York.

Gary, S. P., and S. Saito (2003), Particle-in-cell simulations of Alfven-cyclotron wave scattering: Proton velocity distributions, *J. Geophys. Res., 108,* 1194.

Gary, S. P., S. Saito, and H. Li (2008), Cascade of whistler turbulence: Particle-in-cell simulations, *Geophys. Res. Lett., 35,* L02104.

Gary, S. P., and C. W. Smith (2009), Short-wavelength turbulence in the solar wind: Linear theory of whistler and kinetic Alfven fluctuations, *J. Geophys. Res., 114,* A12105.

Gary, S. P., O. Chang, and J. Wang (2012), Forward cascade of whistler turbulence: Three-dimensional particle-in-cell simulations, *Ap. J., 755,* 142.

Hollweg, J., and P. Isenberg (2002), Generation of the fast solar wind: A review with emphasis on the resonant cyclotron interaction, *J. Geophys. Res., 107(A7),* 1147.

Howes, G. G. (2010), A prescription for the turbulent heating of astrophysical plasmas, *Mon. Not. R. Astron. Soc, 409,* L104.

Howes, G. G., J. M. TenBarge, W. Dorland, E. Quataert, A. A. Schekochihin, R. Numata, and T. Tatsuno (2011), Gyrokinetic simulations of solar wind turbulence from ion to electron scales, *Phys. Rev. Lett., 107,* 035004.

Hughes, R. S., S. P. Gary, and J. Wang (2014), Electron and ion heating by whistler turbulence: Three-dimensional particle-in-cell simulations, *Geophys. Res. Lett., 41,* 8681.

Kiyani, K. H., S. C. Chapman, F. Sahraoui, B. Hnat, O. Fauvarque, and Yu. V. Khotyaintsev (2013), Enhanced magnetic compressibility and isotropic scale- invariance at sub-ion Larmor scales in solar wind turbulence, *Ap. J., 763,* 10.

Klein, K. G., G. G. Howes, J. M. TenBarge, S. D. Bale, C. H. K. Chen, and C. S. Salem (2012), Using synthetic spacecraft data to interpret compressible fluctuations in solar wind turbulence, *Ap. J., 755,* 159.

Markovskii, S. A., and B. J. Vasquez (2010), The effect of spectral anisotropy of fast magnetosonic turbulence on the plasma heating at the proton kinetic scales, *Phys. Plasmas, 17,* 112902.

Markovskii, S. A., B. J. Vasquez, and B. D. G. Chandran (2010), Perpendicular proton heating due to energy cascade of fast magnetosonic waves in the solar corona, *Ap. J., 709,* 1003.

Narita, Y., S. P. Gary, S. Saito, K.-H. Glassmeier, and U. Motschmann (2011), Dispersion relation analysis of solar wind turbulence, *Geophys. Res. Lett., 38,* L05101.

Perschke, C., Y. Narita, S. P. Gary, U. Motschmann, and K.-H. Glassmeier (2013), Dispersion relation analysis of turbulent magnetic field fluctuations in fast solar wind, *Ann. Geophys., 31,* 1949.

Perschke, C., Y. Narita, U. Motschmann, and K.-H. Glassmeier (2014), Multi-spacecraft observations of linear modes and sideband waves in ion-scale solar wind turbulence, *Ap. J. Lett., 793,* L25.

Podesta, J. J. (2013), Evidence of kinetic Alfven waves in the solar wind at 1 AU, *Solar Phys., 286,* 529.

Roberts, O. W., X. Li, and B. Li (2013), Kinetic plasma turbulence in the fast solar wind measured by Cluster, *Ap. J., 769,* 58.

Sahraoui, F., M L. Goldstein, P. Robert, and Yu. V. Khotyaintsev (2009), Evidence of a cascade and dissipation of solar-wind turbulence at the electron gyroscale, *Phys. Rev. Lett., 102,* 231102.

Sahraoui, F., M L. Goldstein, G. Belmont, P. Canu, and L. Rezeau (2010), Three dimensional anisotropic *k* spectra of turbulence at subproton scales in the solar wind, *Phys. Rev. Lett., 105,* 131101.

Sahraoui, F., S. Y. Huang, G. Belmont, M. L. Goldstein, A. Retino, P. Robert, and J. DePatoul (2013), Scaling of the electron dissipation range of solar wind turbulence, *Ap. J., 777,* 15.

Saito, S., S. P. Gary, H. Li, and Y. Narita (2008), Whistler turbulence: Particle-in-cell simulations, *Phys. Plasmas, 15,* 102305.

Saito, S., S. P. Gary, and Y. Narita (2010), Wavenumber spectrum of whistler turbulence: Particle-in-cell simulation, *Phys. Plasmas, 17,* 122316.

Saito, S., and S. P. Gary (2012), Beta dependence of electron heating in decaying whistler turbulence: Particle-in-cell simulations, *Phys. Plasmas, 19,* 012312.

Saito, S., and Y. Nariyuki (2014), Perpendicular ion acceleration in whistler turbulence, *Phys. Plasmas, 21,* 042303.

Salem, C. S., G. G. Howes, D. Sundkvist, S. D. Bale, C. C. Chaston, C. H. K. Chen, and F. S. Mozer (2012), Identification of kinetic Alfvén wave turbulence in the solar wind, *Ap. J., 745,* L9.

Stawicki, O., S. P. Gary, and H. Li (2001), Solar wind magnetic fluctuation spectra, *J. Geophys. Res., 106,* 8273.

Taylor, G. I. (1938), The spectrum of turbulence, *Proc. R. Soc. Lond. A*, 164, 476.

Wang, J., P. Liewer, and V. Decyk (1995), 3D electromagnetic plasma particle simulations on a MIMD parallel computer, *Comput. Phys. Commun., 69,* 306.

Wu, P., M. Wan, W. Matthaeus, M. Shay, and M. Swisdak (2013), von Karman energy decay and heating of protons and electrons in a kinetic turbulent plasma. *Phys. Rev. Lett., 111(12),* 121105.

The statistics of relativistic electron pitch angle distribution in the Earth's radiation belt based on the Van Allen Probes measurements

Hong Zhao

Laboratory for Atmospheric and Space Physics and Department of Aerospace Engineering Sciences, University of Colorado at Boulder, Boulder, CO 80302

Reiner Friedel

Los Alamos National Laboratory, Los Alamos, NM 87545

Abstract

The relativistic electron pitch angle distribution (PAD) is an important characteristic of radiation belt electrons, which can give information on source or loss processes in a specific region. Using data from MagEIS and REPT instruments onboard the Van Allen Probes and LANL-GEO satellites, a statistical survey of relativistic electron pitch angle distribution (PAD) is performed. By fitting relativistic electron PADs to Legendre polynomials, an empirical model of PADs as a function of L (from 1.4 to 6), MLT, electron energy (~100 keV – 5 MeV), and geomagnetic activity is developed and many intriguing results are found. In the outer radiation belt, an unexpected dawn/dusk asymmetry of ultra-relativistic electrons is found during quiet times, with the asymmetry becoming stronger at higher energies and at higher L shells. This may indicate the existence of physical processes acting on the relativistic electrons on the order of drift period. In the inner belt and slot region, 100s of keV pitch angle distributions with minima at 90° are shown to be persistent in the inner belt and appears in the slot region during storm times. The model also shows clear energy dependence and L shell dependence of 90°-minimum pitch angle distribution. On the other hand, the head-and-shoulder pitch angle distributions are found during quiet times in the slot region, and the energy, L shell and geomagnetic activity dependence of those PADs are consistent with the wave-particle interaction caused by hiss waves.

Keywords: radiation belt electrons, pitch angle distribution, wave-particle interaction

1. Introduction

The relativistic electron pitch angle distribution (PAD) is an important characteristic of radiation belt electrons, which can give valued information on source or loss processes in a specific region. Many previous studies have focused on the characteristics and evolution of electron PADs in the outer radiation belt [e.g., West et al., 1973; Gannon et al., 2007; Chen et al., 2014]. Generally, the electron PADs in the outer radiation belt can be categorized into three types: the normal distribution, butterfly distribution, and flat top distribution. The normal distribution is the most general type of PAD in the outer belt, for which the electron flux peaks at 90° pitch angle (PA) and smoothly decreases at smaller PAs. It is thought to form as a result of the loss to the atmosphere combining with the pitch angle diffusion. Inward radial diffusion can also cause the flux peak around 90°. Due to the conservation of the first and second adiabatic invariant, when an electron moves inward, the perpendicular momentum increases more than the parallel component, which would increase the PA of electron and thus create a more 90° peaked PAD [e.g., Schulz and Lanzerotti, 1974]. The butterfly distribution has a minimum around 90°, which looks like a butterfly in the polar plot (in which PA is the polar angle and flux is the radius). The butterfly distribution is thought to be caused by the drift-shell-splitting effect combining with magnetopause shadowing or strong negative radial flux gradient [e.g., Sibeck et al., 1987; Selesnick and Blake, 2002]. Horne et al. [2005] have also suggested that chorus wave heating could cause butterfly distribution by preferentially heating off-equator electrons. For the flat top

distribution the electron flux is approximately equal at a wide PA range centered around 90°. It can be a transition between the normal distribution and butterfly distribution or can be due to strong wave-particle interactions [Horne et al., 2003]. For tens to hundreds of keV electrons, "cigar" distribution with flux peaking along the direction of local magnetic field has also been found in the outer radiation belt, and it is thought to be related to the tail-like stretching of the nightside magnetic field prior to the substorms and thus could be used as an indicator of likely substorm onset [Baker et al., 1978].

There are also some studies have focused on those in the slot region and inner belt [e.g., Lyons and Williams, 1975a, 1975b; Zhao et al., 2014a, 2014b]. Lyons and Williams [1975a] found "cap" PAD (also called "head-and-shoulder" PAD) in the slot region after electron injections and during geomagnetic quiet times, which looks like a bump around 90° on top of a normal distribution. As for the formation of cap distributions, Lyons and Williams [1975a] shows the comparison between the observation and modeling of wave-particle interaction, and the agreement between the two suggests that the cap distribution forms as a result of pitch angle scattering caused by the plasmaspheric whistler mode waves in the slot region. However, Sibeck et al. [1987] has also found the cap distribution in the outer belt and suggested that this type of PAD in the outer radiation belt can be caused by a combination of the drift-shell-splitting effect and a substorm injection or a sudden magnetospheric compression. Recently, Zhao et al. [2014a] reported a new type of PADs of 100s of keV electrons in the inner belt and slot region using the observation from Van Allen Probes. This PAD type, called "90°-minimum PAD" here, shows as a Gaussian distribution with a small bite out around 90°. It is generally present in the inner belt and occurs in the slot region during storm times. While the wave-particle interaction caused by fast magnetosonic waves is suggested as one possible mechanism, the actual physical processes responsible for the formation of this type of PADs are still under debate.

The electron pitch angle distribution reflects the effects of different physical processes and the competition between them in a specific region. Understanding the evolution of pitch angle distributions can contribute to the identifying and understanding of those processes and thus the understanding of the inner magnetospheric dynamics. In this report, using data from REPT and MagEIS instruments on the Van Allen Probes and LANL GEO satellites, we construct an empirical model of relativistic electron PADs by fitting PADs into Legendre polynomials. Focusing on the MeV electrons in the outer radiation belt and 10s to 100s of keV electrons in the low L region respectively, the averaged PADs as a function of L, MLT, electron energy, and geomagnetic activity are shown and some intriguing results are found.

2. Data

In this study, pitch-angle-resolved electron flux data from REPT [Baker et al., 2013] and MagEIS [Blake et al, 2013] instruments onboard Van Allen Probes are used. The Van Allen Probes, launched on 30 Aug 2012, operate in an elliptical orbit with an inclination of 10° and altitude of ~600 km × 5.8 R_E [Kessel et al., 2013]. MagEIS provides high-resolution energetic electron flux measurements with energy range of ~35 – 4000 keV. It contains four independent magnetic electron spectrometers on each spacecraft, one low energy spectrometer (LOW), two medium energy spectrometers (M75 and M35) and a high energy spectrometer (HIGH). The low unit, high unit, and one of the medium units (M75) are mounted with the field of view centered at 75° to the spin axis, while the field of view of another medium unit (M35) is centered at 35° to provide larger PA coverage. REPT provides high-quality measurement of relativistic electrons with energy from ~ 2 MeV to ~20 MeV. However, since the counts for ultra-relativistic electrons are too low to show clear PADs, only data for electrons with energy from 1.8 MeV to 3.6 MeV are used in this study. The MagEIS and REPT data are averaged into 1-min bins and 10° PA bins. For REPT data, to eliminate the influence of background contamination, only PADs with total counts greater than 100 are included. Only those data when Van Allen Probes are near the magnetic equator with magnetic latitude < 10° are used in our study, and the electron PADs are propagated to the magnetic equator using T89D magnetic field model [Tsyganenko, 1989] unless otherwise noted. With the spin axis approximately pointing to the Sun, the spacecraft is spinning with a period of ~12s, which provides good pitch angle coverage during most times and thus provides an ideal data set for pitch angle distribution studies.

Pitch-angle-resolved data from Los Alamos National Laboratory Geosynchronous (LANL-GEO) satellites [Reeves et al., 1997] are also used in this study. The LANL-GEO data are also averaged and binned into 15° PA bins. With measured electron energies up to ~1.5 MeV, LANL-GEO data are used to show the electron PADs at different MLTs at geosynchronous orbit.

3. Methodology

To construct a statistical model for relativistic electron PADs, we choose to fit PADs to Legendre polynomials. The electron PADs can be expressed as

$$j(\alpha) = \sum_{n=0}^{\infty} C_n P_n[\cos(\alpha)]$$

where $j(\alpha)$ is the flux of electrons with pitch angle α, $P_n[\cos(\alpha)]$ is the nth-degree Legendre polynomial, and C_n is the corresponding coefficient. The coefficient of each Legendre polynomial can be calculated using the orthogonal property:

$$C_n = \frac{2n+1}{2} \int_0^\pi j(\alpha) P_n[\cos(\alpha)]\sin(\alpha)d\alpha$$

The coefficients derived using this equation are then normalized as

$$c_n = \frac{C_n}{C_0}$$

Here C_0 is the actual directionally averaged flux.

Any PAD can be fully represented by a whole set of Legendre polynomials. However, in a statistical model we can only keep finite number of coefficients and the number of coefficients should be kept as small as possible. Based on the previous study [Chen et al., 2014], C_n decreases quickly with increasing n, and including the Legendre polynomials up to 6th-degree is enough to reproduce most observed PADs in the outer radiation belt. Thus we fit measured PADs in the outer radiation belt to a summation of 0th to 6th degree Legendre polynomials. However, the situation in the inner belt and slot region is very different. The electron PADs in the inner belt and slot region usually have some detailed features, e.g., 90°-minimum PAD and cap PAD, which cannot be well represented by Legendre polynomials up to 6th degree. Thus for PADs in the low L region (L<3.5) we use Legendre polynomials up to 10th degree. In addition, the electron PADs in the radiation belt are expected to be symmetric with respect to 90° pitch angle. In this study, to give a full coverage on all pitch angles, we average PADs measured by Van Allen Probes in bins of 10° PA and force them to be symmetric, and thus the coefficients even-th degree Legendre polynomials are zero.

The accuracy of our model strongly depends on the accuracy of the fitting results, so we use the PADs that can be well represented by the Legendre polynomials to construct the statistical model. Only good fits with root-mean-square-deviation (RMSD)

$$RMSD = \sqrt{\frac{\sum_n (log(\hat{j}) - log(j))^2}{n}} < 0.05$$

are included in the statistics, where j is the measured flux and $\hat{j}$ is the fitting results. According to our results, most fits are valid. For example, for REPT E=1.8 MeV electrons, only 10% fits are rejected due to poor fitting. This also validates our fitting method. On the other hand, it is essential to make sure the fitting results represent the real PADs, so only PADs with full PA coverage have been included. PADs with no data points within high PA range [80°, 100°] or low PA range [0°, 20°]/[160°, 180°] are excluded from the statistics.

Based on this fitting method, a statistical relativistic electron equatorial PAD model is constructed as a function of L, MLT, geomagnetic activity and electron energy using data from MagEIS and REPT from Sep 2012 to June 2015. The model includes 26 L bins from L=1 to L=6 with ΔL = 0.2 and 12 MLT bins with ΔMLT = 2. Note that for ~MeV and more energetic electrons our model only includes L shells down to L=3 since in the slot region and inner belt the fluxes of these electrons are usually too low to show clear PAD pattern. The geomagnetic activity, represented by the geomagnetic indices Dst, is divided into three levels. The medians and standard deviations of coefficients are derived and recorded in each L and MLT bin for electrons with a specific energy under a specific geomagnetic condition. The averaged PADs shown in the following section are generated using medians of coefficients at each L shell, MLT, geomagnetic activity level for electrons with a specific energy. The main results are as follows.

4. Results

Using the method described in section 3, we construct a statistical model for electron PADs as a function of L, MLT, geomagnetic activity, and electron energy using data from Van Allen Probes. In this section, we will show the medians of these coefficients and averaged PADs as well as their dependence on L, MLT, geomagnetic activity and

electron energy, mainly focusing on the >MeV electron PADs in the high L region and 10s to 100s of keV electron PADs in the low L region.

4.1. The dawn-dusk asymmetry of ultra-relativistic electron PADs in the high L region

Using data from REPT instrument, the relativistic electron PADs are investigated in the outer radiation belt. One unexpected feature that shows up in the high L region during geomagnetic quiet times is the dawn-dusk asymmetry of ultra-relativistic electron PADs. Figure 1 shows the comparison of averaged PADs of 1.8, 2.1, 2.6 and 3.4 MeV electrons at different L shells and MLTs during geomagnetic quiet times with Dst > -20 nT. It is clear that at lower L (L<5), the electron PADs are similar at all MLTs, which is expected from the dipole-like geomagnetic field close to Earth. At higher L (L>5), day-night asymmetry of electron PADs is also very prominent, which can be well explained by the drift-shell-splitting effect. However, at higher L shells, the relativistic electron PADs are asymmetric at dawn and dusk, with more peaked pancake PADs at dusk compared to those at dawn, and this asymmetry is more significant for electrons with higher energies and at higher L shell.
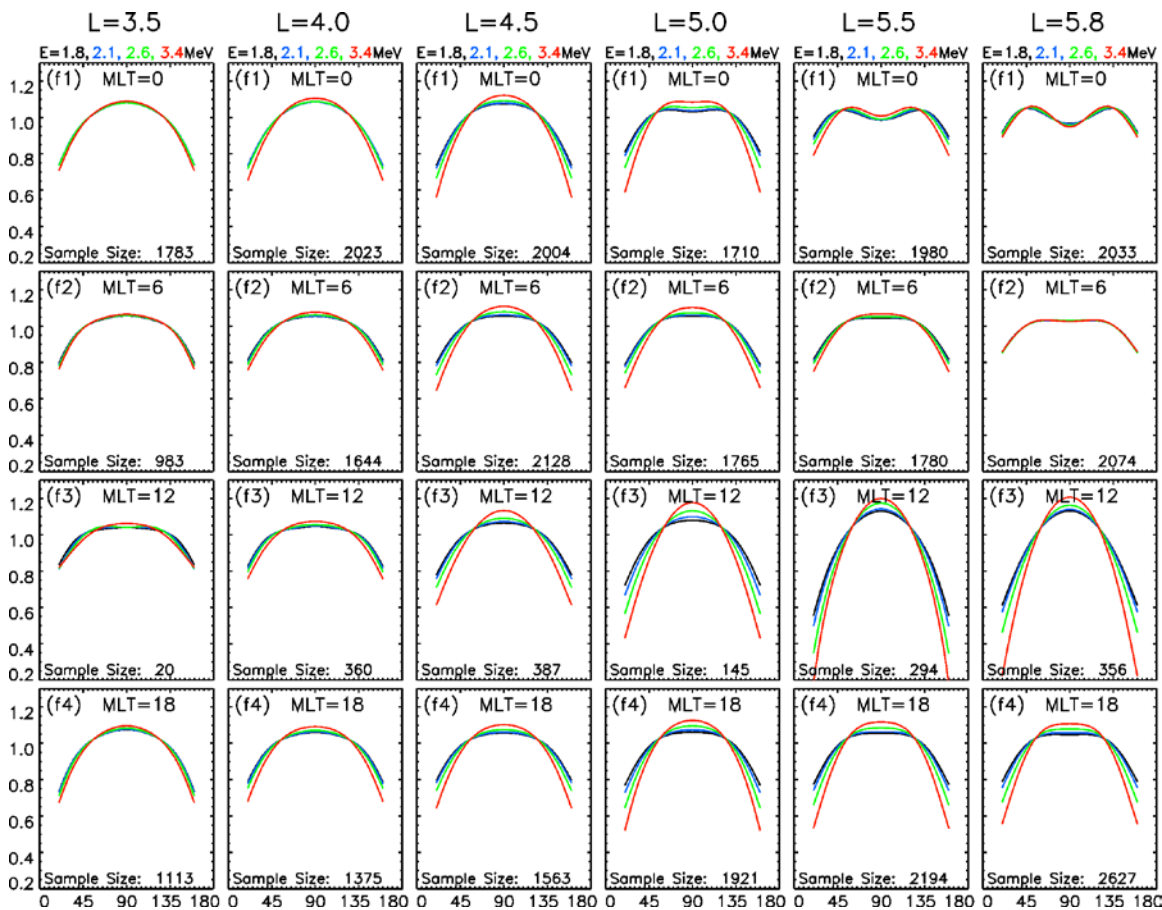

Figure 1. The averaged PADs of 1.8, 2.1, 2.6, and 3.4 MeV electrons as a function of L and MLT, reconstructed from the statistical relativistic electron PAD model.

There are some potential explanations for the observed dawn-dusk asymmetry of electron PADs. One possibility is the dawn-dusk asymmetry of geomagnetic field. The Earth's magnetic field is asymmetric at dawn and dusk due to the existence of partial ring current. However, our model utilizes T89D geomagnetic field model, which is symmetric at dawn and dusk, and this could cause the asymmetry in the PADs. To investigate this possibility, we performed similar analysis using TS04D geomagnetic field model [Tsyganenko and Sitnov, 2005] which

incorporates the partial ring current and is asymmetric at dawn and dusk. Figure 2 shows the averaged PADs of 1.8, 2.1, 2.6 and 3.4 MeV electrons at different MLTs at L=5.8 during geomagnetic quiet times using TS04D model. The dawn-dusk asymmetry is still very clear, which indicates the observed asymmetry is not just due to the asymmetry in the geomagnetic field.
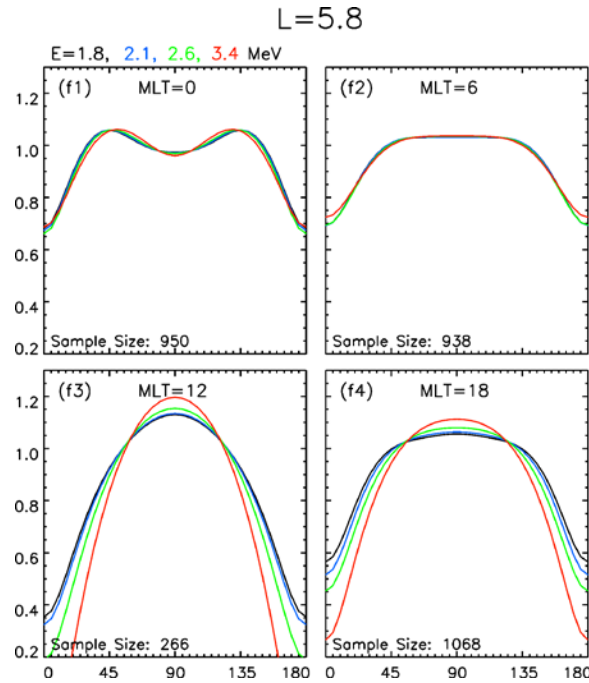

Figure 2. The averaged PADs of 1.8, 2.1, 2.4, and 3.4 MeV electron PADs at MLT=0, 6, 12, and 18 at L=5.8, reconstructed from the empirical electron PAD model based on TS04D model.

Another possible explanation to the observed dawn-dusk PAD asymmetry is the existence of persistent physical processes which can affect electron PADs on the timescale of relativistic electron drift period. One possibility is EMIC waves, which are mostly present at dusk sector and plumes of plasmasphere. EMIC waves can cause losses of low PA >MeV electrons through pitch-angle scattering, and for electrons with higher energies the wave-particle interaction can occur at higher pitch angles [e.g., Li et al., 2007].

However, it is hard to determine if the dawn-dusk asymmetry we observed is physically real or is just caused by sampling since the Van Allen Probes were at different local time sectors at different times. Thus we also use data from LANL-GEO satellites, which were located at different longitudes at geosynchronous orbit and thus can provide simultaneous measurements at different MLTs, to test the observations from Van Allen Probes. Figure 3 shows the averaged PADs of 0.5, 0.75, 1.1, and 1.5 MeV electrons as a function of MLT measured by LANL-GEO satellites during quiet times (Dst > -20 nT). OP77Q geomagnetic field model is used here. Note that the L shells at different MLTs are different because the LANL-GEO satellites were located at a geocentric distance of ~6.6 R_E, which corresponds to different McIlwain L at different MLTs in a non-dipole field. The averaged McIlwain L measured at each MLT is shown in the bottom of each panel. In this Figure, the PADs shown in corresponding MLT sectors (e.g., dawn and dusk, noon and midnight, …) are measured at approximately the same time. It is obvious from this Figure that the averaged PADs observed at both dawn and dusk are butterfly PADs, which is very different from the observations from Van Allen Probes. This may be because of magnetopause shadowing at higher L shells. The observed steeper PADs at dusk than at dawn using Van Allen Probes data are also not visible here. However, this may be due to the fact that the electron energy range measured by LANL-GEO is only up to ~1.5 MeV, while the dawn-dusk asymmetry observed by Van Allen Probes is only significant for ultra-relativistic electrons. As can be seen in Figure 1, at L=5.5 and 5.8, the PADs of 1.8 and 2.1 MeV electrons are almost symmetric at dawn and dusk; the dawn-dusk asymmetry is more significant for 2.6 and 3.4 MeV electrons. Thus to confirm the Van Allen Probes observations, data of electrons with higher energies from LANL-GEO are further required. While another interesting

feature that can be seen from Figure 3 is that the PADs at dusk side are more significant butterfly PADs than those at dawn side. Though not shown here, this asymmetry is not closely related to the solar wind dynamic pressure but more likely associated with the geomagnetic activity, and thus this is more likely due to the asymmetry of the geomagnetic field, since we used McIlwain L in OP77Q geomagnetic field model here, which is also symmetric at dawn and dusk.
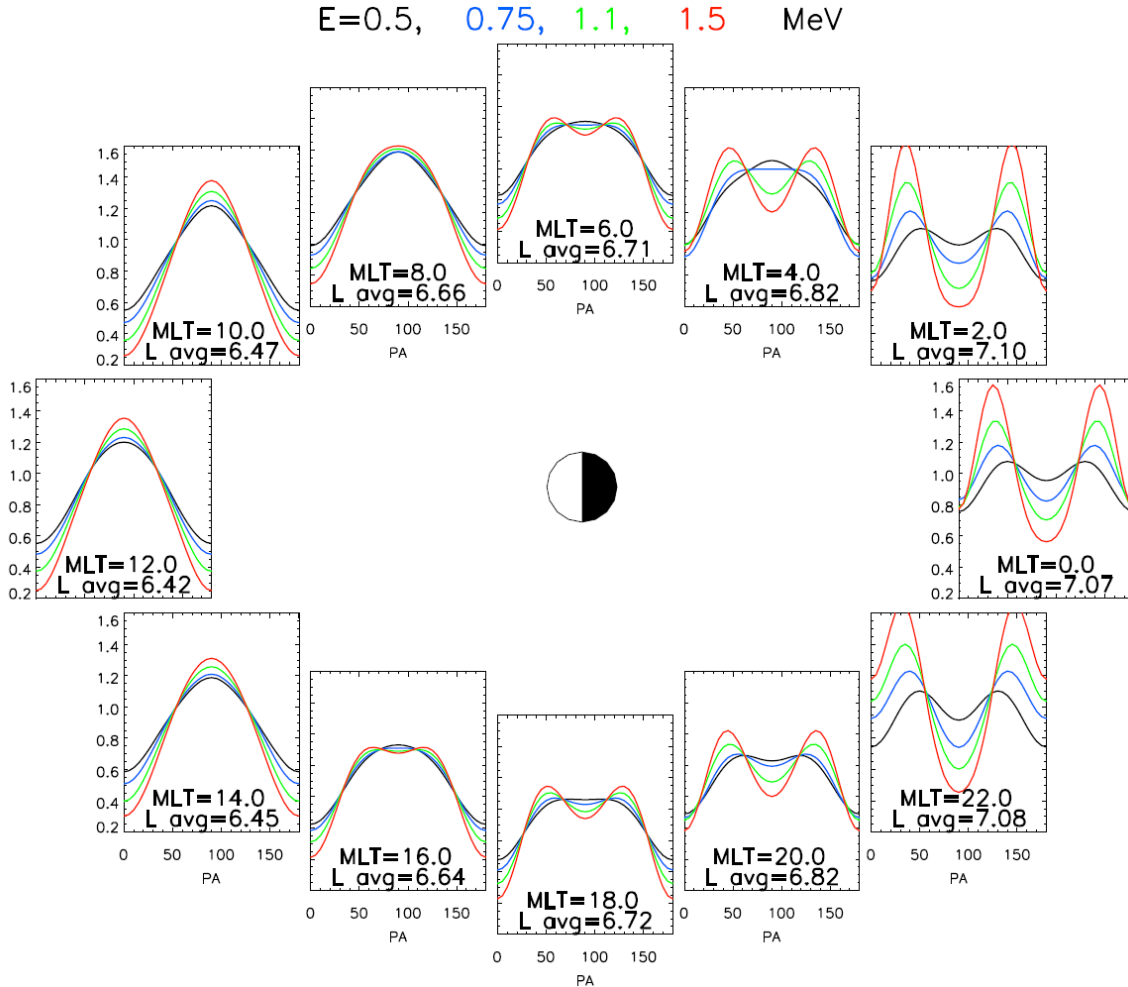

Figure 3. The averaged PADs of 0.5, 0.75, 1.1, and 1.5 MeV electrons as a function of MLT, measured by LANL-GEO satellites.

Another intriguing feature we found when performing the statistical analysis of relativistic electron PADs is that the butterfly PADs of relativistic electrons were observed at dayside occasionally. Figure 4 shows the ~1, 1.6, 2.3 MeV electron PADs observed by MagEIS instruments on the Van Allen Probe-A on 26 Feb 2014, during which the apogee of Van Allen Probe was located around noon and the solar wind condition was quite mild. The butterfly PADs were clearly observed for ~2.3 MeV electrons at higher L region, while for electrons with lower energies, the PADs tend to be more pancake. The evolution of electron PADs around this time shows that the butterfly PADs were formed as the electron fluxes enhanced at low PA. This intriguing observation still cannot be explained by any known theories.
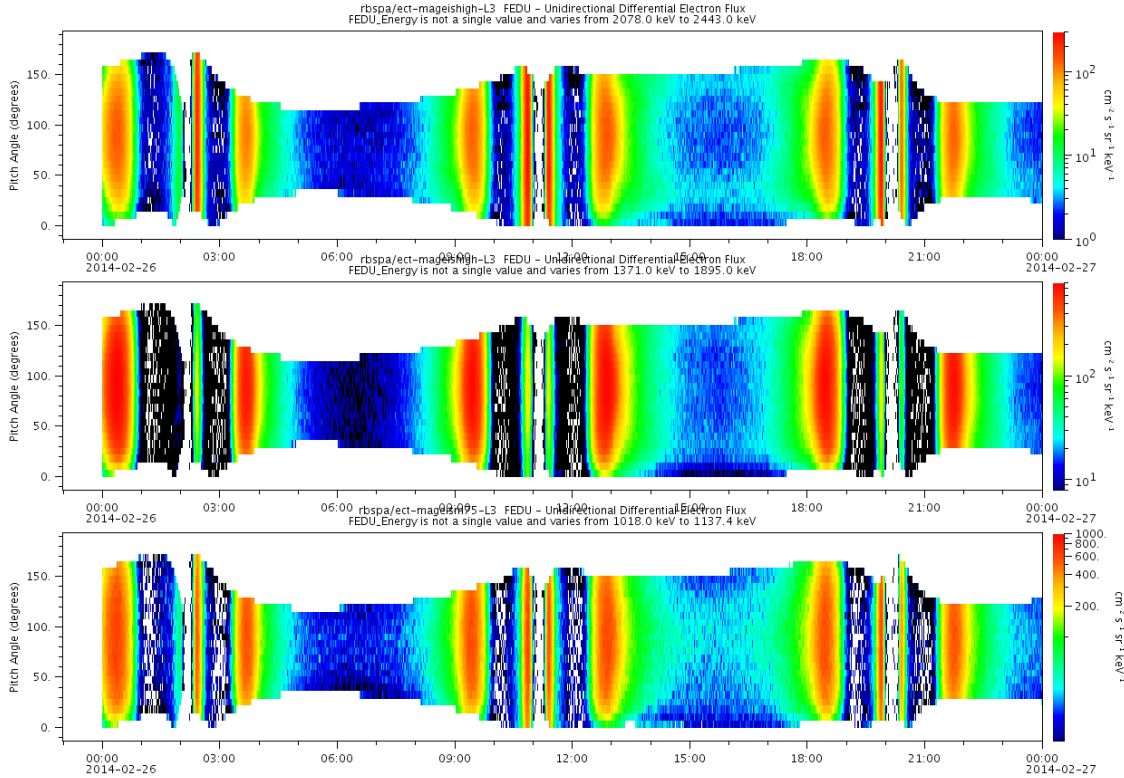
Figure 4. The PADs of ~2.3, 1.6, and 1 MeV electrons on 26 Feb 2014 measured by MagEIS on the Van Allen Probe-A.

4.2. The empirical model of 10s to 100s of keV electron PADs in the inner radiation belt and slot region

MagEIS instruments provide unprecedented clean measurements of 10s to 100s of keV electrons in the low L region. Using data from MagEIS on the Van Allen Probes, an empirical model of 10s to 100s of keV electron PADs in the low L region is constructed. Figure 5 and Figure 6 show some examples of model results in the low L region with intriguing features. Figure 5 shows the averaged PADs of ~105, 235, and 460 keV electrons as a function of MLT in the inner radiation belt measured by MagEIS instruments during quiet geomagnetic activities (Dst > -20 nT). Note that in the inner belt, as expected, the averaged PADs have no dependence on MLT, indicating an azimuthally symmetric geomagnetic field in the low L region. The newly unveiled 90°-minimum PADs are clearly shown in the Figure 5 for different energy electrons. It is clear from Figure 5 that for electrons with higher energies the minimum at 90° PA tends to be more significant. At L=1.4 and 1.6, the minima at 90° PA are very clear; while as the L shell becomes higher, the minima at 90° gradually disappear. Though not shown here, during storm times with Dst < -20 nT, the averaged PADs in the inner belt have more significant minima at 90° PA. This is consistent with the observations from Zhao et al. [2014a, 2014b]. The wave-particle interaction of fast magnetosonic waves is suggested as a possible mechanism responsible for the formation of this PAD type, while the actual causes are still under debate. Though the formation of such 90°-minimum PADs is still not clear, the disappearance of this type of PADs at higher L shells is likely to be caused by the plasmaspheric hiss wave scattering [Zhao et al., 2014b]. Our model results also support this hypothesis, which shows as the cap PADs appear (indicating the presence of hiss wave scattering, as can be seen in the Figure 6) the minima at 90° disappear.

Figure 6 shows the averaged PADs of ~105, 235, and 460 keV electrons as a function of MLT in the slot region measured by MagEIS instruments during quiet geomagnetic activities (Dst > -20 nT). Similarly, no MLT dependence is observed in the slot region either. The cap PADs clearly show up in Figure 6. At L=2.2, the cap PADs are only present for ~460 keV electrons, while for ~105 and 235 keV electrons the PADs are more like pancake PADs. As L shell increases, the cap PADs can be observed for all energy electrons shown here, but the size of "cap" is smaller for higher energy electrons and larger for lower energy electrons. This is consistent with the theoretically

predicted PADs caused by plasmaspheric hiss wave scattering. It is also worth to mention that during geomagnetic active times (Dst < -20 nT) the averaged PADs in the slot region are mostly pancake PADs. This may indicate during active times, other physical processes, e.g., inward radial diffusion and wave heating, play more important roles on relativistic electron dynamics in the slot region than hiss wave scattering.
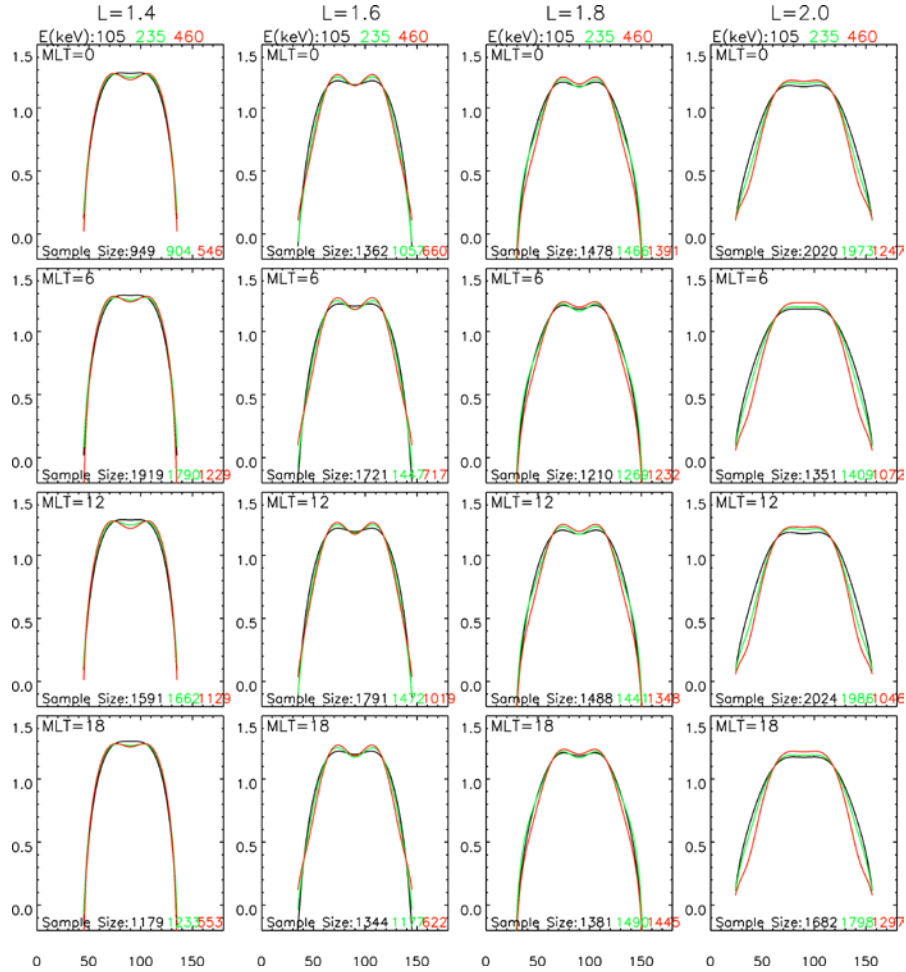

Figure 5. The averaged PADs of ~105, 235, and 460 keV electrons at different MLTs in the inner radiation belt, reconstructed from the statistical relativistic electron PAD model during geomagnetic quiet times (Dst > -20 nT).
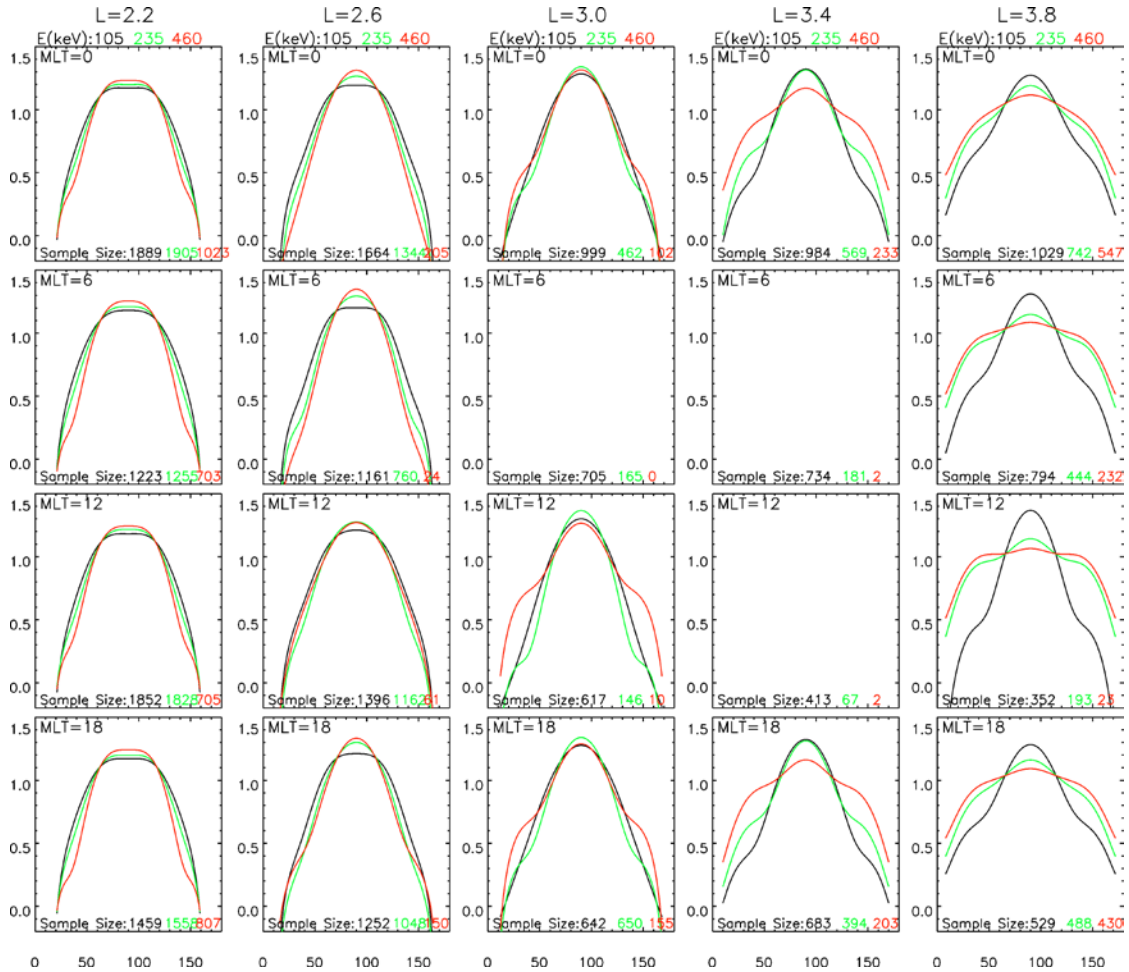
Figure 6. Similar format with Figure 5 but for results in the slot region.

5. Conclusions

A statistical study of relativistic electron pitch angle distribution using data from REPT, MagEIS instruments on the Van Allen Probes and LANL-GEO satellites is performed. An empirical model of radiation belt electron pitch angle distribution as a function of L, MLT, electron energy, and geomagnetic activity is developed and some interesting results are found. The conclusions of this study are as follows:

1) An unexpected dawn-dusk asymmetry of ultra-relativistic electron PADs is observed using data from REPT instruments on the Van Allen Probes, which is shown as more peaked pancake PADs at dusk than at dawn. This asymmetry is only observed for ultra-relativistic electrons and is more significant for electrons with higher energies. It is shown that this asymmetry is not just due to the asymmetry of geomagnetic field, and it is possibly related to the physical processes that can affect relativistic electron PADs on a timescale of drift period. Using data from LANL-GEO satellites which give simultaneous measurements at different MLTs at the geosynchronous orbit, this asymmetry cannot be clearly seen, which could be due to the limited energy range in LANL-GEO data.

2) Using LANL-GEO data, electron PADs at the geosynchronous orbit are investigated and a dawn-dusk asymmetry with more significant butterfly PADs at dusk than dawn is observed. This asymmetry, unlike the one observed by Van Allen Probes, is likely due to the asymmetry in the geomagnetic field.

3) Using data from MagEIS instruments, an empirical model of 10s to 100s of keV electron PADs in the inner radiation belt and slot region is constructed. It is shown that during geomagnetic quiet times, the 90°-minimum PADs in the inner belt are always observed, and the minima at 90° PA are more prominent for electrons with higher energies. In the slot region, the cap PADs are generally observed during quiet times and the dependence of the PAD shape on electrons' energy and L shell is consistent with the theoretical prediction. However, during geomagnetic disturbed times, instead of cap PADs, the pancake PADs are commonly observed, which may indicate the more

important roles of other physical mechanisms, e.g., inward radial diffusion and wave heating, than the hiss wave scattering during geomagnetic storm times.

References

Baker, D. N., P. R. Higbie, E. W. Hones Jr., and R. D. Belian (1978), High-resolution energetic particle measurements at 6.6 Re 3. Low-energy electron anisotropies and short-term substorm predictions, J. Geophys. Res., 83 (A10), 4863-4868, doi:10.1029/JA083iA10p04863.

Baker, D. N., et al. (2013), The Relativistic Electron-Proton Telescope (REPT) Instrument on Board the Radiation Belt Storm Probes (RBSP) Spacecraft: Characterization of Earth's Radiation Belt High-Energy Particle Populations, Space Science Reviews, doi:10.1007/s11214-012-9950-9.

Blake, J. B., et al. (2013), The magnetic electron ion spectrometer (MagEIS) instruments aboard the radiation belt storm probes (RBSP) spacecraft, Space Sci. Rev., doi:10.1007/s11214-013-9991-8.

Chen, Y., R. H. W. Friedel, M. G. Henderson, S. G. Claudepierre, S. K. Morley, and H. Spence (2014), REPAD: An empirical model of pitch angle distributions for energetic electrons in the Earth's outer radiation belt, J. Geophys. Res. Space Physics, 119, 1693–1708, doi:10.1002/2013JA019431.

Gannon, J. L., X. Li, and D. Heynderickx (2007), Pitch angle distribution analysis of radiation belt electrons based on Combined Release and Radiation Effects Satellite Medium Electrons A data, J. Geophys. Res., 112, A05212, doi:10.1029/2005JA011565.

Horne, R. B., N. P. Meredith, R. M. Thorne, D. Heynderickx, R. H. A. Iles, and R. R. Anderson (2003), Evolution of energetic electron pitch angle distributions during storm time electron acceleration to megaelectronvolt energies, J. Geophys. Res., 108(A1), 1016, doi:10.1029/2001JA009165.

Horne, R. B., R. M. Thorne, S. A. Glauert, J. M. Albert, N. P. Meredith, and R. R. Anderson (2005), Timescale for radiation belt electron acceleration by whistler mode chorus waves, J. Geophys. Res., 110, A03225, doi:10.1029/2004JA010811.

Kessel, R. L., N. J. Fox, and M. Weiss (2013), The Radiation Belt Storm Probes (RBSP) and space weather, Space Sci. Rev., 179(1-4), 531–543, doi:10.1007/s11214-012-9953-6.

Li, W., Y. Y. Shprits, and R. M. Thorne (2007), Dynamic evolution of energetic outer zone electrons due to wave-particle interactions during storms, J. Geophys. Res., 112, A10220, doi:10.1029/2007JA012368.

Lyons, L. R., and D. J. Williams (1975a), The quiet time structure of energetic (35-560 keV) radiation belt electrons, J. Geophys. Res., 80 (7), 943-950.

Lyons, L. R., and D. J. Williams (1975b), The storm and poststorm evolution of energetic (35-560 keV) radiation belt electron distributions, J. Geophys. Res., 80 (28), 3985-3994.

Reeves, G., R. Belian, T. Cayton, M. Henderson, R. Christensen, P. McLachlan, and J. Ingraham (1997), Using los alamos geosynchronus energetic particle data in support of other missions, in Satellite-Ground Based Coordination Source Book, edited by M. Lockwood and H. Opgenoorth, pp. 263 – 272, Eur. Space Agency, Noordwijk, Netherlands.

Schulz, M., and L. Lanzerotti (1974), Particle Diffusion in the Radiation Belts, Springer, New York.

Selesnick, R. S., and J. B. Blake (2002), Relativistic electron drift shell splitting, J. Geophys. Res., 107(A9), 1265, doi:10.1029/2001JA009179.

Sibeck, D. G., R. W. McEntire, A. T. Y. Lui, R. E. Lopez, and S. M. Krimigis (1987), Magnetic field drift shell splitting: Cause of unusual dayside particle pitch angle distributions during storms and substorms, J. Geophys. Res., 92, 13,485–13,497, doi:10.1029/JA092iA12p13485.

Tsyganenko, N. A. (1989), A magnetospheric magnetic field model with a warped tail current sheet, Planet. Space Sci, 37, 5.

Tsyganenko, N. A., and M. I. Sitnov (2005), Modeling the dynamics of the inner magnetosphere during strong geomagnetic storms, J. Geophys. Res., 110, A03208, doi:10.1029/2004JA010798.

West, H. I., R. M. Buck, and J. R. Walton (1973), Electron pitch angle distributions through the magnetosphere as observed on Ogo5, J. Geophys. Res., 78, 1064–1081.

Zhao, H., X. Li, J. B. Blake, J. F. Fennell, S. G. Claudepierre, D. N. Baker, A. N. Jaynes, D. M. Malaspina, and S. G. Kanekal (2014a), Peculiar pitch angle distribution of relativistic electrons in the inner radiation belt and slot region, Geophys. Res. Lett., 41, doi:10.1002/2014GL059725.

Zhao, H., X. Li, J. B. Blake, J. F. Fennell, S. G. Claudepierre, D. N. Baker, A. N. Jaynes, and D. M. Malaspina (2014b), Characteristics of pitch angle distributions of hundreds of keV electrons in the slot region and inner radiation belt, J. Geophys. Res. Space Physics, 119, 9543–9557, doi:10.1002/2014JA020386.

Los Alamos Space Weather Summer School
30 Bikini Atoll Rd, ISR-1, MS D466
Los Alamos, NM 87545

http://swx-school.lanl.gov